The Boundary Element Method Simulation of Adhesion of Brush-Structures

vorgelegt von

M. Sc.

Xin He

an der Fakultät V – Verkehrs- und Maschinensysteme

der Technischen Universität Berlin

zur Erlangung des akademischen Grades

Doktor der Ingenieurwissenschaften

- Dr.-Ing. -

genehmigte Dissertation

Promotionsausschuss

Vorsitzende: Prof. Dr.-Ing. habil. Sandra Klinge

Gutachter: Prof. Dr. rer. nat. Valentin L. Popov

Gutachter: Prof. Dr.-Ing. Thomas Geike

Tag der wissenschaftlichen Aussprache: 19. Oktober 2021

Berlin 2021

Acknowledgements

This work was conducted at the Department of System Dynamics and Friction Physics in the Technische Universität Berlin. It was my great pleasure to be engaged in the scientific research on bioinspired adhesion. I would like to express my gratitude to colleagues in the research group, past and present, who helped me during the past four years.

I am especially grateful to my supervisor, Professor Valentin L. Popov, for his constant support and guidance. Many times, his theoretical prediction pointed out clear directions for the numerical simulations. I benefited a lot from his insightful advice during the study. I would like to thank Dr. Qiang Li for his explanation of the Boundary Element Method, and constructive feedback on my numerical algorithm. I would also like to thank Weike Yuan for his willingness to discuss many ideas, and Dr. Roman Pohrt for his advice for improving the quality of programming.

I am also grateful to my friends Shucheng Wang, Yuanheng Mu, who helped me during the COVID-19 lockdown period, especially to Yinan Liu, who supported me graciously with patience.

Finally, I would like to thank my beloved family, who continuously supported me without doubt and has been a tremendous source of inspiration in my life.

Abstract

The structure of biological adhesion systems, which mainly contribute to insects' strong adhesion ability, have attracted great interest of researchers in the last few decades. A lot of theoretical analysis has been carried out to understand the mechanism of bio-adhesion, for example, the concept of contact splitting and the principle of equal load sharing. In this work, we numerically study the adhesive contact of brush-structures on an elastic half-space. The structure is composed of a large number of cylindrical pillars, which are elastically embedded into a common rigid base. We consider different approaches for adhesion enhancement based on the concept of fine subdivision of compact interfaces. This work addresses two investigation directions of adhesion behavior of brush-structures: one based on the structure of brush-models, from compact cylinder to splitting- and to hierarchical structures; and the other one based on the configuration of contact surfaces, from rough contact shapes to optimized contact profiles.

This work is carried out with the help of the Fast Fourier Transform-assisted Boundary Element Method (BEM). The BEM for adhesive contact of rigid bodies in contact with an elastic half-space is further developed for cases considering the pillar stiffness (stiffness of the elastic connection between rigid pillars and the base). With this effective numerical tool, the adhesion behavior of different brush-structures during the pull-off process is numerically studied. The influence of a series of structure parameters including pillar stiffness, pillar number, distribution of pillars, filling factor (density of pillar distribution), roughness and macroscopic contact shape as well as loading parameter on the adhesive contact, is investigated in detail. Analytical predictions of two limiting cases of brush-structures with rigid pillars and very soft pillars are consistent with the numerical results obtained in this work. The transitional development between these two limiting cases is observed, and different approaches for adhesion enhancement such as softer pillars and multi-level hierarchical structures, are systematically analyzed.

Zusammenfassung

Struktur von biologischen Adhäsionssystemen, die vor allem zur starken Adhäsionsfähigkeit von Insekten beitragen, haben in den letzten Jahrzehnten großes Forchungsinteresse geweckt. Viele theoretische Analysen wurden durchgeführt, um den Mechanismus von Bioadhäsion zu verstehen, zum Beispiel das Konzept der Kontaktspaltung und das Prinzip der gleichmäßigen Lastverteilung. In dieser Arbeit untersuchen wir numerisch den adhäsiven Kontakt von Bürstenstrukturen im Kontakt mit einem elastischen Halbraum. Die Struktur besteht aus einer Vielzahl von zylindrischen Stäben, die elastisch in eine gemeinsame starre Basis eingebettet sind. Unterschiedliche Methoden zur Verbesserung der Adhäsion basierend auf der feinen Unterteilung kompakter Grenzflächen werden untersucht. Wir untersuchen den adhäsiven Kontakt von Bürstenstrukturen unter zwei Gesichtspunkten. Zum einen basierend auf der Struktur von Bürstenmodellen (von kompakten Zylindern über Splitting- bis hin zu hierarchischen Strukturen). Zum Anderen von Gesichtspunkt der Konfiguration der Kontaktflächen (von rauen Kontaktformen bis hin zu optimierten Kontaktprofilen).

Simulationen in dieser Arbeit werden mit Hilfe der Fast Fourier Transform-unterstützten Randelemente-Methode (BEM) durchgeführt. Die Methode für den adhäsiven Kontakt von starren Körpern in Kontakt mit einem elastischen Halbraum wird für Fälle weiterentwickelt, die die Fasersteifigkeit (Steifigkeit der elastischen Verbindung zwischen starren Stäben und Basis) berücksichtigen. Mit diesem effektiven numerischen Verfahren wird das Adhäsionsverhalten verschiedener Bürstenstrukturen während des Abziehprozesses numerisch untersucht. Der Einfluss von einer Reihe von Strukturparametern, einschließlich Fasersteifigkeit, Faseranzahl, Faserverteilung, Füllfaktor (Dichte der Faserverteilung), Rauheit und makroskopische Kontaktform sowie Belastungsparameter auf den Adhäsionskontakt wird eingehend untersucht. Analytische Vorhersagen von zwei Grenzfällen von Bürstenstrukturen mit starren Stäben und sehr weichen Stäben stehen im Einklang mit den Ergebnissen von den numerischen Simulationen. Der Übergang zwischen diesen beiden Grenzfällen wird beschrieben und unterschiedliche Ansätze zur Verbesserung der Adhäsion wie weichere Säulen und mehrstufige hierarchische Strukturen, werden systematisch analysiert.

Publications

The following are publications during the doctoral studies:

[1] He, X; Li, Q.; Popov, V. L. Simulation of Adhesive Contact of Soft Microfibrils. Lubricants, 2020, 8, 94. doi.org/10.3390/lubricants8100094

[2] He, X; Li, Q.; Popov, V. L. Strength of adhesive contact between a rough fibrillar structure and an elastic body: Influence of fibrillar stiffness. The Journal of Adhesion, 2021. doi: 10.1080/00218464.2021.1939017

Part of the content in Chapter 3 and Chapter 4 follows the paper [1].

Part of the content in Chapter 5 follows the paper [2].

Contents

List of Figures

Chapter 1 Introduction

1.1 Bio-inspired adhesion

The strong climbing ability of many insects with adhesive organs has inspired wide scientific research interest for understanding the mechanism of bio-adhesion [1][2]. For example, the gecko can generate reversible adhesion to stick on the wall at speeds up to 1 m/s [3], and bear a force over 20 *N* on a pad area of 220 mm^2 [4]. Such adhesion abilities have promoted scientific research on the intrinsic mechanisms of dry adhesion [5]-[9] and various engineering applications in industrial and medical fields [10]-[12], as well as the development of artificial attachment systems [13]-[18].

The microstructure of insects' adhesion systems is regarded as the main contributing factor to the strong adhesion ability [19]. For example, one gecko's toe contains several lamellas, which include numerous setae, and then each seta branches into a large number of spatula pads, as shown in Figure 1-1 [20]. There is van der Waals interaction (adhesion) [1][21], simultaneously working together with capillary forces [22] as well as friction between the bio-attachment structure and the substrate. When the gecko climbs on the wall, this adhesion structure of millions of micro-fibrils complies with the contacting surface, to ensure intimate contact and then to generate a strong sticking force.

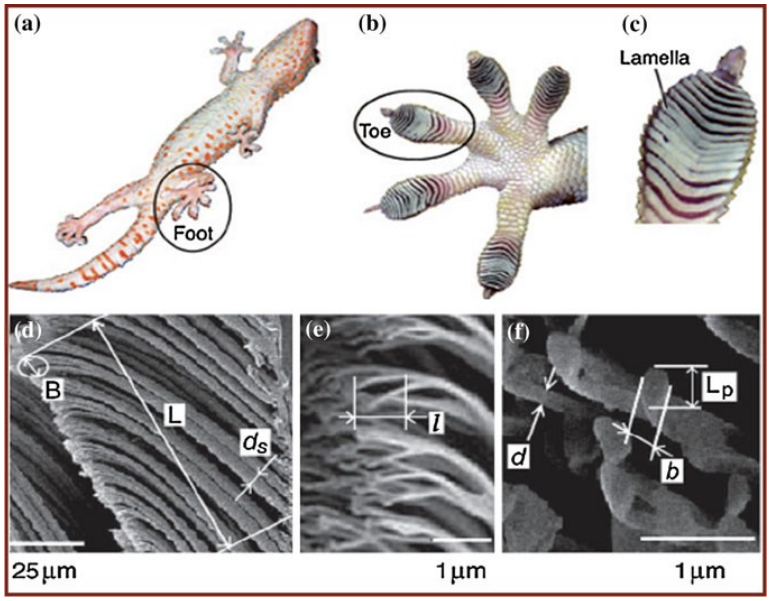

Figure 1-1 Hierarchical adhesion structures of a gecko's foot pad in different scales: (a) Gecko, (b) foot, (c) toe, (d) setal array, (e) spatulae, and (f) spatula pads. Reproduced from Ref. [20] with permission from the National Academy of Sciences. Copyright (2006) National Academy of Sciences, U.S.A.

In the last few decades, a lot of related work has been carried out to mimic those biological adhesion structures, and different experimental models have been developed [23]-[36].

Geim et al. produced a simple array structure of flat-ended fibrils using polyimide [28]. It was found that the strength of adhesion was linearly related to the contact area. Peressadko et al. studied the adhesion behavior of a patterned surface using polyvinylsiloxane (PVS). A stronger adhesive strength was obtained in comparison with that of an unpatterned surface made of the same material [29]. Later, it was shown that a microfabricated carbon nanotubes (CNT) array possessed a reversible and robust adhesion ability [30][31]. Greiner et al. fabricated a hierarchical fibrillar structure using polydimethylsiloxane (PDMS) through photolithography, as shown in Figure 1-2 [32]. Murphy et al. produced a multi-level structure using polymeric material [33]. Corresponding experimental results of the two-level structure exhibited an increased adhesive strength and better toughness of structure, compared with the results of the single-level structure as well as unstructured samples. However, when fibrils are soft and slender, some of them could tend to bunch together. This effect decreases the number of working fibrils as well as the adhesive strength.

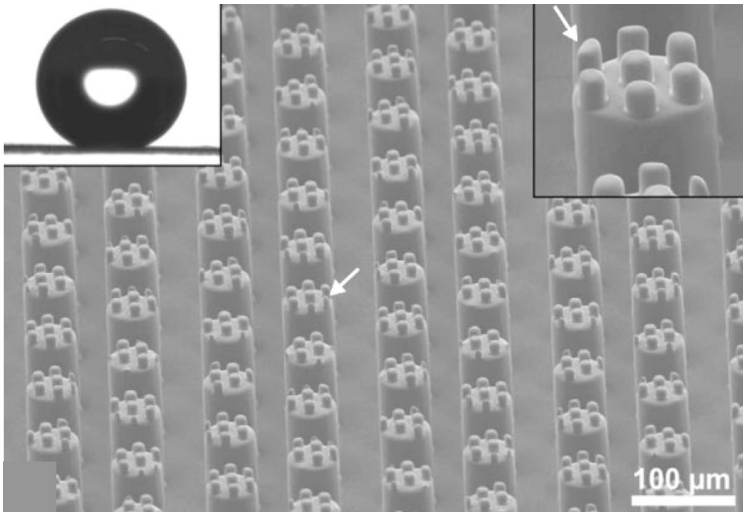

Figure 1-2 A two-level fibrillar structure by using PDMS. Reproduced with permission from [32]. Copyright (2009) Wiley.

On the other hand, various fibril geometries have been studied in the last few years. Del Campo et al. fabricated a series of tip geometries of PDMS fibrils through lithographic and soft-molding method, as shown in Figure 1-3 [9]. It was found that the mushroom-shaped tip benefited from a significant reduction of the stress concentration and obtained stronger adhesion compared with a flat profile [34][35]. Wang et al. further studied mushroom-shaped PDMS pillars and hierarchical structures through conventional photolithography and molding techniques [36]. Heide-Jørgensen et al. investigated the fracture response of

a double cantilever beam (DCB) model with an array of pillars between the upper and lower beams. They altered the geometry of pillars to affect the fracture behavior of DCB model and then to improve the toughness of structure [11]. Morano et al. fabricated adhesive-bonded DCB fracture specimens with an array of sub-surface (hollow) channels, and suggested that the geometry of channels affected the dissipated energy needed for separating the interface [12].

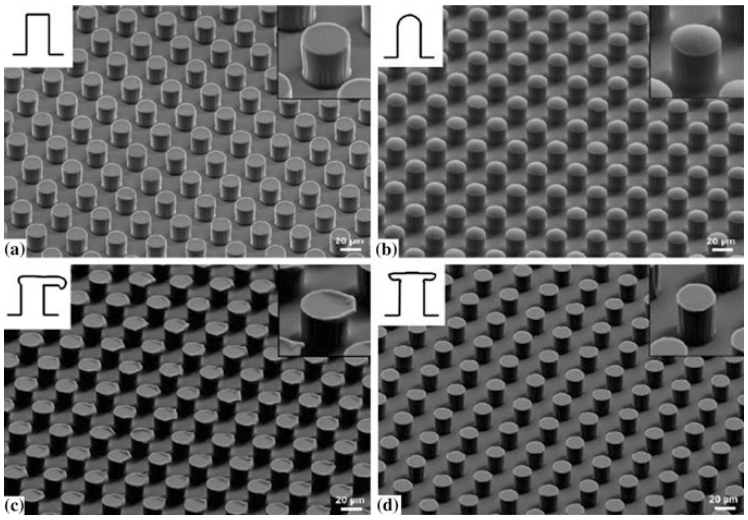

Figure 1-3 Fibrillar structures with different tip geometries: (a) flat-ended; (b) spherical; (c) spatula; (d) mushroom shape. Reprinted with the permission from Ref. [9]. Copyright (2007) American Chemical Society.

1.2 Theoretical models of adhesive contact

For understanding the adhesion mechanism of insects' adhesion systems, a lot of theoretical analysis based on theories of adhesive contact in contact mechanics has been carried out for a few decades. Here we shortly review those classic theories and models of adhesive contact.

1.2.1 Classic theories of adhesive contact

The problem of normal contact between two smooth elastic bodies was solved in 1882 by Hertz [37]. He used an optical microscope to measure the contact between glass spheres and verified his theory. However, some experiments contradict the Hertzian theory. In the 1960s, Roberts using smooth rubber spheres and Kendall using glass spheres, found that the experimental results agreed with the Hertzian theory when the applied load was large. However, at low applied load, the contact area between two bodies was larger than the value predicted by Hertz, and a constant finite contact area remained when the applied load

was removed [38][39]. The reason for that is that the attractive interaction between the contacting solids, which is now usually called adhesion, is not considered in the Hertz theory [40][41].

In 1971, Johnson, Kendall and Roberts solved the adhesive contact between two elastic spheres [42]. Based on the Griffith energy balance criterion, they calculated the elastic energy stored in the deformed bodies and the surface energy for creating new surfaces. The relation between the applied load and the contact area was obtained by equilibrating the two energies. For the pull-off force, they found

$$F = -\frac{3}{2}\pi R\Delta\gamma, \tag{1.1}$$

where $\Delta\gamma$ represents surface energy per unit area, R is the combined radius defined by $1/R = 1/R_1 + 1/R_2$, R_1 and R_2 are the radii of the two contacting spheres. The attractive force in the JKR theory is considered only within the contact area. In 1975, Derjaguin, Muller and Toporov proposed another theory, the DMT theory [43][44], which considered the attractive force outside of the contact area. The corresponding pull-off force is

$$F = -2\pi R\Delta\gamma. \tag{1.2}$$

In 1977, Tabor [45] showed that the JKR and DMT theories were two special cases of the general problem, and defined a dimensionless parameter μ_T linking these two models

$$\mu_T = \left[\frac{R\Delta\gamma^2}{E^{*2}z_0^3}\right]^{\frac{1}{3}}, \tag{1.3}$$

where z_0 is the equilibrium separation between the two contacting surfaces, and E^* is the effective elastic modulus. Following this theory, the JKR model is applicable to compliant large bodies (large Tabor parameter), and the DMT model works well for stiff small solids (small Tabor parameter). A continuous increase of the Tabor parameter and the transition from the DMT to the JKR were numerically observed in [46]. Based on Tabor's idea, Maugis [47] considered the Dugdale [48] cohesive zone approximation to present the surface stress, so that the surface energy is given by

$$\Delta\gamma = \sigma_0 h_0, \tag{1.4}$$

where σ_0 is the adhesive stress between two surfaces and is assumed constant in the range up to a distance h_0. A dimensionless parameter λ is introduced, which is equivalent to the Tabor parameter μ_T

$$\lambda = \sigma_0\left(\frac{9R}{2\pi E^{*2}\Delta\gamma}\right)^{\frac{1}{3}} \approx 1.16\mu_T. \tag{1.5}$$

The JKR model is obtained for large values of λ, and the DMT model for small λ.

1.2.2 Adhesive contact of rough surfaces

In reality, there is no object whose surface is absolutely smooth. It is widely known that surface roughness has a significant influence on the contact of elastic bodies. The Greenwood-Williamson model based on non-interacting spherical asperities with the same curvature radius, was the first model to predict that the real contact area increases approximately linearly with the applied load [49][50]. In the last twenty years, a large number of studies on roughness in contact mechanics have been conducted. For example, Persson considered the multi-scale feature of rough surfaces, and proposed a magnification-based pressure diffusion method to determine the stress probability distribution, under the assumption of initial full contact at the interfaces [51]-[54]. Numerical methods such as the Finite Element Method, the Boundary Element Method, Molecular Dynamics have been applied to investigate the real contact area, contact stiffness, and so on [55]-[57]. Considering adhesion, many models based on the non-adhesive contact theories have been further developed, to investigate the influence of roughness on adhesion. For instance, Ciavarella introduced a Bearing Area Model (BAM) [58]-[61] based on the DMT theory for relatively stiff bodies, to investigate the adhesive contact between elastic rough solids. The results were similar to those obtained by the Persson and Scaraggi's DMT model.

It is clear that roughness can reduce adhesion. Fuller and Tabor have proposed a basic model using the Gaussian distribution to describe the surface asperity height, and found that roughness prevented intimate contact, and thus, even minor roughness could weaken adhesion [62]. However, the roughness at the small level can also enhance adhesion. Briggs and Briscoe experimentally observed that a slightly rough surface exhibited stronger adhesion than a smooth one in the pull-off experiment of smooth rubber against a perspex cylinder [63]. This effect has been confirmed by Fuller and Roberts using soft rubbers in contact with rough glasses [64]. A similar conclusion was found in the analytical study on adhesive contact of spheres with axially symmetrical waviness by Guduru [65].

In this work, we also consider the 'roughness', but the roughness of 'fibrillar structures', which refers to the length (or height) distribution of fibrils. The adhesion ability of such structures could be modified by varying the elasticity of fibrils and the characteristic roughness (length distribution).

1.2.3 Fibrillar surface model

As mentioned above, with the increasing interest in bio-adhesion, various theoretical models have been developed to investigate adhesive contact of fibril structures [17][66][67]. Bhushan considered a multi-level hierarchically structured spring model for simulation of the model contacting with randomly rough surfaces, and the DMT theory was applied to each spring in the bottom level of the hierarchical structure. Hui et al. proposed a spring model containing an array of independent linear springs with spherical tips, and the length of fibrils was ruled by the Gaussian distribution to represent the height of surface asperities [68]-[70]. Schargott proposed a 3D model consisting of hierarchical layers of vertical or tilted beams, based on the structure of tokay gecko's pad, to investigate the adhesive rough contact [67].

In the last twenty years, the concept of contact splitting has raised popular discussion. It argues that strong adhesion can be obtained by dividing a continuous surface into small sub-contact surfaces, since the adhesive stress for separation of two surfaces is severely size-dependent [71]-[73]. Related experimental and numerical studies have shown that a discontinuous contact surface can enhance adhesion in comparison with a compact one.

However, in the recent theoretical and numerical studies on adhesive contact between a rigid flat-ended indenter with different shapes and an elastic half-space, it has been found that the adhesive force is roughly proportional to the square root of filling factor (the ratio of the real contact area to the apparent contact area) [74]. The numerical study on adhesive contact between a rigid flat brush-structure and an elastic half-space, showed a different conclusion compared with the contact splitting [75]: no obvious adhesion enhancement was observed. Another investigation of rigid rough brush-structure, i.e. the length distribution of pillars was described by the exponential probability density [76], showed a similar result of no adhesion enhancement. It is noted that in [75][76] the indenters and pillars are rigid, not deformable, but in the biological contact, the 'pads' are generally compliant.

Furthermore, in the most of splitting models, the fibrils are assumed independent of each other. While in the recent three-dimensional simulations [75][76], the interactions among rigid pillars, which affect stress distribution, are coupled through the elastic contact with the elastic foundation, but the whole structure is rigid. Therefore, in this work, we introduce the elasticity of brush-structure into the numerical study and bridge these two limiting cases described above.

1.3 Numerical methods for adhesive contact

For adhesive contact of an indenter with a simply shaped- or an axial symmetric profile, the analytical solution could be obtained. In contact problems of biological microstructures, the fibrils are commonly modeled by linear springs, and the whole surface structure is represented by independent springs or complicated hierarchical structure of springs with different stiffness [77][78]. Fibrillar structures have also been modeled by rigid micro-cylinders based on Kendall's theory of cylindrical contacts [79]. For complicated structures, numerical methods have to be introduced, such as Molecular Dynamics (MD), the Finite Element Method (FEM), the Boundary Element Method (BEM), etc.

Molecular Dynamics is a well-established approach for simulation of particle interactions as well as some contact problems in the nano-, micro- and mesoscale [80]-[82]. For example, Yang and Persson simulated contact between a flat elastic block and a rigid rough surface using MD, and the results agreed with the analytical theory of Persson [83]. Gilabert et al. carried out MD simulation of adhesive contact between a rough sphere and a smooth rigid plane [84]. However, the high computational cost associated with the spatial resolution is the limitation of MD [85].

The Finite Element Method is a very popular numerical tool for solving various problems in engineering [86][87]. Optional element variants, high tolerance for boundary conditions, as well as capability of handling complex geometries and loading situations, made the FEM the most popular numerical approach for dynamic simulation and stress analysis. For example, Takahashi numerically studied a multi-spring model based on the FEM [88], where springs were governed by the JKR theory and each of them acted individually. Although the FEM is versatile for many applications and its result is almost robust, the computational costs of using the FEM for contact problems are usually huge due to the discretization of the whole testing body.

In comparison with the FEM, the Green's function-based Boundary Element Method is more applicable for solving contact problems. Under the assumption of the elastic half-space, the already known fundamental formulations of displacement and traction are directly applied for numerical simulation. Instead of three-dimensional discretization in the FEM, only two-dimensional discretization of contacting surfaces is necessary for the BEM, which allows to avoid numerical dispersion and dissipation effects [89]-[91]. Since the 1990s, this method has been intensively developed for various contact problems of rough bodies [92]-[94].

From the fundamental formulations of contact problems, it is clear that the displacement of surfaces is calculated by a convolution of the traction and corresponding influence

functions over the whole surface, e.g. the Boussinesq-Cerruti solution [95][96]. The numerical calculation of this convolution has high complexity of $O(N^4)$ if the surface is discretized into $N \times N$ elements. In order to accelerate the calculation, a few fast computational algorithms are applied. For example, Lubrecht used a multi-level multi-integration algorithm in simulation of determining the elastic deformation in elastohydrodynamic lubrication [97]. This technique was also applied by Polonsky in simulation of rough dry contact [94]. A similar way is the application of the Fast Fourier Transformation (FFT), which has been recently very often involved in simulation of contact problems [98][99]. Both methods can dramatically reduce the complexity from $O(N^4)$ to $O(N^2 log N^2)$.

In the last two decades, adhesive contact has been frequently numerically simulated using BEM. The attractive interaction is often modeled by the Lennard-Jones potential [100][101], or the simple Maugis-Dugdale stress-separation law [102]. In 2015, Pohrt and Popov proposed a stress-based criterion to discriminate the detachment of surface elements for the simulation of adhesive contact based on the BEM [103]. The element will be 'detached' from the contacting surface once its stress exceeds the critical stress value. This stress criterion is based on the idea of Griffith by equating the increasing of the surface energy and the decrease in the elastic energy due to detaching of a surface element. The classic JKR theory is based on Griffith's idea of the energy balance as well, and thus, this BEM for adhesive contact numerically generates exactly the same results as the JKR theory. This BEM has become a very effective numerical tool, and it has been applied to adhesive contacts of indenters with complicated geometries, including toroidal indenter [104], elliptical shape [105], and flat stamp but with various shapes [74].

In this thesis, we use the BEM for simulation of adhesive contact of brush-structures and develop it further considering the elasticity of structures. The principles of the BEM including the discretization, influence matrix, Conjugated-gradient method for the inverse problem, are deeply discussed in Chapter 3.

1.4 Objectives of the work

In this work, we numerically study the adhesion behavior of rough brush-structures in contact with an elastic half-space. The pillars of brush-structure are modeled by rigid cylinders, which are *elastically embedded* into a common rigid base. These elastic connections can be considered as linear springs with stiffness k, as illustrated in Figure 1-4. For convenience, it will be called ***pillar stiffness*** generally in this thesis. One can consider the structure as elastically deformable fibrils with rigid tips. The displacement of pillars is

then coupled altogether via contact with the elastic half-space. The left side of Figure 1-4 shows such a flat brush-structure being in contact with an elastic half-space. The right figure illustrates an alternative model of rough brush-structure using a thin elastic layer [106], which is equivalent to the linear springs in the left figure. In this work, the following assumptions are made:

(1) Only normal contact is simulated.
(2) The stiffness of all springs (pillar stiffness) is identical. In biological microstructures, the fibrils are usually slender (much larger than the characteristic roughness), so their stiffness could be approximated as constant.
(3) The pillars (corresponding to the tip of bio-fibrils) are modeled as flat-ended cylinders.
(4) The effect of bunching among pillars is not considered.

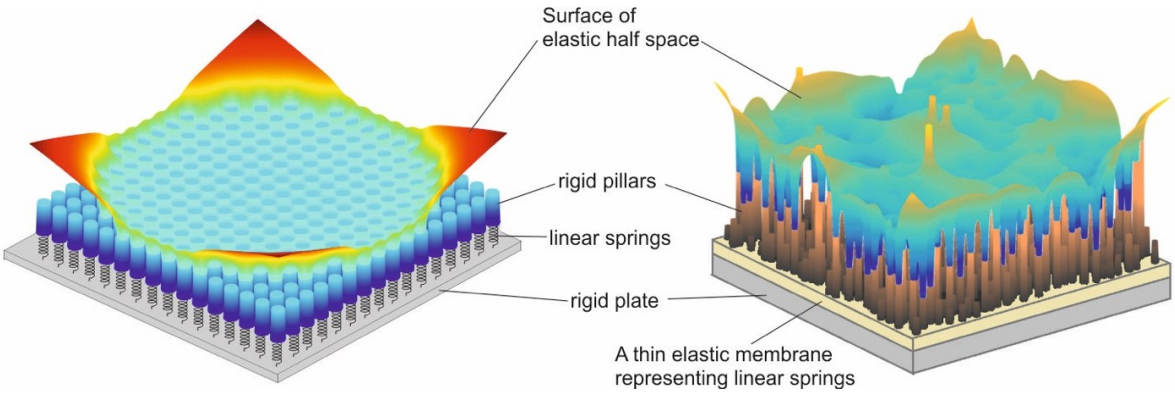

Figure 1-4 Illustration of adhesive contact between an elastic multi-pillar structure and an elastic half-space. Left: the rigid 'fibril tip' (pillars) are elastically connected to a rigid plate. Stiffness of pillars is modeled by linear springs. Right: an alternative model of rough contact where the linear springs are replaced by a very thin elastic membrane. The deflection of pillars is coupled by the contact with the elastic half-space.

For the adhesive contact of brush-structure, if the pillar stiffness is very large, the whole structure is regarded as a rigid body. The results of this rigid case have been analytically and numerically studied in [75]. If on the contrary the stiffness is extremely small compared with the contact stiffness, such 'contact splitting'-like results should be expected. In this work we consider brush-structures including flat and rough brush-structures, hierarchical- and optimal shaped structures, to bridge these two liming cases and investigate the influence of geometry parameters (such as roughness (length distribution of pillars) and density of pillar distribution), pillar stiffness, and loading parameters on adhesion.

To conduct simulations of these brush-structures, we develop the BEM with further consideration of the elasticity of connections in structures. The difficulty of simulation is the deformation correlation between pillars and the elastic half-space, and the elastic

interaction among pillars: the correction of any one pillar's displacement will cause the change of all other pillars' displacement. An effective algorithm is required for simulation of structures with a large number of pillars.

The sub-objectives are as follows:

(a) Development of an effective FFT-assisted BEM algorithm for simulation of adhesive contact of elastic brush-structures on an elastic half-space, where the pillar stiffness should be integrated into the BEM.

(b) Investigation of the adhesion behavior of different structures from flat structures, rough structures, and hierarchical- to optimal shaped structures.

(c) A general understanding of the influence of pillar stiffness, geometry parameters and loading parameter on adhesion in the cases of (b).

1.5 Outline

In Chapter 2, the pillar stiffness is introduced into two simple cases of a single indenter, including a flat cylindrical punch and a spherical cap. The existing BEM for rigid indenters developed in [103][107] is applied in simulation of adhesive contact of a single indenter. In Chapter 3, the FFT-assisted BEM is developed for effective simulation of adhesive contact of elastic brush-structures. In the developed BEM, the pillar stiffness is directly integrated into the influence matrix of the fundamental equation. A few examples of simulation results are shown for comparison with the results obtained by the method used in Chapter 2. In Chapter 4, the flat brush-structure is investigated numerically using the developed BEM. The influence of pillar stiffness, pillar number and filling factor on adhesion is studied in detail. In Chapter 5, the rough brush-structure, in which pillars' length follows the Gaussian distribution, is numerically studied. The adhesion coefficient in the preload-sensitive region, and the maximum adhesive force in the preload-insensitive region, are discussed. In Chapter 6, the BEM is further developed for the hierarchical structure, and the effect of structural hierarchy on adhesion is investigated. In Chapter 7, the artificial structure (the contact shape is artificially optimized) is studied for decreasing stress concentration and finding the optimal contact shape.

Chapter 2 Effect of pillar stiffness on adhesive contact of a single pillar

We start the study with a simple case of adhesive contact between a *single* pillar and an elastic half-space. We introduce the pillar stiffness into the numerical simulation through an easily understandable way: finding the equilibrium state of the pillar by correcting its position iteratively, based on the existing well-established Boundary Element Method (BEM) for the JKR-type adhesive contact of rigid indenters [74][103][107]. In two cases including a single cylindrical punch and a single spherical cap, the effect of pillar stiffness on adhesion is investigated. The external work for the complete separation is discussed.

2.1 Theoretical analysis of the external work of separation

We briefly review the classic problem of adhesive contact between a rigid flat-ended cylinder with radius r_c and an elastic half-space with elastic modulus E and Poisson's ratio ν. If the cylinder is pressed by an indentation depth d, the normal force is equal to [108]

$$F = 2E^* r_c d, \tag{2.1}$$

where E^* is the effective elastic modulus $E^* = E/(1-\nu^2)$. The contact stiffness can be expressed as

$$k_{cyl} = 2E^* r_c. \tag{2.2}$$

Thus, the elastic energy stored in the elastic half-space is given by $U_{el} = \frac{1}{2}k_{cyl}d^2 = E^* r_c d^2$, while the surface energy equals $U_{surf} = -\Delta\gamma\pi {r_c}^2$, where $\Delta\gamma$ represents the surface energy per unit area. The total energy of the system reads

$$U_{tot} = U_{el} + U_{surf} = E^* r_c d^2 - \Delta\gamma\pi {r_c}^2. \tag{2.3}$$

From Eq. (2.3), the critical indentation depth and the critical normal force as functions of radius are obtained [74][108]

$$d_K = -\sqrt{\frac{2\Delta\gamma\pi r_c}{E^*}}, \tag{2.4a}$$

$$F_K = -\sqrt{8E^*\Delta\gamma\pi {r_c}^3}. \tag{2.4b}$$

The external work for separating the two surfaces is

$$w_{ad} = \int_0^{d_K} 2E^* r_c d \, \mathrm{d}d = 2\Delta\gamma\pi r_c^2. \tag{2.5}$$

The work equals the elastic energy stored in the elastic half-space

$$U_{el} = E^* r_c d_K^2 = 2\Delta\gamma\pi r_c^2. \tag{2.6}$$

However, the energy used to create new surfaces (πr_c^2) is

$$\Delta U_{surf} = \Delta\gamma\pi r_c^2. \tag{2.7}$$

This means the total external work contains one part $\Delta\gamma\pi r_c^2$ for creating new surfaces, as well as another part $\Delta\gamma\pi r_c^2$, which will dissipate in elastic waves emitted into the elastic body [74].

Now we consider our model: the rigid cylinder (r_c) is elastically connected to a rigid base by a linear spring with stiffness k (as described in Chapter 1). We define this model as an *elastically embedded pillar*, and the *pillar stiffness* refers to the stiffness of spring, to indicate the elastic connection between the cylinder and the base.

For the adhesive contact of such an elastically embedded pillar on an elastic half-space, the entire system can be divided into two subsystems: one is the adhesive contact between the cylinder and the elastic half-space, and the other one is the elastic connection between the cylinder and the base.

For one single punch, it is clear that the existence of spring will not affect the critical values including the pull-off force F_K and the critical displacement (of the bottom of cylinder) d_K. However, more external work has to be done for separating the two bodies (extra energy is accumulated in the spring). The work of separation is then equal to the sum of elastic energy stored in the elastic half-space and in the spring

$$w_{ad} = 2\Delta\gamma\pi r_c^2 + \frac{1}{2}k\Delta l^2, \tag{2.8}$$

where Δl is the deflection of the elastically embedded pillar (i.e. $\Delta l + d_K$ is the critical displacement of the base). For such a system, it is noted that the deflections of the pillar and the elastic half-space within the contact region, are coupled under the loading condition.

Now we generalize the pull-off scenario of a single elastically embedded pillar with an arbitrary tip shape. When the general displacement of the rigid base (under the displacement-controlled condition) changes from d_0 (in a stable state) to d_1, the system approaches another stable state due to the stress balance between the pillar and the elastic half-space spontaneously. Considering adhesion, separation of some surface elements

could occur, which decreases the contact area, and further affects the stress balance. In order to find the final state, we follow the procedures described below:

1. Assume the contact area keeps unchanged, and then the pillar and the elastic half-space will deflect to reach a *virtual* balanced position, to satisfy force equilibrium.
2. If there are no elements detached from the contact area, then the state in step 1 is already the final stable state.
3. However, if partial separation occurs, the decreased contact area and the new corresponding stress distribution acting on the elastic half-space, are generated.
4. The forces acting on the pillar from the spring and from the elastic half-space are no longer in balance in step 3. One has to return to step 1 to repeat the above procedures, until the condition of force equilibrium is satisfied or the complete detachment occurs.

The determination of the element detachment in the numerical simulation will be described in the next section. Since the contact area can only decrease, the iteration of these procedures is guaranteed to terminate, and then only *two* possible states will be obtained: either the final stable state is reached, or the complete separation is accomplished.

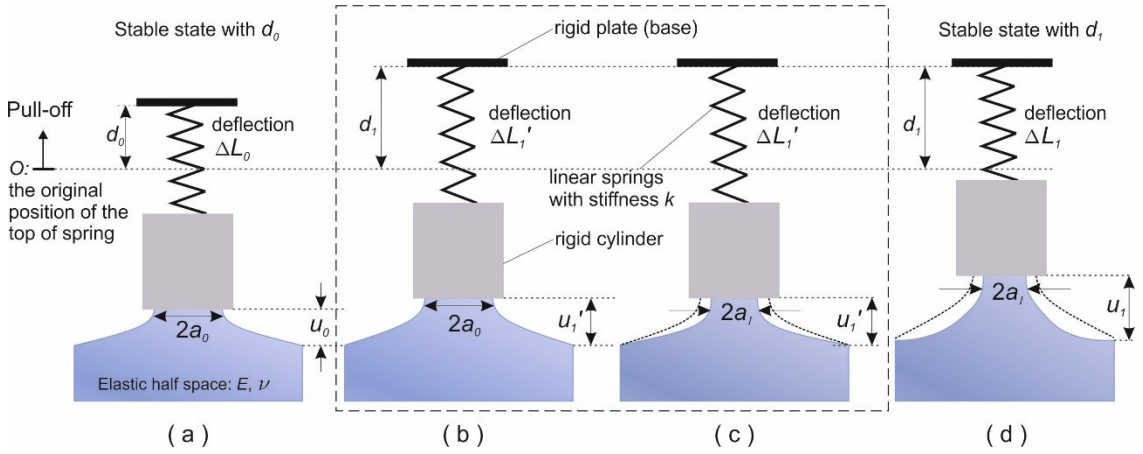

Figure 2-1 Illustration of the separation of a single elastically embedded pillar from an elastic half-space. (a) is the stable contact state with displacement d_0; (d) is the stable contact state with displacement d_1. (b) and (c) are two virtual states described in step 1 and step 3 above.

In Figure 2-1, we illustrate a simple example to explain the procedures described above. (a) and (d) are two stable states before and after the change of the (controlled) displacement (of the base) from d_0 to d_1. We perform the procedure in step 1 to get the virtual state (b), and then due to separation, we obtain the state (c) (as in step 3). The system is solved again (by performing the procedure in step 1 again) to reach the final state (d). In next section, we follow the procedures to realize the numerical simulation.

2.2 Numerical implementation based on the BEM

We use the FFT-assisted BEM for rigid indenter developed in [107], to simulate the contact between an elastically embedded pillar and an elastic half-space. The fundamental equation for the relationship between the stress p acting on the elastic half-space and the displacement distribution u, can be written as [96]

$$u = \int K(x - x')p(x)\mathrm{d}x' = K * p, \tag{2.9a}$$

where '$*$' means convolution operation, and K is the influence coefficient depending on the type of contact, for example the Boussinesq's solution to the normal displacement generated by the normal stress [96]. In the BEM, the relation above can be rewritten in a discrete form as

$$u_{ij} = K_{iji'j'}p_{i'j'}, \tag{2.9b}$$

where u_{ij} is the displacement of surface element at position (i, j), $p_{i'j'}$ is stress acting on the element (i', j'). The stress acting on a discrete element is assumed *constant* inside the element mesh [107]. For a given displacement u, the corresponding stress distribution p can be obtained with the help of the conjugate-gradient method [94].

Here, we do not deeply discuss the BEM, and more details such as the theoretical formulation, the numerical discretization, and its further development will be presented in Chapter 3. We only address that using this existing BEM one can realize the simulation of indentation test: with the given surface geometry of the rigid indenter, the load (either the indentation depth or the force) and the material parameters, the contact area and stress distribution can be calculated.

With the help of the BEM, we can construct the procedures of numerical simulation, as described in previous section.

2.2.1 Determination of balanced position

Now we consider the contact case of a single elastically embedded pillar. For a given displacement of the base d (which is called *general displacement* in the following content), there are two parts of deflection: one is the deflection of the elastic half-space u, and the other one is the deflection of the pillar Δl (as shown in Figure 2-1). The geometrical condition within the contact are A is given by

$$d = u + \Delta l. \tag{2.10}$$

The equilibrium of forces acting on the pillar from the spring and from the elastic half-space is

$$F = k\Delta l = \int_A p\mathrm{d}A = \sum_A ph^2\,, \tag{2.11}$$

where h is the size of the square element of discretization, and p is the pressure distribution within the contact area.

A simple way for determining the deflection of the pillar (as well as the corresponding deflection of the elastic half-space within the contact area) is the following. We can start with an initial value of the pillar's deflection Δl_0 (for example $\Delta l_0 = d/2$). The indentation depth of the pillar is then equal to $u_0 = d\text{-}\,\Delta l_0$. With the help of the BEM, we obtain the corresponding stress distribution $p(u_0)$ as well as the normal force $\sum ph^2$ acting on the elastic half-space. Comparing this normal force with the spring force F, one can correct the position of the pillar by a value Δd. Repeat this procedure, until the balance condition Eq. (2.11) is met (or the difference r_{err} between these two forces is small enough). A scheme for the numerical implementation is shown in Figure 2-2.

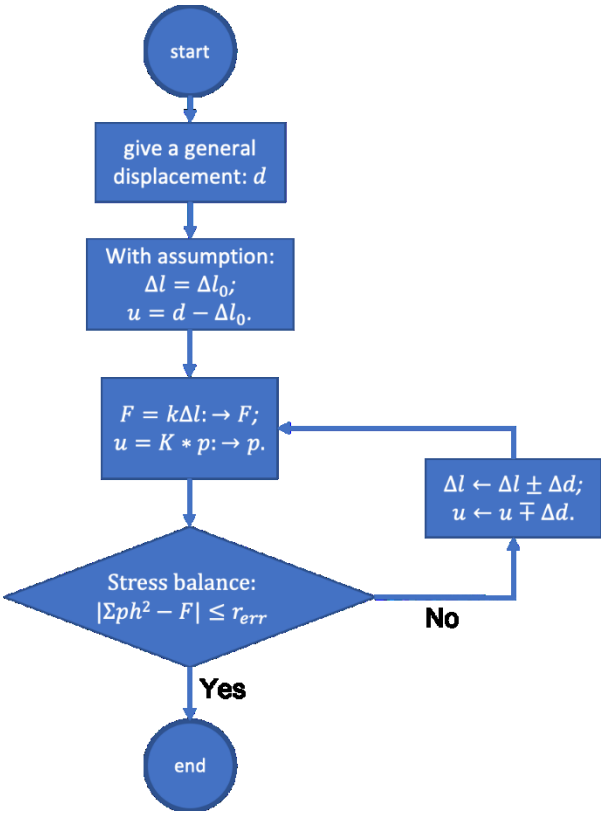

Figure 2-2 Flow chart of determination of the pillar's balanced position.

2.2.2 Criterion of detachment in adhesive contact

Considering adhesion, the mesh-dependent stress criterion is used in the BEM to determine the detachment of elements [74][103]: It is based on the Griffith's crack theory: the elastic energy stored in the contacting bodies will be released to accomplish the adhesion work needed to create new surfaces. For a discrete element with size h in the BEM, it will detach once the elastic energy $U_{el,mesh}$ stored in it exceeds the surface energy $\Delta U_{surf,mesh}$. The surface energy is simply equal to

$$\Delta U_{surf,mesh} = \Delta\gamma h^2. \tag{2.12}$$

The elastic energy in this element in the framework of the BEM was first found in [103]

$$U_{el,mesh} = \frac{1}{2}\int_{mesh} pu\mathrm{d}A = 0.473201\frac{p_{mesh}^2}{E^*}h^3, \tag{2.13}$$

where p_{mesh} is the local stress acting on this element, and it is assumed constant within the mesh. The critical condition is determined by $U_{el,mesh} = \Delta U_{surf,mesh}$ for $p_{mesh} = \Sigma_c$. The corresponding critical stress is given by

$$\Sigma_c = \sqrt{\frac{E^*\Delta\gamma}{0.473201 \cdot h}}. \tag{2.14}$$

For stress distribution p over the contact zone in discrete form, we elementally compare them with the critical value Σ_c and exclude those elements from the contact region, whose tensile stress are larger than Σ_c. This method can numerically reproduce the JKR-solution with very high accuracy.

Now we apply this detachment criterion in the adhesive contact of elastically embedded pillar. As described in Section 2.1, we firstly determine the virtual balanced position by the method in last subsection. Then we apply this local stress criterion Σ_c, to remove those detached elements and to correct the contact area. The whole numerical process is illustrated in Figure 2-3.

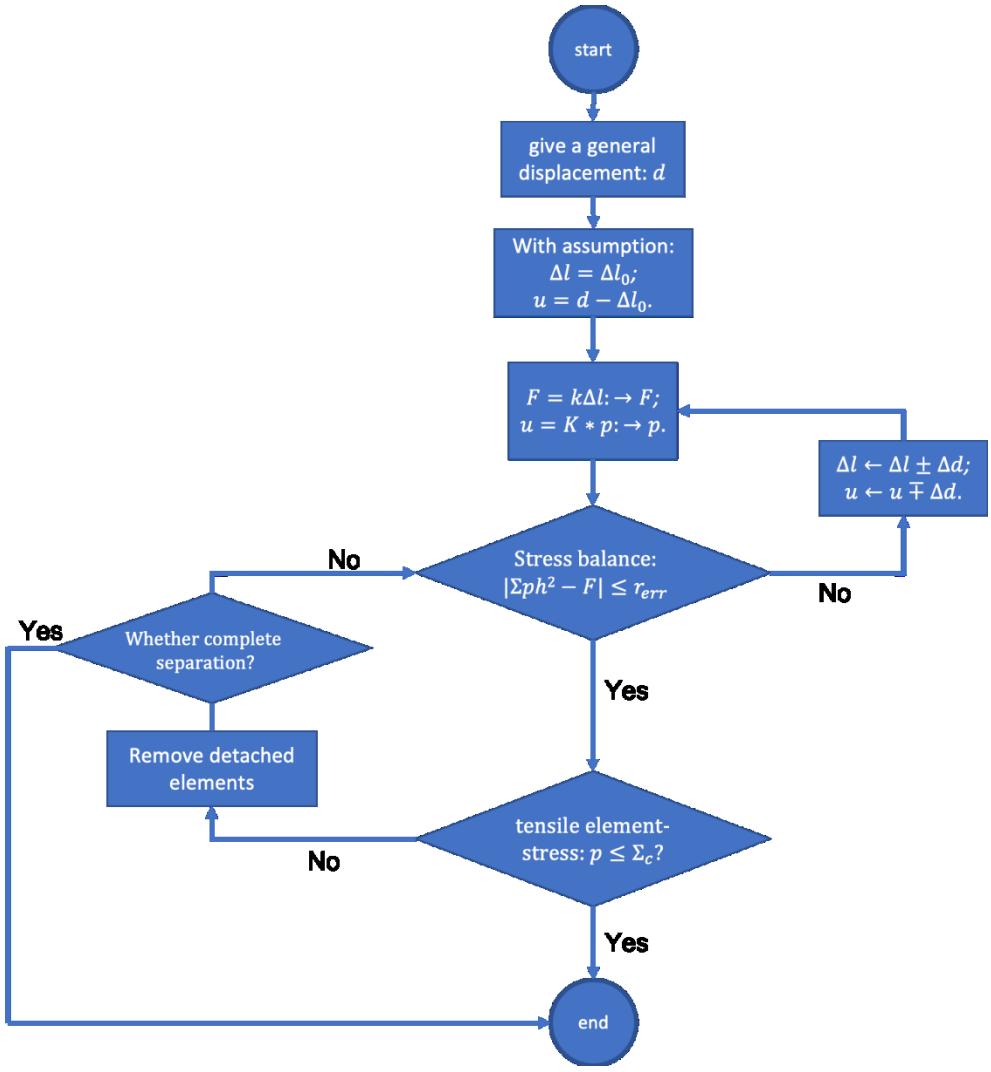

Figure 2-3 Flow chart of determination of the pillar's balanced position in adhesive contact.

After removing detached elements, the stress inside the contact area has to be recalculated, and then used to compare with the spring force for determining the new equilibrium state. As mentioned before, the contact area can only decrease in pull-off simulation, so the iteration is guaranteed to terminate.

2.3 Results and discussion

In this section, we study two cases using the method described above. The pillar's shape has a form of flat cylindrical punch or spherical cap. *Displacement-controlled* pull-off of a system composed of such a pillar and elastic connection, is numerically simulated. The effect of pillar stiffness (i.e. spring stiffness) on adhesion is investigated, and analytical solutions to the work of separation are given for comparison with numerical results.

2.3.1 Flat cylindrical punch

2.3.1.1 Pull-off process

We firstly simulate the adhesive contact between a flat cylindrical punch and an elastic half-space. The whole simulation zone is $L \times L = 1\,\text{mm} \times 1\,\text{mm}$, and the radius of the punch is set $r = 0.3\,\text{mm}$. Stiffness varies from $1\,N/\text{mm}$ to $10000\,N/\text{mm}$. For the dimensionless comparison, we normalize normal force F and the displacement d by the Kendall's solution with $F_K = \sqrt{8E^*\Delta\gamma\pi r^3}$, $d_K = \sqrt{2\Delta\gamma\pi r/E^*}$ [108]:

$$\tilde{F} = \frac{F}{F_K};\ \ \tilde{d} = \frac{d}{d_K}. \tag{2.15}$$

The contact radius a and the pillar stiffness k are normalized as follows:

$$\tilde{a} = \frac{a}{r};\ \ \tilde{k} = \frac{k}{2E^*r}. \tag{2.16}$$

The corresponding dimensionless stiffness $\tilde{k}$ varies from 0.01 to 100. Figure 2-4 shows curves of load-displacement for different stiffnesses, and Figure 2-5 shows curves of load-contact radius.

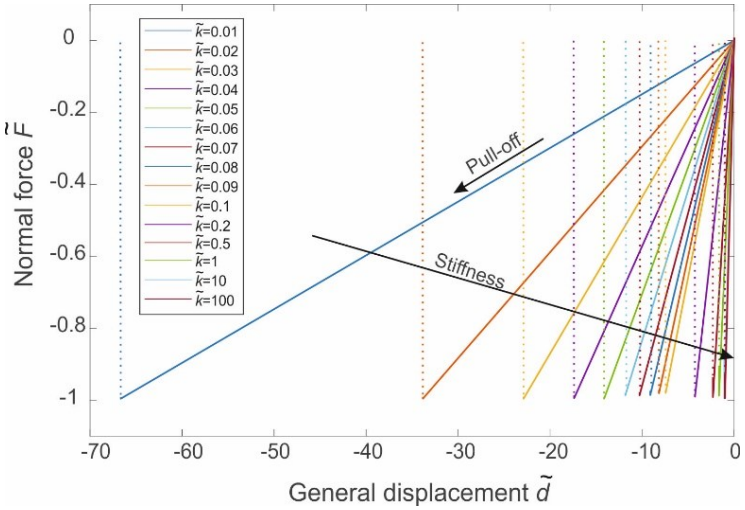

Figure 2-4 Pull-off process of flat punch with different stiffnesses.

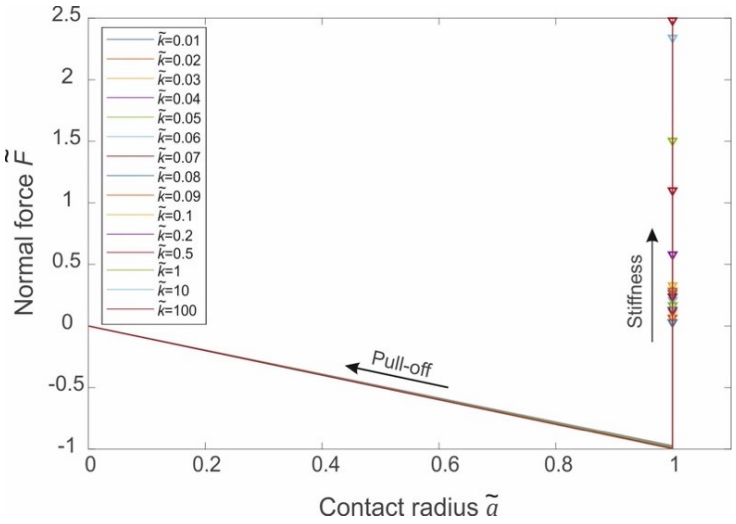

Figure 2-5 Relation between the normal force and the contact radius. 'Triangles' represent the initial applied forces for different stiffnesses to obtain the same initial general displacement.

It is seen that the pull-off process of elastic systems is very similar to it of the rigid case: the normal force is linearly increased with displacement till to the complete separation. With the decrease of stiffness, the critical displacement becomes larger. In the case of the smallest $\tilde{k} = 0.01$ (the blue line in Figure 2-4), the critical displacement reaches 67 times larger than it of the rigid case. The curves of force-contact radius for different stiffnesses are practically the same, as shown in Figure 2-5. The contact area keeps unchanged during the pull-off, and detachment does not appear until the maximum tensile force (the pull-off force) appears, then the complete separation accomplishes.

2.3.1.2 Work of separation

Let us discuss the influence of pillar stiffness on the external work for complete separation. We define that the work of separation is accumulated from the zero-indentation to the complete separation. At the critical state, the whole system is in balance under the condition

$$F_K = \sqrt{8E^*\Delta\gamma\pi r^3} = k\Delta l. \tag{2.17}$$

We can calculate the deflection of the pillar $\Delta l = \frac{1}{k}\sqrt{8E^*\Delta\gamma\pi r^3}$. Then according to Eq. (2.8), the work of separation reads

$$w_{ad} = 2\Delta\gamma\pi r^2 + \frac{1}{2}\frac{1}{k}(8E^*\Delta\gamma\pi r^3) = \Delta\gamma\pi r^2\left(2 + \frac{4E^* r}{k}\right). \tag{2.18}$$

The external work for the rigid case $w_K = 2\Delta\gamma\pi r^2$ (in Eq. (2.5)), is used to normalize the work in Eq. (2.18):

$$\widetilde{w} = \frac{w_{ad}}{w_K} = \left(1 + \frac{1}{\tilde{k}}\right). \tag{2.19}$$

Then we get the relation between the work of separation and the pillar stiffness, as shown in Figure 2-6.

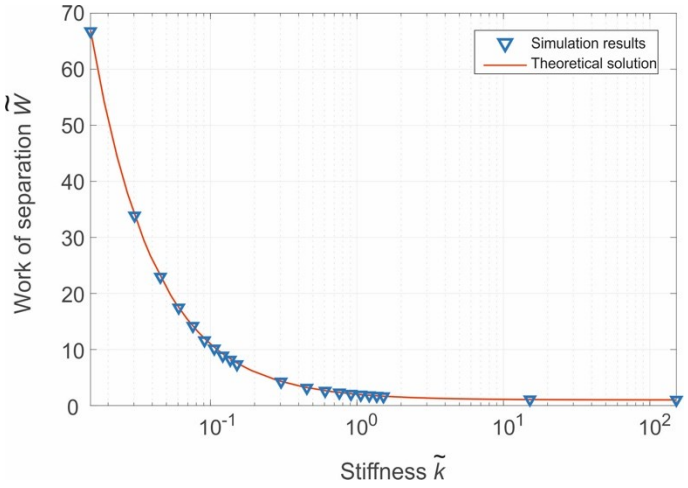

Figure 2-6 Dependence of the work of separation on the pillar stiffness.

Figure 2-6 shows that the numerical results agree with the theoretical estimation Eq. (2.19) well. For cases of very small stiffness, for example $\tilde{k} = 0.015$, the work of separation can be much higher than it of the rigid case (over 65 times). The work $\widetilde{w}$ decreases rapidly with stiffness. In the case of $\tilde{k} = 0.3$, the work $\widetilde{w}$ reduces to 4.26, while it is nearly 1.64 in the case of $\tilde{k} = 1.5$.

2.3.2 Spherical cap

2.3.2.1 Pull-off process

A spherical cap with radius $R = 0.3\text{mm}$ is numerically simulated as well. It is noted that we will regulate the initial general displacement for different pillar stiffnesses, to ensure all indenters obtain the same initial contact area. We normalize values by the JKR solution [42][109]

$$F_{JKR} = \frac{3}{2}\pi R\Delta\gamma; \tag{2.20a}$$

$$d_{JKR} = -\left(\frac{3\pi^2\Delta\gamma^2 R}{64E^{*2}}\right)^{\frac{1}{3}};\ \ a_{JKR} = \left(\frac{9}{8}\frac{\Delta\gamma\pi R^2}{E^*}\right)^{\frac{1}{3}}. \tag{2.20b}$$

$$\tilde{F} = \frac{F}{F_{JKR}};\ \tilde{d} = \frac{d}{d_{JKR}};\ \tilde{a} = \frac{a}{a_{JKR}};\ \tilde{k} = \frac{k}{E^* a_{JKR}} \tag{2.21}$$

Figure 2-7 shows the relation load-displacement for different stiffnesses. The black dashed line represents the typical JKR curve of the rigid case. It can be found that adhesive force is the same for all stiffness cases, but the critical displacement becomes larger when the stiffness decreases, and then more external work needs to be done for separation.

On the typical JKR curve, the maximum value of normal force (in the tensile state) appears at the point C, where $F = F_{JKR}$. While the complete separation appears at the point D (the minimum of displacement) under the *displacement-controlled* condition. These two points (C and D) approach each other as stiffness decreases. For example, in the cases of small stiffness $\tilde{k} = 0.19,\ 0.26,\ 0.32$ (the yellow, purple and green curves on the left side of Figure 2-7), the complete separation occurs close to the critical moment of the pull-off force (i.e. the point C).

Equivalently, it can be seen that the complete separation moment tends to the point C when stiffness decreases. Therefore, for small stiffness cases, the system becomes much unstable after the point C, and thus, a slight perturbation of displacement (after C) could result in an irreversible crack propagation till to the complete separation.

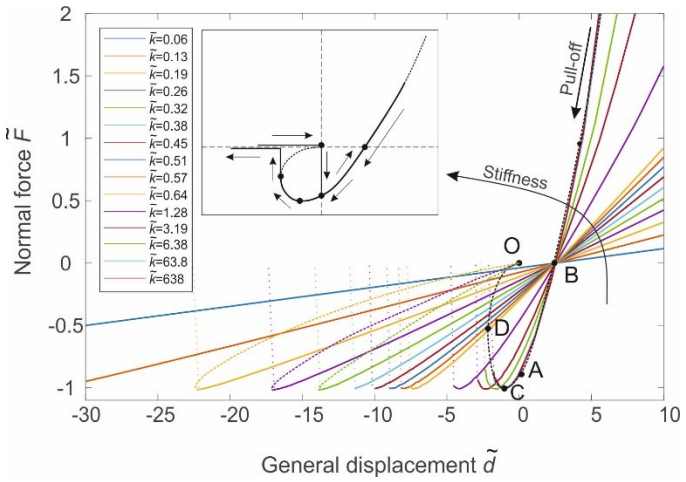

Figure 2-7 Pull-off processes of spherical caps with different stiffnesses. The black dashed line represents the JKR curve of the rigid case.

For relation of the normal force and the contact radius in Figure 2-8, all cases have roughly similar processes compared with the JKR curve, but a slightly earlier detachment moment is observed for cases of smaller stiffness.

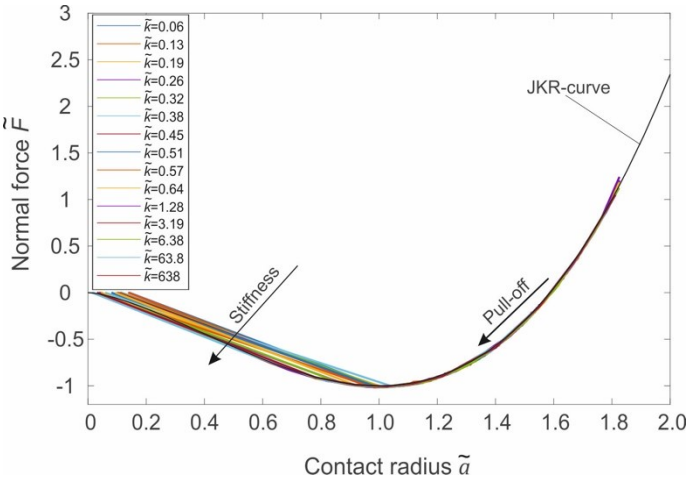

Figure 2-8 Relation between the normal force and the contact radius for different stiffnesses.

2.3.2.2 Work of separation

For the work of separation, we noticed the complete separation moment is different for cases of large and small stiffness. We start with the JKR case (rigid indenter with contact radius a). The contact radius - force (a-F) relation is given by [46][109]

$$F = E^*\left(\frac{4}{3}\frac{a^3}{R} - \left(\frac{8\Delta\gamma\pi a^3}{E^*}\right)^{\frac{1}{2}}\right), \tag{2.22}$$

then the total energy of the system can be expressed as

$$U_{tot} = E^*\left(d^2 a - \frac{2}{3}\frac{da^3}{R} + \frac{a^5}{5R^2}\right) - \Delta\gamma\pi a^2. \tag{2.23}$$

The first term represents the elastic energy stored in the elastic half-space, and the second term represents the surface energy. We have the dimensionless relation of a-F and a-d [109]

$$\tilde{F} = \tilde{a}^3 - 2\tilde{a}^{\frac{3}{2}};\ \tilde{d} = 3\tilde{a}^2 - 4\tilde{a}^{\frac{1}{2}}. \tag{2.24}$$

Let $\tilde{F} = 0$, we obtain the contact radius a_0 in the corresponding state (i.e. the point B in Figure 2-7), $\tilde{a}(a_0) = 2^{\frac{2}{3}}$. Then we can calculate the total energy at contact radius a_0

$$U_{tot,0} = U_{tot}(a_0). \tag{2.25}$$

Let $\frac{\mathrm{d}\tilde{d}}{\mathrm{d}\tilde{a}} = 0$, we obtain the contact radius a_s at the complete separation moment (the point D in Figure 2-7), $\tilde{a}(a_s) = \left(\frac{1}{3}\right)^{\frac{2}{3}}$, and the corresponding force is $\tilde{F}(a_s) = -\frac{5}{9}$. The total energy at contact radius a_s is

$$U_{tot,s} = U_{tot}(a_s). \tag{2.26}$$

We define that the work of separation for spherical cap is counted from the point B to the complete separation moment. Then the work of the rigid case is equal to

$$\boldsymbol{w_0} = U_{tot,s} - U_{tot,0}. \tag{2.27}$$

Now we consider the influence of pillar stiffness *k*. The elastic energy stored in the pillar is $U_{sp} = \frac{1}{2}k\Delta l^2$, and the total energy can be expressed as

$$U_{tot,sp} = U_{tot} + U_{sp}. \tag{2.28}$$

At contact radius $a = a_o$ (the point B), $\tilde{F} = 0$ implies no deflection of the pillar, and thus

$$U_{tot,sp}(a_0) = U_{tot}(a_0) = U_{tot,0}. \tag{2.29}$$

For *large* stiffness cases, we can assume that it has similar behavior to the rigid case. Therefore, at the separation moment (i.e. the point D), the force is equal to $F_s = -\frac{5}{6}\pi R\Delta\gamma$. Then we can calculate the elastic energy stored in the pillar as $U_{sp,h} = \frac{F_s^2}{2k} = \frac{1}{2k}\left(\frac{5}{6}\pi R\Delta\gamma\right)^2$, and the work of separation is equal to

$$\boldsymbol{w_{ad,h}} = U_{tot,sp}(a_s) - U_{tot,0}. \tag{2.30}$$

However, for *small* stiffness cases, we assume that the complete separation happens at the point C, so the force is then the pull-off force $F_c = -\frac{3}{2}\pi R\Delta\gamma$ (the adhesive force), and the elastic energy stored in the pillar reads $U_{sp,l} = \frac{F_c^2}{2k} = \frac{1}{2k}\left(\frac{3}{2}\pi R\Delta\gamma\right)^2$. Then the work is given by

$$\boldsymbol{w_{ad,l}} = U_{tot,sp}(a_c) - U_{tot,0}. \tag{2.31}$$

2.3.2.3 Work of separation in dimensionless form

We substitute d with a ($d = \frac{a^2}{R} - \sqrt{\frac{2\Delta\gamma\pi a}{E^*}}$ [109]), and the total energy can be rewritten as

$$U_{tot,sp} = \left[\frac{8}{15}\frac{E^*}{R^2}a^5 - \frac{2}{3}\frac{\sqrt{8\pi\Delta\gamma E^*}}{R}a^{\frac{7}{2}} + 2\pi\Delta\gamma a^2\right] + [-\pi\Delta\gamma a^2] + \frac{1}{2k}a^3\left[\frac{4}{3}\frac{E^*}{R}a^{\frac{3}{2}} - \sqrt{8\pi\Delta\gamma E^*}\right]^2. \tag{2.32}$$

The first term represents the elastic energy in the elastic half-space, the second term represents the surface energy, and the last term represents the elastic energy stored in the pillar. Now we introduce two new terms for normalization and we have parameters [110]

$$a_{nor} = \left(\frac{\pi \Delta\gamma R^2}{2E^*}\right)^{\frac{1}{3}};\ \ \bar{a} = \frac{a}{a_{nor}}; \tag{2.33}$$

$$U_{nor} = \left(\frac{\pi^5 \Delta\gamma^5 R^4}{2^5 E^{*2}}\right)^{\frac{1}{3}};\ \ \bar{U} = \frac{U}{U_{nor}}. \tag{2.34}$$

Then we can rewrite the total energy as

$$\bar{U}_{tot,sp} = \left[\frac{8}{15}\,\bar{a}^5 - \frac{8}{3}\,\bar{a}^{\frac{7}{2}} + 4\bar{a}^2\right] + [-2\bar{a}^2] + \frac{8}{9}\frac{E^*\bar{a}}{k}\,\bar{a}^3\left[\bar{a}^{\frac{3}{2}} - 3\right]^2. \tag{2.35}$$

Furthermore, we normalize the pillar stiffness k as

$$\bar{k} = \frac{k}{E^* a_{nor}}. \tag{2.36}$$

Hence,

$$\bar{U}_{tot,sp} = \frac{8}{15}\bar{a}^5 - \frac{8}{3}\bar{a}^{\frac{7}{2}} + 2\bar{a}^2 + \frac{8}{9}\frac{1}{\bar{k}}\,\bar{a}^3\left(\bar{a}^{\frac{3}{2}} - 3\right)^2. \tag{2.37}$$

For the rigid case, the last term disappears ($\frac{1}{\bar{k}} \to 0$). Finally, the work of separation in dimensionless form reads

$$\bar{\boldsymbol{w}}_{\boldsymbol{ad,h}} = \frac{\bar{U}_{tot,sp}(\bar{a}_s) - \bar{U}_{tot}(\bar{a}_o)}{\bar{U}_{tot}(\bar{a}_s) - \bar{U}_{tot}(\bar{a}_o)}; \tag{2.38}$$

$$\bar{\boldsymbol{w}}_{\boldsymbol{ad,l}} = \frac{\bar{U}_{tot,sp}(\bar{a}_c) - \bar{U}_{tot}(\bar{a}_o)}{\bar{U}_{tot}(\bar{a}_s) - \bar{U}_{tot}(\bar{a}_o)}. \tag{2.39}$$

Compared with the numerical results, we use $\bar{w}_{ad,l}$ for cases of $\bar{k} < 1.7$, and $\bar{w}_{ad,h}$ for other cases, then we obtain a reasonable fitting result, as shown in Figure 2-9. Similarly, it is found that only in a very narrow zone, the work can be very high. It rapidly approaches the result of the rigid case as stiffness increases.

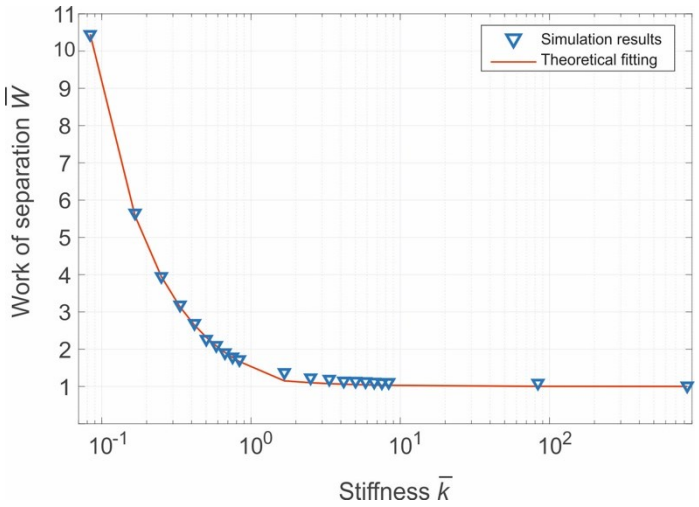

Figure 2-9 The work of separation for different stiffnesses.

2.4 Conclusions

In this chapter, we designed an iterative method to study the adhesion behavior of a single elastically embedded pillar in contact with an elastic half-space, based on the existing BEM for rigid indenters. Two cases including flat cylindrical punch and spherical cap with different pillar stiffnesses, were numerically simulated. It has been found that the work of separation varies with the pillar stiffness. For the flat punch with very small stiffness, the external work could be over 60 times larger than that of the rigid case, and numerical results agreed with the theoretical estimation well. For the spherical cap with very small stiffness, the complete separation moment approached the critical moment of the adhesive force. It is found small stiffness leads to the system becoming unstable (after achieving the adhesive force).

Chapter 3 Development of the BEM for adhesive contact of elastic brush-structure

The iterative method used for a single pillar in previous chapter could also be theoretically applied for simulation of (adhesive) contact of multiple pillars. However, in the latter case, the correction of any pillar's position will induce the change in deflection of all other pillars, which results in many cumbersome operations. Thus, the computing cost will be huge. For a brush-structure with a large number of pillars, it is impossible to individually correct the deflection of all pillars. Therefore, we reconsider the force-displacement relation for this system and find a more appropriate way to solve the contact problem.

In this chapter, the pillar stiffness is directly introduced into the fundamental equation as well as the influence matrix of the BEM. The further development based on the existing BEM enables the numerical simulation much faster and more accurately in comparison with the iterative method.

Part of the work in this chapter appears in paper: He, X.; Li, Q.; Popov, V. L. Simulation of Adhesive Contact of Soft Microfibrils. Lubricants, 2020, 8, 94. doi.org/10.3390/lubricants8100094. My contribution (in accordance with the content of this chapter) is the following: He X proposed the theoretical model (section 3.2). He X developed the numerical method: this part is described in section 3.2 including Figure 3-2 to Figure 3-3 and equations Eq. (3.8) to Eq. (3.17). All the authors contributed in preparing the manuscript. All authors reviewed the manuscript.

3.1 Fundamentals of the BEM

For liner elastic contact problems, the surface displacement of elastic half-space under traction is calculated by an integral equation. The solution to the normal contact was given by Boussinesq [96]: the normal displacement of the elastic half-space $u(x,y)$ at position (x,y) under the normal stress distribution p acting on position (x',y') is equal to

$$u(x,y)=\frac{1}{\pi E^*}\int_X\int_Y\frac{1}{\sqrt{(x-x')^2+(y-y')^2}}\,p(x',y')\mathrm{d}x'\mathrm{d}y', \tag{3.1}$$

where E^* is the effective elastic modulus of the elastic half-space. We can write Eq. (3.1) in a simplified form

$$u(x,y)=\int_X\int_Y S(x-x',y-y')\,p(x',y')\mathrm{d}x'\mathrm{d}y'. \tag{3.2}$$

For a numerical model, we discretize the simulation domain into regular element meshes with size $h_x \times h_y$ as shown in Figure 3-1. Then u_{ij} is the displacement of surface element at position (i, j) in two-dimensional discretization, and $p_{i'j'}$ is the *uniform* normal stress inside the element (i', j'). Eq. (3.2) can be rewritten in a discrete form as

$$u_{ij} = \sum_{i'} \sum_{j'} K_{iji'j'} p_{i'j'}\,, \tag{3.3}$$

with influence matrix

$$K_{iji'j'} = \int_{y_{j'}-\frac{h_y}{2}}^{y_{j'}+\frac{h_y}{2}} \int_{x_{i'}-\frac{h_x}{2}}^{x_{i'}+\frac{h_x}{2}} S(x-x', y-y')\,\mathrm{d}x'\mathrm{d}y'. \tag{3.4}$$

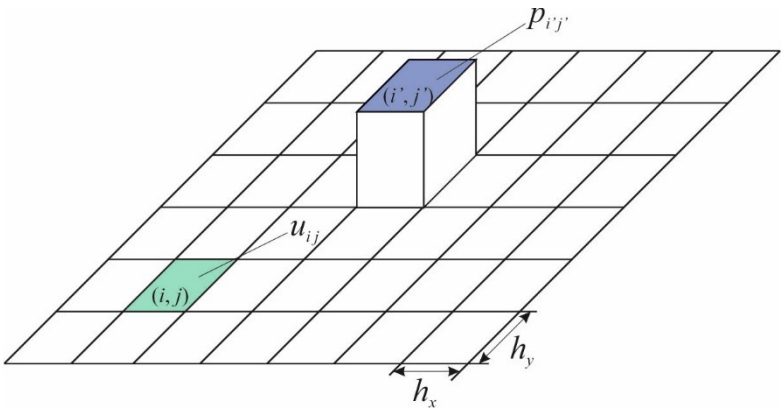

Figure 3-1 Discretization of the simulation domain and the uniform stress distribution inside a mesh grid.

For the BEM with regular mesh grid, the influence coefficient $K_{iji'j'}$ in Eq. (3.4) can be analytically evaluated [107]

$$\begin{aligned} K_{iji'j'} = \frac{1}{\pi E^*} \cdot \Big(& s \ln \frac{m+\sqrt{m^2+s^2}}{n+\sqrt{n^2+s^2}} + t \ln \frac{n+\sqrt{n^2+t^2}}{m+\sqrt{m^2+t^2}} \\ & + m \ln \frac{s+\sqrt{s^2+m^2}}{t+\sqrt{t^2+m^2}} + n \ln \frac{t+\sqrt{t^2+n^2}}{s+\sqrt{s^2+n^2}} \Big), \end{aligned} \tag{3.5}$$

with

$$s = (i'-i+0.5)h_x, \qquad m = (j'-j+0.5)h_y,$$

$$t = (i'-i-0.5)h_x, \qquad n = (j'-j-0.5)h_y.$$

If the surface is discretized with dimension $N \times N$, then the stress p and displacement u have the same dimension $N \times N$, but the matrix of influence coefficient K will be usually transferred to a dimension $N^2 \times N^2$ in the system of linear equations. The matrix of

influence coefficient K is dense (not a diagonal-dominant coefficient matrix). A direct calculation of the system of linear equations requires large computer memory and is very time-consuming. As mentioned in Section 1.3, the system of linear equations Eq. (3.3) can be solved with the help of the Fast Fourier Transform (FFT), which reduces the complexity largely from $O(N^4)$ to $O(N^2 log N^2)$. This technique has been applied by many researchers [99]. Before carrying the FFT, the matrix of influence coefficient is usually constructed in the "convolution" form of having the same dimension $N \times N$ as the pressure and displacement distribution. Then Eq. (3.3) can be expressed as

$$u = K * p, \tag{3.6}$$

and the operation of FFT is then pointwise multiplication

$$u = \mathrm{IFFT}[\mathrm{FFT}(K) \cdot \mathrm{FFT}(p)]. \tag{3.7}$$

As suggested by Liu et al. [111], for the non-periodic contact in a finite domain, matrices of pressure and influence coefficient should be expanded to dimension $2N \times 2N$, in which zero padding and wraparound order in this doubled domain must be performed to execute cyclic convolution. After the inverse FFT, the displacement u is then extracted from the obtained displacement with the same doubled dimension.

Furthermore, a conjugate-gradient technique (CG), which was introduced by Polonsky and Keer for normal rough contact problem [94], is applied to solve the inverse problem [107]. It takes the deflection u as the input inside the contact zone, to inversely determine the necessary stress p corresponding to the given deflection. With the development of computing technology in recent years, other techniques have also been applied into the BEM for improving computing efficiency. For example, the 'FFT-based Approximate Inverse' preconditioner [98] is used for the acceleration of converge rate of the inverse problem, and the parallel calculation on GPU for speeding up the FFT operation.

With the combination of the techniques above, many tests in contact mechanics can be effectively realized in the framework of the BEM. With the given arbitrary geometry of rigid indenter and material parameters of the elastic half-space, one can carry out the displacement- or force-controlled indentation simulations. The stress distribution and contact area can be very quickly calculated. This method has been applied in various contact problems including partial sliding with Coulomb's law of friction [112], wear based on the Archard' law of wear [113], and adhesion, etc.

3.2 Numerical modeling of elastic brush-structures

We follow the basic work above to study the brush-structure with a large number of *elastically embedded pillars*. It is noticed again that the elastic deformability of pillars has been modeled by considering them as rigid cylinders elastically coupled to a common rigid plate. Under the loading, interaction between pillars and elastic half-space must be coupled to the elastic connection between pillars and the rigid plate.

3.2.1 Determination of balanced position of elastically embedded pillars

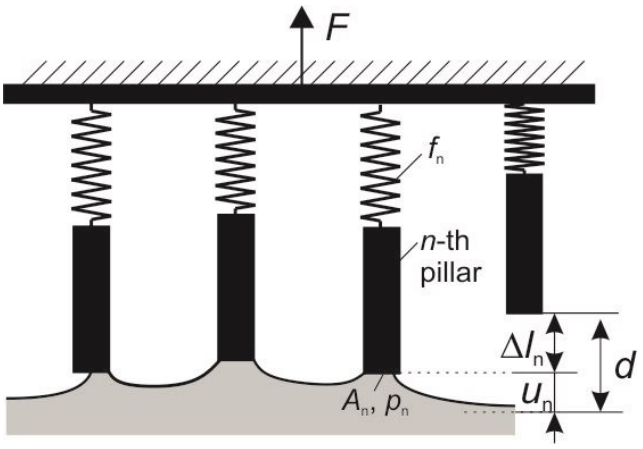

Figure 3-2 Sketch of adhesive contact between a flat elastically deformable brush-structure and an elastic half-space. The pillars are embedded into a rigid plate elastically, so that each pillar acts as a linear spring. Under the loading, the pillars will be stretched and the interaction between pillars and elastic half-space must be evaluated.

Now we integrate the displacement of elastically embedded pillars into the current FFT-based BEM. Figure 3-2 illustrates that a flat brush-structure with the identical stiffness k under a tensile state. Considering a total displacement d, for the n-th pillar within the contact region A_n, the following relation is satisfied

$$d = \Delta l_n + u_n. \tag{3.8}$$

The force on spring equals the force on the pillar

$$f_n = k\Delta l_n = \int_{A_n} p_n \mathrm{d}A\,. \tag{3.9}$$

Substitution of Eq. (3.9) into Eq. (3.8) yields

$$d = \frac{1}{k}\int_{A_n} p_n \mathrm{d}A_n + u_n. \tag{3.10}$$

Based on the BEM described in last subsection, u_n and p_n are transferred to matrix form in two-dimensional discretization, then Eq. (3.10) can be rewritten in a discrete form

$$d = \frac{1}{k}\sum_{A_n} p_n h^2 + u_n. \tag{3.11a}$$

From the discrete form of p_{ij} and u_{ij}, it can be rewritten as

$$d = \frac{1}{k}\sum_{(i,j)\in A_n} p_{ij}h^2 + u_{ij};\ \ (i,j) \in A_n. \tag{3.11b}$$

One can solve this contact problem numerically with the help of the existing BEM as described in the pervious chapter. Nevertheless, the difficulty for this case is due to the elastic interaction of pillars on each other. The iteration cannot be realized if the number of pillars is large, because correction of position for one pillar will induce the position change of others. Due to the complicated interactions among the pillars, the iteration takes much time and the results are usually not accurate. In the following content, this iterative method is called 'nested-loop' method.

Instead of determining every single pillar's balance position separately, it would be more effective if all pillars' correct positions could be found simultaneously. To accomplish this target, we suggest another solution to this problem.

3.2.2 A universal method for elastic brush-structure

From Eq. (3.11), the deflection of *n*-th pillar in discrete form can be expressed as

$$\Delta l_{ij;(i,j)\in A_n} = \frac{h^2}{k}\sum_{A_n} p_{ij} = \frac{h^2}{k}\left(\sum_{(i,j)\in A_n} 1\cdot p_{ij} + \sum_{(i,j)\notin A_n} 0\cdot p_{ij}\right), \tag{3.12}$$

and the operation of sum in Eq. (3.12) can be written in *convolution form* by introducing a new influence coefficient Π

$$\Delta l_{ij} = \frac{h^2}{k}[\Pi * p]_{ij}, \tag{3.13}$$

where Π is called *discriminant matrix* and used to sum the stress within the contact region of *n*-th pillar A_n. It is noted that we replace the sum operation with matrix *convolution*, since p is a matrix in discrete form. Thus, the deflection of the *n*-the pillar Δl_n corresponds to elements of the matrix on the right side of Eq. (3.13). The element of the matrix Π is either one or zero.

Let us discuss the size and element arrangement of a squared matrix Π. For convenience we denote $L_{n\xi}$ and $L_{n\eta}$ as the greatest size of n-th pillar's contact region A_n in both directions, and a square or a circle with a least dimension $2r_\Pi$ as the size of the matrix Π (following a squared shape is to be used as shown in Figure 3-3). The nature of convolution requires the condition: $r_\Pi \geq \max(L_{n\xi}, L_{n\eta})$. As for Π, elements inside the square all have a value of **1**, and outside **0**. This ensures that the elements of the convolution $[\Pi * p]_{ij}$ within A_n, their values keep as $\sum_{A_n} p_{ij}$ identical.

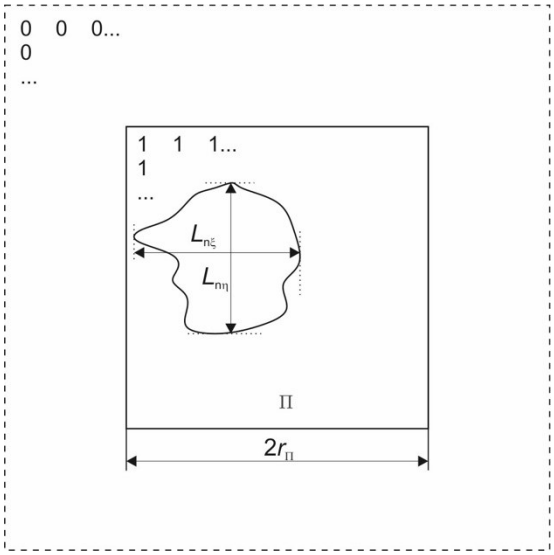

Figure 3-3 A schematic illustration of the discriminant matrix Π. The size of the matrix Π should meet the geometrical condition: $r_\Pi \geq \max(L_\xi, L_\eta)$, where the elements are set one.

For a brush-structure, the length of Π must be larger than the doubled maximal value $L_{n\xi}, L_{n\eta}$ that

$$r_\Pi \geq \max\left(L_{1\xi}, L_{1\eta}, L_{2\xi}, L_{2\eta}, \dots\right). \tag{3.14}$$

The size of matrix Π should also be smaller than the minimal gap g_n among pillars

$$r_\Pi \leq \min(g_1, g_2, \dots), \tag{3.15}$$

which guarantees that the matrix Π must only include the whole contact are that only belongs to one single pillar as shown in Figure 3-4.

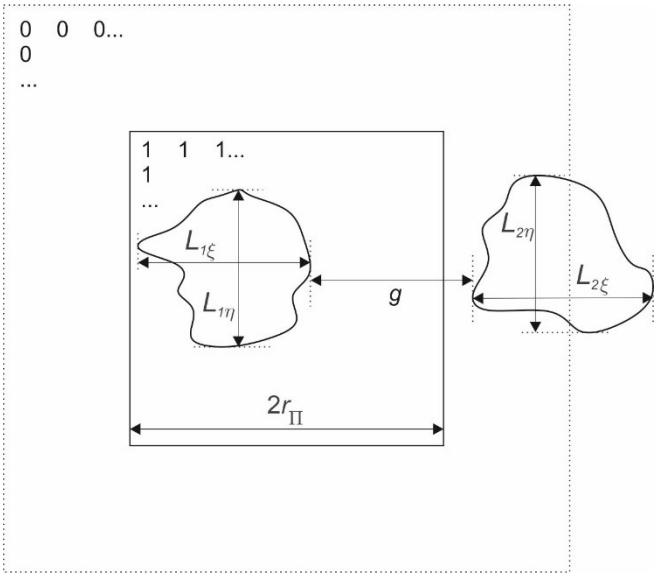

Figure 3-4 A schematic illustration of the discriminant matrix Π in the brush-structures. Similarly, the size of the check zone needs to satisfy the condition that $r_{\Pi} \geq \max(L_{1\xi}, L_{1\eta}, L_{2\xi}, L_{2\eta}, \dots)$, and furthermore, it must satisfy the condition $r_{\Pi} \leq \min(g_1, g_2, \dots)$ as well, where g_i represents the gap between two pillars, which ensures that, the discriminant matrix will not include two pillars' contact zones simultaneously.

So far, we can apply Eq. (3.13) to the whole contact zone

$$d_{ij} = \left[\frac{h^2}{k}\Pi * p\right]_{ij} + [K * p]_{ij}. \tag{3.16}$$

In fact, Eq. (3.16) is applied to the whole simulation domain, since we only interested in the displacement and stress of elements inside the contact zone, to correct the deflection of pillars and the elastic half-space (the displacement of elements outside the contact zone can be determined by applying Eq. (3.6)). To conduct the FFT, the size of Π will be expanded into the same dimension as the matrix of influence coefficient K and stress p, and additional elements are filled with zero. Then the relation Eq. (3.16) can be rewritten in convolution form

$$d = \left(\frac{h^2}{k}\Pi + K\right) * p. \tag{3.17a}$$

Similar to Eq. (3.7), the operation of FFT can be carried out

$$d = \mathrm{IFFT}\left[\mathrm{FFT}\left(\frac{h^2}{k}\Pi + K\right) \cdot \mathrm{FFT}(p)\right]. \tag{3.17b}$$

Therefore, one only has to add a term $\frac{h^2}{k}\Pi$ to the matrix of influence coefficient. In simulation, we assume the displacement of the brush-structure d is given (this means that

we consider the displacement-controlled indentation). The stress p on the elastic half-space can be inversely obtained from Eq. (3.17) by the CG method as in the case of rigid indenters [107]. With this stress p, the displacement of elastic half-space u as well as that of pillars can be determined simply by $\Delta l = d - u$. In this method, the influence of elasticity of the brush-structure is already integrated into the influence matrix, therefore, it can dramatically reduce computation time and there is no further convergence problem.

Notes: Here, an important point needs to be emphasized, during the calculation of p using Eq. (3.17), the calculation results after the convolution $[\frac{h^2}{k}\Pi * p]$ could be non-zero for those elements outside the contact zone, but they will be ignored and set as 0 (As mentioned above, their displacement can be determined by applying Eq. (3.6)). In this situation (to firstly find the correct stress distribution), only values within the contact zone matters, and that is the reason we can apply Eq. (3.17) to the whole simulation domain.

3.3 Numerical results

With two examples, we compare the results from two methods. As discussed previously, this contact can be also solved by the nested-loop method through correcting the position of pillars iteratively (in Section 2.2). The other one is the newly developed convolution method. Figure 3-5 shows the cross-section of displacement of the elastic half-space in the simulation of indentation test of three different elastically embedded indenters: (a) a single flat punch, (b) a single spherical indenter, and (c) 5×5 array multi-pillar structure.

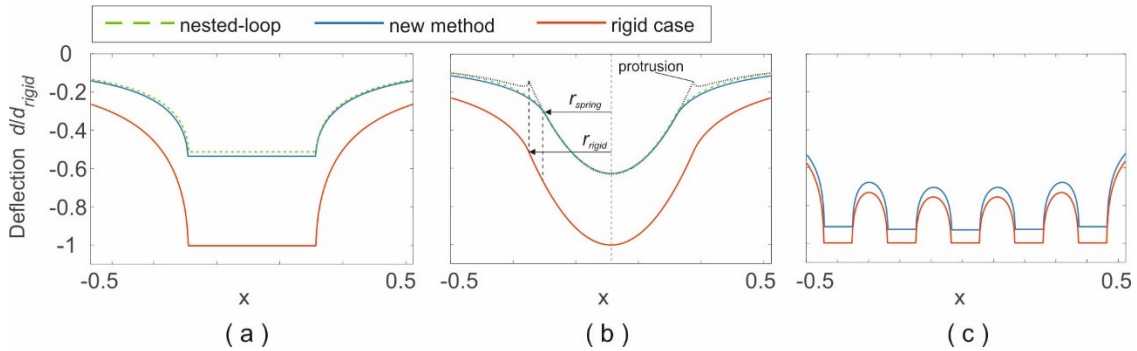

Figure 3-5 Cross-section of deformed elastic half-space indented by (a) a flat cylindrical punch; (b) a sphere indenter; (c) a 5×5 array multi-pillar structure. Contact profiles in green and blue involve elastic embedded model with stiffness $k = 50\ N/\mathrm{mm}$ and the elastic modulus of the elastic half-space is $E = 100\ N/\mathrm{mm}^2$. The simulation domain is $1\ \mathrm{mm} \times 1\ \mathrm{mm}$. The green dashed line is the result based on a nested-loop algorithm to iteratively find the balanced position, and the blue line is the result based on the new algorithm as described above, while the red line is the result of corresponding rigid cases.

The red curves show the cases of rigid indenters, and the blue curves are the results of the convolution method, while the green dashed curves correspond to those of the nested-loop method. The stiffness is $k = 50\ N/\text{mm}$. The elastic modulus of the elastic half-space is $E = 100$ MPa. The simulation domain is $1\ \text{mm} \times 1\ \text{mm}$. From Figure 3-5 (a), one can see that the results from both methods are quite close. It is noted that the iteration in the nested-loop method will stop until a previously given precision is reached, so its solution is not as exact as the convolution method. In Figure 3-5 (b), similar results of a spherical indenter are shown for the two methods. It is noted that the nested-loop method is carried out with the assumption that the contact region keeps the same as the rigid case. Thus, we have to determine the correct contact region over again by every iteration for different indentation depths. Otherwise, a wrong profile can be generated as shown in a dotted black curve. However, as for the convolution method, the correct initial contact region is implicitly satisfied by stress balance, and thus the correct displacement is directly attained. For the multi-spring model, it is difficult to find the balance position of pillars, even for the limited numbers 5×5 in Figure 3-5 (c). In the convolution method, the influence of elastically embedded pillars is already integrated into the kernel matrix. Therefore, it can dramatically reduce computation time. In Figure 3-6, we plot the simulation procedure of the two methods.

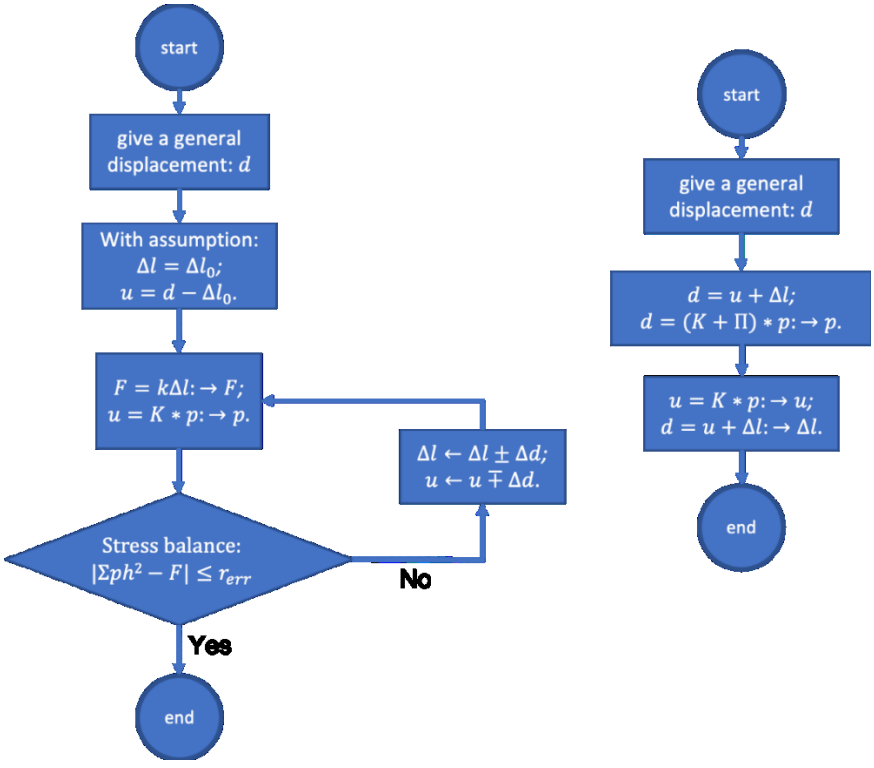

Figure 3-6 Flow chart of the two methods. Left: the nested-loop method; right: the convolution method.

3.4 Combination with adhesion

In the above description, adhesion is not mentioned. In the studied model, adhesion occurs at the interface of pillars and the elastic half-space. Thus, the algorithm of adhesive BEM for rigid indenters suggested in [103], which has been discussed in last chapter (Section 2.2), is still valid for the current case. We apply the stress-criterion to determine the detachment of contacting elements. In the simulation of displacement-controlled pull-off, we initially keep the contacting area constant equaling the total surface area of pillars when an incremental displacement is given. Then the stress distribution can be obtained according to Eq. (3.17). By comparing this tensile stress with the critical value of stress Σ_c (in Chapter 2 Eq. (2.14)), the detachment of elements can be determined, and a new contact area is generated. With this new contact area, the above iteration is repeated until both pressure and geometry conditions for all elements within the contact area are met.

3.5 Conclusions

In this chapter, we successfully developed an effective BEM for the contact simulation of elastic brush-structure. The pillar stiffness is directly integrated into the influence matrix of the BEM. The FFT technique and the conjugate-gradient method as well as the stress criterion for adhesion, which were used in the previous BEM version, are still applicable in the newly developed BEM. Therefore, this new BEM enables faster simulation and higher accuracy compared with the nested-loop method. This new method will be applied in the cases of flat and rough brush-structures, hierarchical structure (with a once again developed BEM) as well as the structure with concave geometry in the following chapters.

Chapter 4 Simulation of adhesive contact of elastic flat brush-structure

With the newly developed BEM, the adhesive contact between a *flat* brush-structure (pillars' length is identical) and an elastic half-space, is numerically studied in this chapter. The influence of pillar stiffness, pillar number and filling factor on the strength of adhesion is investigated.

Part of the work in this chapter appears in paper: He, X.; Li, Q.; Popov, V. L. Simulation of Adhesive Contact of Soft Microfibrils. Lubricants, 2020, 8, 94. doi.org/10.3390/lubricants8100094. My contribution (in accordance with the content of this chapter) is the following:). Li Q and He X contributed to theoretical prediction to two limiting cases including Figure 4-2 and equations Eq. (4.5) to Eq. (4.10) (section 4.2). He X carried out the numerical simulation: this part is described in section 4.3 including Figure 4-3 to Figure 4-7. Popov VL, Li Q and He X discussed the results (section 4.3) and gave an analytical support in Eq. (4.14) to Eq. (4.18). All the authors contributed in preparing the manuscript. All authors reviewed the manuscript.

4.1 Adhesion enhancement of discontinuous surfaces

In the recent twenty years, the contact splitting theory has been a popular topic. It suggests that stronger adhesion can be achieved by dividing the contact surface into small sub-contacts [114]. This concept was initially inspired by the observation of biological adhesive pads of insects and geckos. The strong bio-adhesion is largely attributed to the micropad contact, often in the form of fibrillar structure [115]. There is a lot of theoretical work on the principle of contact splitting, for example the JKR-type approach that the compact indenter is divided into a large number of smaller pillars with small cap radius [115][116]. In the JKR theory, the adhesive force of a spherical cap with radius R_1, is equal to $F_{JKR} = \frac{3}{2}\pi R_1 \Delta\gamma$ [42], where $\Delta\gamma$ is the surface energy per unit area. If we divide the large sphere into N pillars with spherical tips, and the tip radius R_2 is given by

$$R_2 = \frac{R_1}{\sqrt{N}}, \tag{4.1}$$

which keeps the real contact area unchanged as illustrated in Figure 4-1. Under the assumption that the small pillars work independently, so the total adhesive force following the JKR solution reads [115]

$$F_{R_2} = N\frac{3}{2}\pi R_2 \Delta\gamma = \sqrt{N}\frac{3}{2}\pi R_1 \Delta\gamma. \tag{4.2}$$

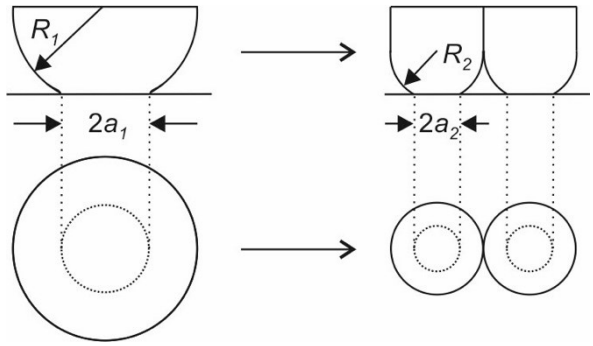

Figure 4-1 A schematic illustration of the concept of contact splitting. The original spherical indenter is divided into two smaller pillars with spherical tips, but the real contact area keeps unchanged.

According to Eq. (4.2), the splitting enhances the adhesive strength by $\sqrt{N}$, considering the precondition that the entire real contact area of fine sub-contacts is equivalent to the original compact contact area. The adhesive force increases with the number of divided pillars.

Furthermore, Gao and Yao have investigated the critical size of pillars, and suggested that a pillar with very small contact size approaches uniform stress distribution at the complete separation moment [117]. Through size reduction of pillars, an upper-limiting adhesive force could be achieved. For the structure with pillar number N_c and very small tip radius ($R_c \ll R_1$), i.e. $R_c = R_1/\sqrt{N_c}$, the adhesive force in the case of uniform stress distribution with adhesive stress p_c, can be expressed as

$$F_{R_c} = N_c \pi R_c^2 p_c = \pi R_1^2 p_c. \tag{4.3}$$

The ratio of this critical force to the JKR solution reads [117]

$$\frac{F_{R_c}}{F_{JKR}} = \frac{2R_1 p_c}{3\Delta\gamma}. \tag{4.4}$$

For instance, $\Delta\gamma = 1\ \mathrm{mJ/m^2}$, $p_c = 1$ MPa, then the amplification of enhancement in order of magnitude reaches 10^6 for $R_1 = 1$ mm, and 10^3 for $R_1 = 1$ μm.

Experimental studies found that the adhesive strength of a surface with fibrillar structure can be greater than it of compact one [27][118]-[120]. In the experiment of [118], over twice larger adhesive force was observed in adhesive contact between a micropillar-patterned PDMS surface and glass substrates, compared with that of unpatterned surfaces.

This enhancement can be attained even for rough substrates. The detailed review can be found in ref. [115][121][122].

Recently, adhesive contact between a rigid brush-structure and an elastic half-space has been numerically simulated using the BEM [75][76]. For the flat rigid brush-structure, it has been found that the adhesive force is roughly proportional to the square root of real contact area, meaning that adhesion was not enhanced [75]. However, in these studies [75][76][79], the pillars are rigid, which does not conform to the true cases of insects' or gecko's feet. The elasticity of brush-structure may play an important role in adhesion and the contact splitting theory.

4.2 Analytical solutions for limiting cases

We consider a brush-structure with a large number of elastically embedded pillars as illustrated in Figure 1-4. We analyze a brush-structure with a large number of elastically embedded pillars. Firstly, we consider a limiting case where the stiffness k is infinitely large. In the adhesive contact between such a flat rigid brush-structure with the apparent area A_0 and an elastic half-space with elastic modulus E and Poisson's ration ν, the adhesive force has been given in [74]

$$F_R \approx \sqrt{8\pi E^* \Delta\gamma \varphi \left(\sqrt{A_0/\pi}\right)^3}, \tag{4.5}$$

where $E^* = E/(1-\nu^2)$ is the effective elastic modulus, and φ is the filling factor defined as the ratio of the real contact area A to the apparent area A_0, $\varphi = A/A_0$ (thus, $\varphi < 1$). This solution has the same form as the Kendall's solution of a single flat punch in adhesive contact [108], but with an effective surface energy changed by a factor φ. Rewriting Eq. (4.5) and substituting the apparent area with the real contact area, then it gives

$$F_R \approx \varphi^{-\frac{1}{4}} \cdot \sqrt{8\pi E^* \Delta\gamma \left(\sqrt{A/\pi}\right)^3}. \tag{4.6}$$

The term $\sqrt{8\pi E^* \Delta\gamma \left(\sqrt{A/\pi}\right)^3}$ in Eq. (4.6) is the Kendall's solution to adhesive force for a compact cylindrical punch with radius $\sqrt{A/\pi}$. Observing Eq. (4.6), we conclude that if a compact flat cylinder is split into a sparse structure with a larger apparent area, then the adhesive force will be increased by a factor $\varphi^{-\frac{1}{4}}$, as illustrated in Figure 4-2. For example, the amplification is $\varphi^{-\frac{1}{4}} = 1.19$ for $\varphi = 0.5$ and $\varphi^{-\frac{1}{4}} = 1.78$ for $\varphi = 0.1$, which shows limited enhancement of adhesion.

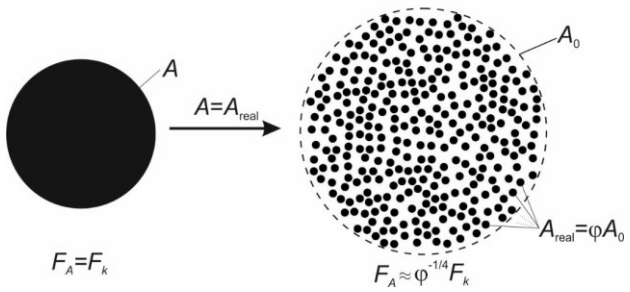

Figure 4-2 A rigid flat cylinder is split into a sparse brush-structure with the same real contact area A but larger apparent area A_0, i.e. $A = \varphi A_0$. The adhesive force is increased by a factor $\varphi^{-\frac{1}{4}}$ in the rigid case.

Another limiting case corresponds to the very soft pillars. If the contact stiffness of the elastic half-space is much larger than the pillar stiffness in the brush-structure, the pillars will detach individually from the half-space. We assume that the pillars have the same geometry. Then the adhesive force for such a flat soft brush-structure is simply the sum of individual forces

$$F_S = NF_a = N \cdot \sqrt{8\pi E^* \Delta\gamma a^3}, \tag{4.7}$$

where N is the number of pillars, a is the radius of pillars. Considering the same contact as shown in Figure 4-2, we get $N \cdot A_{pillar} = A$, then Eq. (4.7) can be rewritten as

$$F_S \approx N^{\frac{1}{4}} \cdot \sqrt{8\pi E^* \Delta\gamma \left(\sqrt{A/\pi}\right)^3}. \tag{4.8}$$

From Eq. (4.8), we conclude that in this limiting case the adhesive force will be increased by the factor $N^{\frac{1}{4}}$. This result is quite similar to the theory of contact splitting, where an enhanced adhesive force is obtained by a factor $\sqrt{N}$ as described in Section 4.1. The amplification is then $N^{\frac{1}{4}} = 2.24$ for $N = 25$ and $N^{\frac{1}{4}} = 4.47$ for $N = 400$, which shows that however, a strong enhancement of adhesion.

According to Eq. (4.8), the adhesive force seems to increase unlimitedly with an increase of pillar number. However, in any real system, the adhesive stress is finite and determines the 'theoretical strength' of adhesive contact. The strength cannot exceed this limit. From the point of view of the theory of adhesion, this limitation corresponds to the transition from the JKR-type of adhesion to the DMT kind.

Normalized by the Kendall's solution to the case of a compact cylindrical punch with radius $\sqrt{A/\pi}$ that $F_K = \sqrt{8\pi E^* \Delta\gamma \left(\sqrt{A/\pi}\right)^3}$, the estimations Eq. (4.6) and Eq. (4.8) for the rigid and very soft cases can be expressed as

$$\tilde{F}_R = \frac{F_R}{F_K} = \varphi^{-\frac{1}{4}}, \tag{4.9}$$

$$\tilde{F}_S = \frac{F_S}{F_K} = N^{\frac{1}{4}}. \tag{4.10}$$

Comparing the two cases, however, the main difference between these two results is that, the influence from *elastic interaction among pillars*, as well as the effect of *stress concentration* at the outer edge of the apparent area. The contact-splitting model emphasizes that every single pillar is independent of each other, so the state of separation for any single pillar is identical. While the rigid-brush model considers that the interactions among rigid pillars are coupled through the contact with the elastic foundation. In the case of arbitrary pillar stiffness, an analytic solution is not possible, and the BEM described in Chapter 3 is used for simulation of adhesive contact of elastic flat brush-structures.

4.3 Results and discussion

We carry out the numerical simulation of adhesive contact between a flat brush-structure and an elastic half-space, and investigate the influence of pillar stiffness and number of pillars. The pillars have the same radius and are regularly or randomly distributed in a square area $L \times L = 1\ \text{mm} \times 1\ \text{mm}$. The system is discretized with 512×512 elements. The filling factor is almost constant for all cases $\varphi \approx 0.12$. The pillar stiffness k, and the pillar number N will vary.

The following normalizations are used in the whole analysis: forces are normalized by the Kendall's solution to a compact cylindrical punch with the same real contact area A, so that we can clearly observe the effect of splitting. Displacement is normalized by the critical displacement of a rigid flat brush-structure as suggested in [75]

$$\tilde{F} = \frac{F}{\sqrt{8\pi E^* \Delta\gamma \left(\sqrt{A/\pi}\right)^3}}, \tag{4.11}$$

$$\tilde{d} = \frac{d}{\sqrt{\frac{2\pi\varphi\Delta\gamma\sqrt{A_0/\pi}}{E^*}}}. \tag{4.12}$$

The pillar stiffness is normalized as follows

$$\tilde{k} = \frac{k}{E^* L}. \tag{4.13}$$

Here E^*L is roughly the contact stiffness of the macroscopic brush-structure in contact with the elastic half-space. So the dimensionless stiffness indicates the elasticity of the brush-structure in comparison with the contact property.

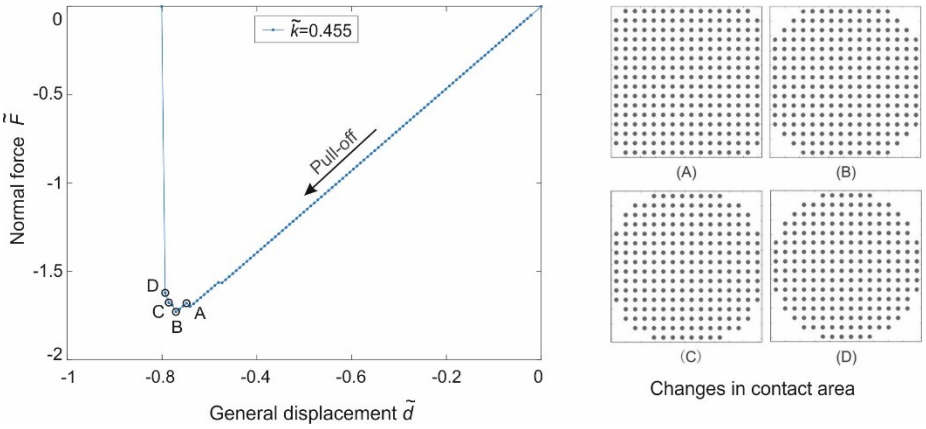

(a)

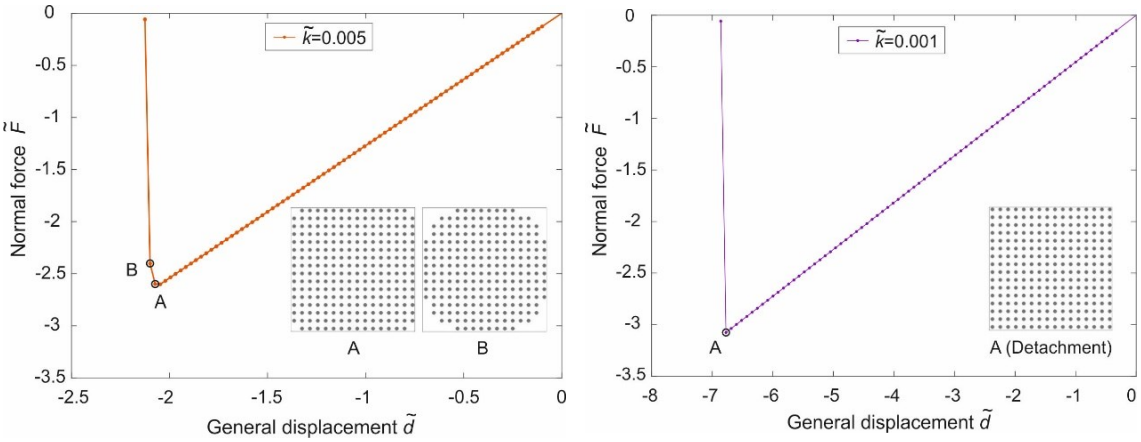

(b) (c)

Figure 4-3 Dependence of the normal force on the displacement of brush-structure in the simulation of pull-off process with different stiffnesses: (a) $\tilde{k} = 0.455$; (b) $\tilde{k} = 0.005$; (c) $\tilde{k} = 0.001$. The subfigures show the change in the contact area at a few marked stages of pull-off.

Figure 4-3 shows the simulation examples of pull-off process of a brush-structure with 16×16 pillars. Dependence of the normal force $\tilde{F}$ on the general displacement $\tilde{d}$, is shown for three values of stiffness $\tilde{k}$. In the case of large stiffness $\tilde{k} = 0.455$, the load-displacement curve and the detachment process are similar to that of the rigid pillars as described in [74][75] (Figure 4-3 (a)). Separation initially occurs at the sharp corners of the contact zone and it propagates inwards till to a circle-like shape, then all remained pillars detach completely. The maximum pull-off force (in tensile state), which is identified as adhesive force $\tilde{F}_A$, is about 1.8, which indicates that the adhesive force is 1.8 times larger

than it in the case of a compact cylindrical punch with the same *real* contact area. This value is very close to the limiting case of rigid pillars, $\tilde{F}_R = \varphi^{-1/4} = 1.7$, according to Eq. (4.9).

When the pillars become soft (small stiffness), e.g. $\tilde{k} = 0.005$ as shown in Figure 4-3 (b), the complete detachment occurs earlier when the contact area is still not the circle-like shape yet. In the case of very small stiffness $\tilde{k} = 0.001$ as shown in Figure 4-3 (c), the normal force increases almost linearly until the moment when all the pillars detach instantly.

Dependences of the adhesive force $\tilde{F}_A$ on the stiffness $\tilde{k}$ for different numbers of pillars are shown in Figure 4-4. Figure 4-4 (a) shows the case of regularly distributed pillars with number of 8×8 (64), 16×16 (256), 24×24 (576) and 48×48 (2304), while Figure 4-4 (b) shows the case of random distribution with 64, 220, 425 and 1620 pillars.

With large stiffness (in the range of $\tilde{k} > 1$), the adhesive forces for both cases and numbers of pillars are almost the same, and very slightly larger than the value of theoretical approximation from Eq. (4.9) (solid lines in the bottom right of figures). The results are similar to those of the rigid case reported in [75]. Decreasing the stiffness leads to an increasing adhesive force until it reaches a plateau. For soft pillars, the pillar number plays an important role in the adhesive force. Therefore, one can see that the adhesive force is strongly enhanced if the punch is split into fine pillars, especially when the pillar stiffness is small. For example, the adhesive force increases by the factor of *six* times for the case with 2304 pillars.

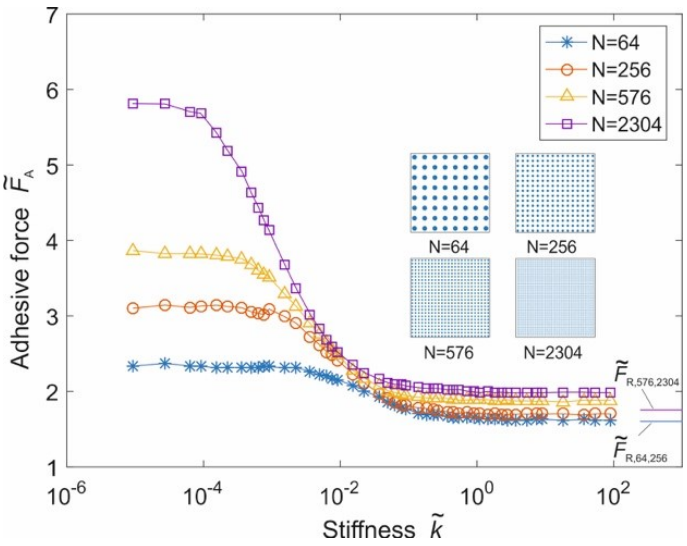

(a)

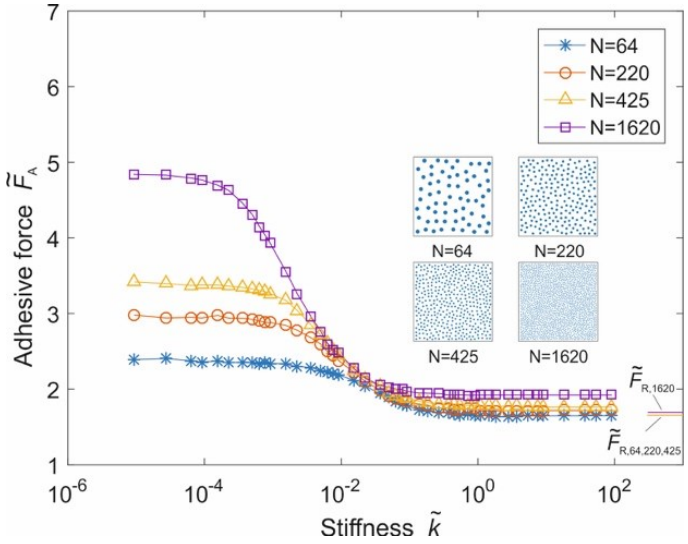

(b)

Figure 4-4 Dependence of the adhesive force on the stiffness for different numbers of pillars (a) regularly and (b) randomly distributed in a square area. The theoretical approximations for the case of rigid structure are given in the bottom right of figures.

It is also found that for the case with larger pillars number, the stiffness needed for reaching the plateau of the soft region (the maximum enhancement) is smaller, i.e. the largest enhancement appears earlier for cases with fewer pillars. For example here, it is $\tilde{k} = 10^{-3}$ for pillar number 64, but $\tilde{k} = 10^{-5}$ for pillar number 2304.

Focusing on the plateau region with very small stiffness in Figure 4-4 (i.e. the largest enhancement cases), we compare the adhesive force in this region with the theoretical prediction $\tilde{F}_S = N^{\frac{1}{4}}$ as in Eq. (4.10). The curves are presented in a double logarithmic plot in Figure 4-5. The numerical results have the same power-law with a power of 1/4 as the theoretical prediction, but the amplitude coefficient is about 1.2 to 1.3 times smaller than the values in the analytical estimation.

When we vary the filling factor φ, the better effect of approaching the contact splitting theory is obtained when the filling factor becomes smaller, as shown in Figure 4-6. It is noted that the dimensionless forces $\tilde{F}_A$ for different filling factors are not comparable, since they are normalized by different values (with different contact area (i.e. filling facor), see Eq. (4.11)). Thus, the forces $\tilde{F}_A$ indicates the level of approaching contact splitting.

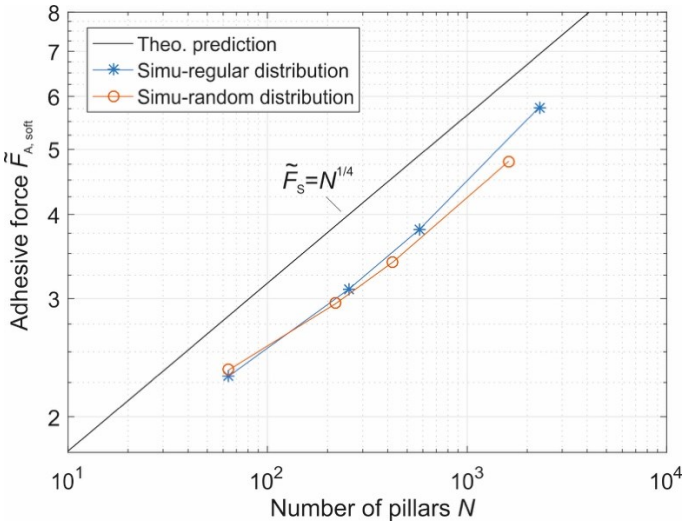

Figure 4-5 Comparison of the adhesive forces at the plateau region: solid line is the theoretical prediction in Eq. (4.10) and symbols are numerical results.

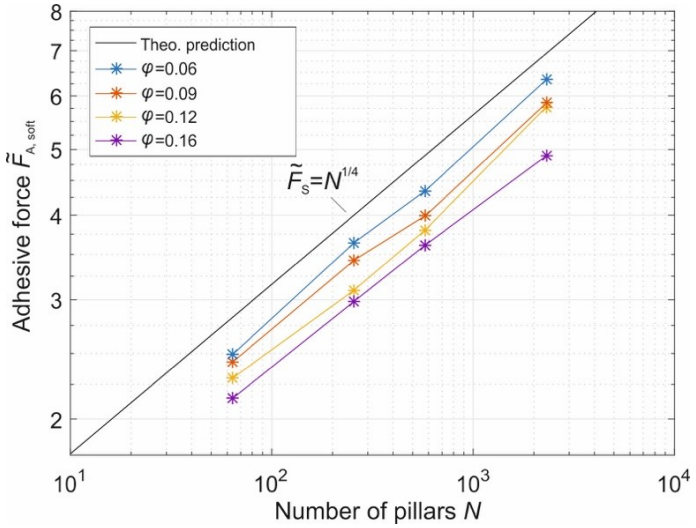

Figure 4-6 The dimensionless adhesive force at the plateau region for different filling factors.

We discuss the work of separation briefly, which is simply obtained from the load-displacement curve from the zero-indentation to the complete separation. It is known that in the case of a rigid cylindrical punch with radius a_0, the work of separation is equal to [74]

$$W_K = 2\pi\Delta\gamma a_0^2. \tag{4.14}$$

Half of this energy will be used to create new surfaces and the other half will dissipate in the elastic foundation. In the following discussion, the work of separation is normalized by the value of Eq. (4.14),

$$\widetilde{W} = W/W_k. \tag{4.15}$$

In Figure 4-7, the work of separation for different stiffnesses and pillar numbers is presented. It can be found that for large stiffness, the work of separation is roughly equal to the case of rigid compact punch. With the reduction of stiffness, the work of separation increases, since the energy stored in the brush-structure becomes important. Furthermore, the work of separation decreases with the number N.

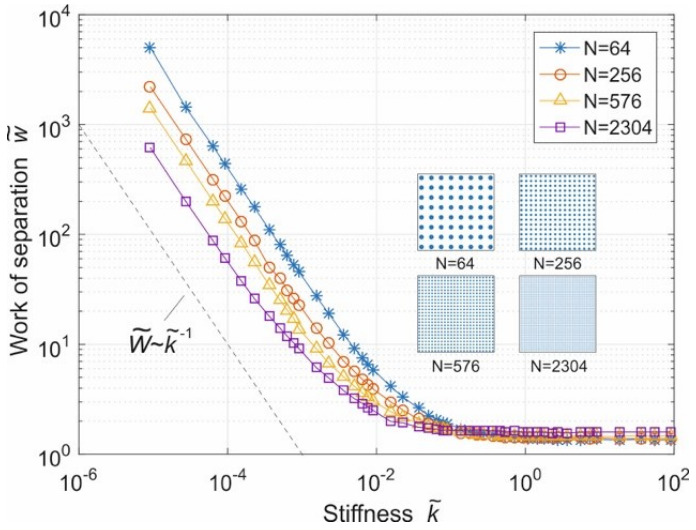

(a)

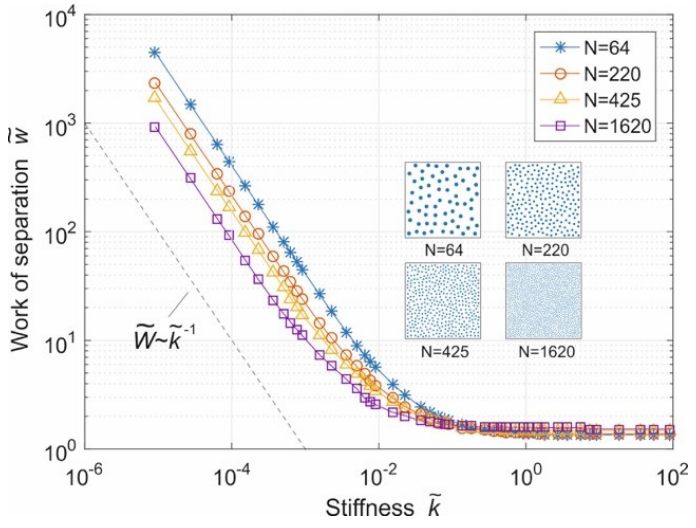

(b)

Figure 4-7 Dependence of the work of separation on the stiffness for different numbers of pillars (a) regularly and (b) randomly distributed in a square.

If the stiffness is very small, the energy will be stored mainly in the brush-structure. In this case, the force on each pillar can be calculated from Eq. (4.8)

$$f \approx \frac{F_S}{N} = N^{-\frac{3}{4}} \cdot F_K. \tag{4.16}$$

Thus, the elastic energy stored in the brush-structure with pillar stiffness k is roughly

$$W_S \approx N\frac{F_a^2}{2k} = N^{-\frac{1}{2}} \cdot \frac{F_K^2}{2k}. \tag{4.17}$$

where $F_a = \sqrt{8\pi E^* \Delta\gamma a^3}$ is the individual adhesive force for a single pillar. In dimensionless form, it can be written as

$$\widetilde{W}_S \approx N^{-\frac{1}{2}} \cdot \frac{2E^* a_0}{k} = N^{-\frac{1}{2}} \cdot \varphi^{\frac{1}{2}} \cdot \frac{1}{\tilde{k}}\,. \tag{4.18}$$

Following Eq. (4.18), the work of separation $\widetilde{W}_S$ is inversely proportional to the stiffness $\tilde{k}$, and decreases with the number of pillars N. This approximation coincides with the result for very small stiffness as shown in Figure 4-7.

4.4 Conclusions

In this chapter, we numerically studied the adhesive behavior of elastic flat brush-structure with the help of the developed BEM. The present elastic brush-structure aims to bridge the limiting cases of very rigid pillars and extremely soft pillars (which approaches the contact splitting) [73][115][121]. The influence of pillar stiffness, number of pillars and filling factor, was investigated. The transition from rigid brush-structure to very soft pillars was obtained. It is found that the adhesive force can be enhanced by splitting a compact punch into micro pillars. This effect becomes strong when the pillar number is large and the pillar stiffness is small. The enhancement is roughly a power function of pillar number with the exponent $1/4$, in the case of very small pillar stiffness.

Contact splitting alone does not increase the adhesive strength greatly. When we consider the adhesion of a compact surface with the same *apparent* contact area, and if the 'splitted spots' are connected rigidly with each other, this always leads to a decrease of the adhesive strength (since the real contact area actually decreases). However, if the pillars possess elasticity, the adhesive strength can increase or decrease, depending on the number and elasticity of the pillars.

Chapter 5 Adhesive contact of rough brush-structure

Adhesive contact of rough fibrillar structure has been intensively investigated in the last few decades [123]-[125]. For instance, Hui et al. proposed an array structure with linear springs, and the length of fibrils was ruled by Gaussian distribution [69][70]. It was found that increasing the compliance of fibrils can weaken the detrimental effect of roughness. Based on theoretical studies, technologies for fabrication of structured surfaces mimicking the function of gecko's foot pad have been developed. Micropillar-patterned PDMS surfaces have shown stronger adhesion compared with unpatterned surfaces [118]. It was shown that elastic fibrils could possess better adaptability to comply with surfaces, even with rough surfaces [125].

In this chapter, we consider the adhesive contact of rough elastic brush-structure on an elastic half-space. The pillar's length distribution is ruled by the Gaussian distribution. The elastic coupling of fibrils is treated numerically exactly, without any further simplifications. The developed BEM is used for numerical simulation, to investigate the influence of pillar stiffness and roughness.

Part of the work in this chapter appears in paper: He, X.; Li, Q.; Popov, V. L. Strength of adhesive contact between a rough fibrillar structure and an elastic body: Influence of fibrillar stiffness. The Journal of Adhesion, 2021. doi: 10.1080/00218464.2021.1939017. My contribution (in accordance with the content of this chapter) is the following: He X proposed the numerical model and carried out the numerical simulation: this part is described in section 5.1 including Figure 5-1. He X prepared Figure 5-2 to Figure 5-7. Popov VL, Li Q and He X discussed the results (section 5.2) and gave an analytical support in Eq. (5.6) to Eq. (5.8). All authors contributed in preparing the manuscript. All authors reviewed the manuscript.

5.1 Numerical Model

The numerical model is shown in Figure 5-1. The brush-structure is composed of a large number of cylindrical pillars with the same radius. The length of pillars is characterized by the probability density function

$$\Phi(l) = \frac{1}{\sqrt{2\pi\sigma}} \mathrm{e}^{-\frac{(l-l_0)^2}{2\sigma^2}}, \tag{5.1}$$

where l is the length of pillars, σ and l_0 are the standard deviation and the mean value respectively. The parameter σ describes the characteristic roughness of the brush-structure. The pillar stiffness indicates the elastic connection between rigid cylinders and a rigid plate with linear springs, as shown in Figure 5-1. This model is equivalent to a system with a thin elastic layer between cylinders and a rigid plate [106] (Figure 5-1 right).

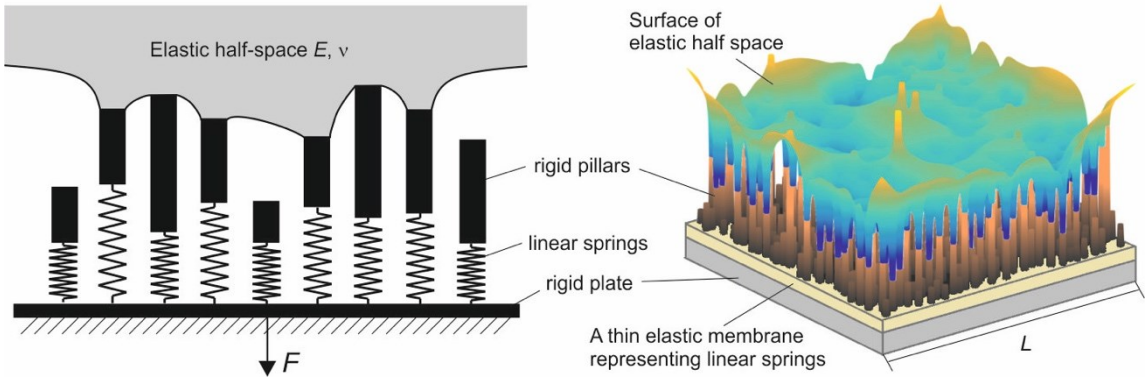

Figure 5-1 Sketch of adhesive contact between a rough brush-structure and an elastic half-space. The right figure shows an equivalent three-dimensional illustration.

We assume that all elastically embedded pillars have the same stiffness k, since the length of pillars is much greater than the characteristic roughness ($l \gg \sigma$). The developed FFT-assisted BEM is used to carry out the pull-off simulation of adhesive contact of elastic brush-structures considering roughness, which is equivalently replaced by the distribution of pillars' length.

5.2 Results and discussion

In simulation, the brush-structure is pressed against the elastic half-space by a general displacement d, and then pulled off until the complete detachment, under the condition of controlled displacement. The results are normalized by the characteristic values of force, the critical indentation in the case of *rigid flat brush-structure* [75]

$$\tilde{F} = \frac{F}{F_c}, \tilde{d} = \frac{d}{d_c}, \tag{5.2}$$

with

$$F_c = \sqrt{8\pi\varphi E^* \Delta\gamma \left(\sqrt{A_0/\pi}\right)^3}, \tag{5.3}$$

$$d_c = \sqrt{\frac{2\pi\varphi\Delta\gamma\left(\sqrt{A_0/\pi}\right)}{E^*}}, \tag{5.4}$$

where φ is the filling factor defined as the ratio of the area of all pillars' cross-section A_{cross} to the apparent area A_0, $\varphi = A_{cross}/A_0$, here $\varphi = 0.16$ is determined. E^* is the effective elastic modulus $E^* = E/(1-\nu^2)$, and $\Delta\gamma$ is the surface energy per unit area. F_c is the adhesive force and d_c is the critical displacement for the rigid flat brush-structure.

It is noted that the normalization Eq. (5.3) is different from those in the case of flat brush-structures in Chapter 4, where the Kendall's solution of a compact punch with the same true (real) area was used. Here, we directly use the theoretical estimation of the flat rigid brush-structure, which is roughly proportional to the square root of real contact area as shown in Eq. (4.5) and Eq. (4.6). In comparison with the results of rigid flat brush-structure, we can better understand the influence of pillar stiffness and roughness on adhesion.

The characteristic roughness σ and pillar stiffness k are normalized as

$$\tilde{\sigma} = \frac{\sigma}{d_c}, \tilde{k} = \frac{k}{E^* L}, \tag{5.5}$$

where L is the size of simulation area, so the apparent area $A_0 = L \times L$. The value $E^* L$ is roughly the contact stiffness of a rigid punch with diameter L in contact with an elastic half-space.

With an example, we show the value of the dimensionless stiffness using the values of biomaterial: pillars distributed in area $10\ \mu m \times 10\ \mu m$ have elastic modulus 1 GPa, length $2\ \mu m$ and diameter $0.2\ \mu m$, and the half-space has effective elastic modulus $E^* = 1$ GPa. According to the beam theory, the pillar stiffness is $0.02\ N/mm$. Contact stiffness of a rigid flat punch with this elastic half-space is roughly $10\ N/mm$. This case corresponds to the dimensionless stiffness $\tilde{k} = 0.002$. To obtain a general law, the dimensionless stiffness $\tilde{k}$, the roughness $\tilde{\sigma}$, and the maximum displacement $\tilde{d}$ are varied to study their influence on the adhesive strength.

Firstly, we present nine simulations of pull-off process for different roughnesses $\tilde{\sigma}$ ranging from 0.07 to 2.10. Filling factor $\varphi = 0.16$ is used. In all cases, the structure was initially pressed by the general displacement corresponding to the same preload $\tilde{F}_P \approx 6.5$ (i.e. for different stiffness cases, the initial displacement varies, but the preload keeps unchanged). A large stiffness is used $\tilde{k} = 10$. Dependences of the normal force on the displacement and the contact area are shown in Figure 5-2.

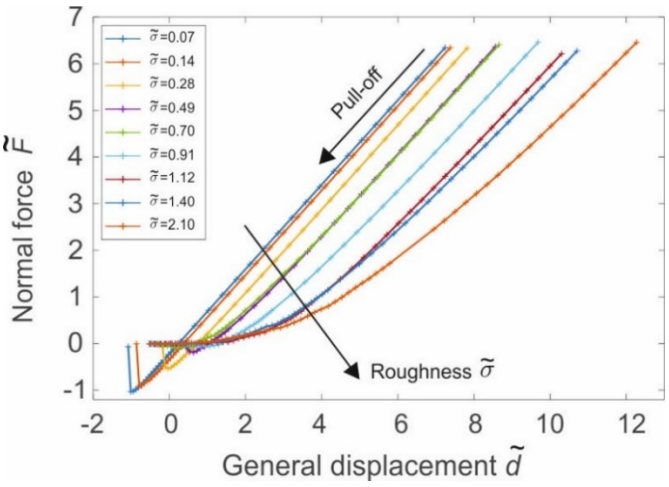

(a)

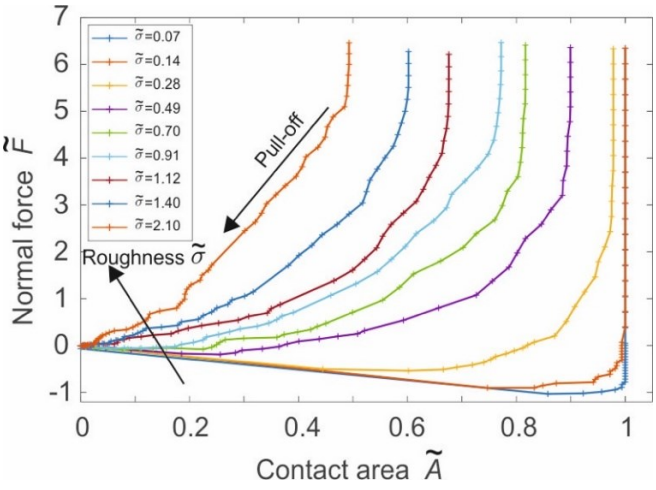

(b)

Figure 5-2 Dependences of the normal force on the displacement (a) and the contact area (b) for different roughnesses. The stiffness is $\tilde{k} = 10$.

At the initial displacement (the maximum), the initial applied force (preload) $\tilde{F}_P$ is recorded. The absolute value of the minimum negative pull-off force is considered as adhesive force $\tilde{F}_A$. It is clearly seen that the adhesive force decreases with roughness. For very rough structures, the adhesive force approaches zero. The fact that roughness reduces the strength of adhesion is well-known (it is generally valid with an exception of a slight enhancement of adhesion for the case of very small level of surface roughness [65][126][127]).

We alter the preload, and this changes the preliminary contact area, then eventually affects the adhesive force. In Figure 5-3, the influence of preload on the adhesive force is shown for different roughnesses. The values are averaged by 10 realizations of rough brush-structures. When roughness is determined, the adhesive force increases with the preload

almost linearly firstly, and ultimately reaches a plateau where the adhesive force is independent of the preload. This behavior can be observed for all cases of different roughnesses. For very small roughness e.g. $\tilde{\sigma} = 0.070$ (blue curve in Figure 5-3), the structure is almost flat, so that the value of normalized adhesive force approaches one, which corresponds to the rigid case.

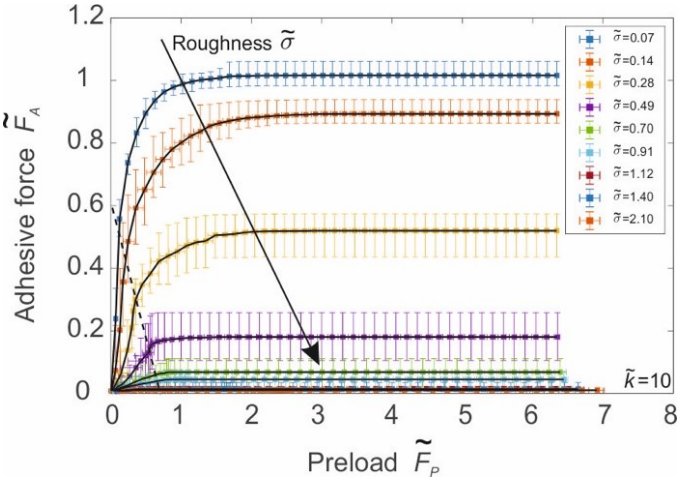

Figure 5-3 Dependence of the adhesive force on the preload. The stiffness is $\tilde{k} = 10$.

With the same parameters as above, the simulations were repeated for different stiffnesses $\tilde{k}$ ranging from 10 to 0.001. The last one corresponds to the very soft case. Dependences of the adhesive force on the preload and roughness for four selected cases $\tilde{k} = 1, 0.1, 0.01, 0.001$, are shown in Figure 5-4.

With the decrease of stiffness, the influence of roughness becomes weak, thus the adhesive force becomes tolerant to roughness. The case of $\tilde{k} = 1.0$ (Figure 5-4 (a)) corresponds to a still quite rigid structure, and thus, the dependence is nearly the same as it in the case $\tilde{k} = 10$.

It is found that the enhancement of adhesive strength is achieved when the stiffness is small (soft pillars), which is even sufficient for cases of large roughness. For example, in the case of a quite flat and rigid structure ($\tilde{k} = 1.0$ and the smallest roughness $\tilde{\sigma} = 0.07$, the blue curve in Figure 5-4 (a)), the maximum adhesive force $\tilde{F}_A$ lies at 1. While it approaches 2, when the pillars are very soft $\tilde{k} = 0.001$ (Figure 5-4 (d)). For cases of the largest roughness $\tilde{\sigma} = 2.1$, the adhesive force almost vanishes for the case of $\tilde{k} = 1.0$, but it still remains at a high level of $\tilde{F}_A = 1.5$ for the soft case of $\tilde{k} = 0.001$.

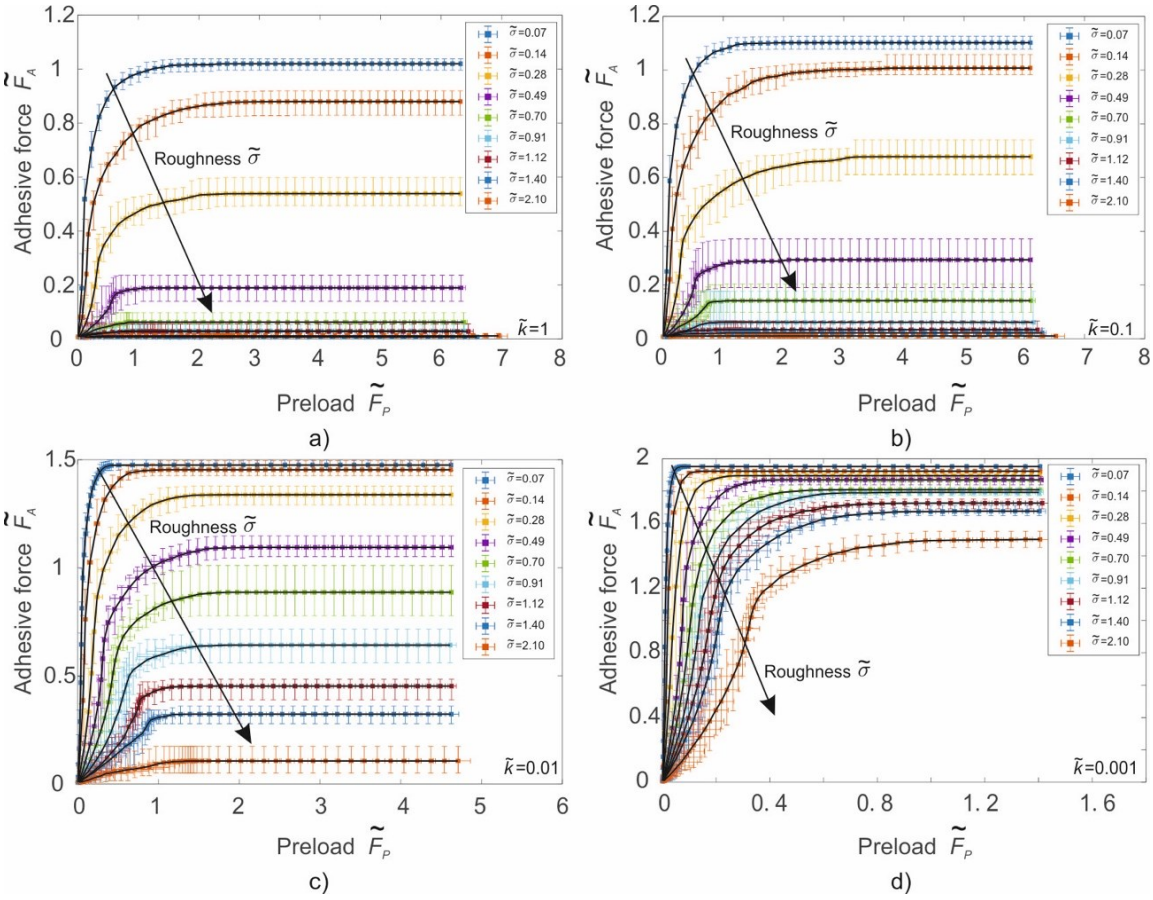

Figure 5-4 Dependences of the adhesive force on the preload for different roughnesses with stiffness (a) $\tilde{k} = 1.0$; (b) $\tilde{k} = 0.1$; (c) $\tilde{k} = 0.01$; (d) $\tilde{k} = 0.001$.

It is noted that the ranges of x coordinate in four figures of Figure 5-4 are different. The linear region will be shorter when reducing the stiffness. Softer structure reaches the plateau region earlier compared with stiffer one.

Let us look in more detail at the dependence of the adhesive force on the preload. In the linear region, $\tilde{F}_A$ is roughly proportional to $\tilde{F}_P$

$$\tilde{F}_A = c\tilde{F}_P, \tag{5.6}$$

where the slop c is known as adhesion coefficient [109][128]. In Figure 5-5, the dependence of adhesion coefficient on roughness (for stiffness varying between $\tilde{k} = 0.001$ and $\tilde{k} = 10$), is shown with symbols.

The adhesion coefficient c decreases rapidly with roughness, especially for cases of large stiffness. With increasing stiffness, curves approach the result of the rigid case, and they collapse practically to one curve when $\tilde{k} \geq 0.55$. However, for soft structures, e.g. $\tilde{k} =$

0.001, adhesion coefficient can reach $c = 204$ (at the smallest roughness $\tilde{\sigma} = 0.01$), which is more than 25 times larger than $c = 8$ for cases of large stiffness $\tilde{k} \geq 0.55$.

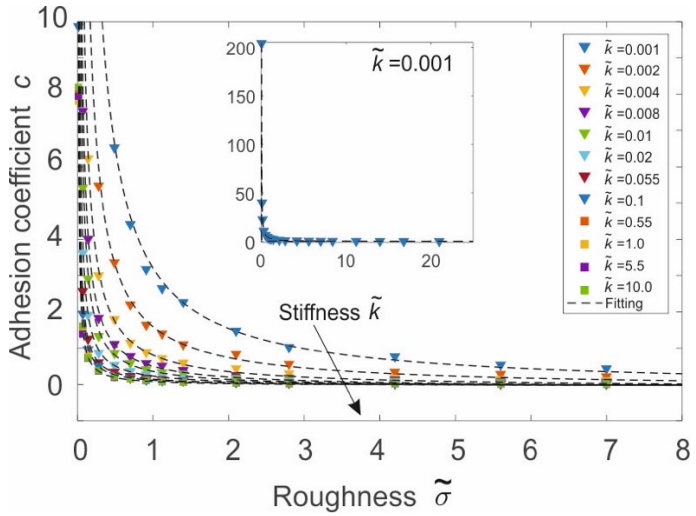

(a)

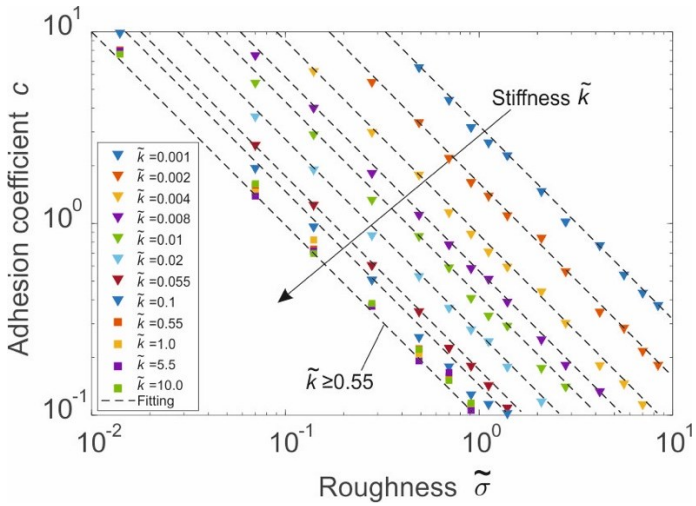

(b)

Figure 5-5 (a) Dependence of adhesion coefficient on the characteristic roughness for different stiffnesses, and (b) this dependence in double logarithmic coordinates.

For a structure with independent elastic pillars [109], where the pillar's length follows an exponential probability distribution, an approximation of such a linear relation was given by $c = \frac{\tilde{F}_A}{\tilde{F}_P} = \frac{1}{\tilde{\sigma}} - 1$, and we can rewrite it as

$$\tilde{F}_A = \left(\frac{1}{\tilde{\sigma}} - 1\right)\tilde{F}_P. \tag{5.7}$$

In this case, adhesion vanishes at $\tilde{\sigma}_c = 1$. While for the case based on the Gaussian distribution, it can be expressed as $c = \frac{\tilde{F}_A}{\tilde{F}_P} = \frac{0.1}{\tilde{\sigma}} - 0.03$, and macroscopically no adhesion is found at $\tilde{\sigma}_c = 3.33$. In this chapter, similarly, we can approximate our numerical results with a similar dependence

$$\tilde{F}_A = c(\tilde{\sigma}, \tilde{k}) \cdot \tilde{F}_P = \left[\alpha(\tilde{k}) \cdot \frac{1}{\tilde{\sigma}} - \beta(\tilde{k})\right] \cdot \tilde{F}_P, \tag{5.8}$$

where α can be interpreted as an amplification factor depending on stiffness, compared with the rigid brush-structure. While β is the bias to determine the maximum roughness, after which adhesion vanishes. Fitting Eq. (5.8) to numerical results is shown by dashed lines in Figure 5-5. It is seen that the function Eq. (5.8) describes the relation well. The values of α, β for different stiffnesses can be found in the Table 1.

When roughness is very large, the adhesive force should vanish. The transition from adhering to non-adhering surfaces is rather sharp, and the critical value of roughness $\tilde{\sigma}_c = \alpha/\beta$, can be identified with good precision. Simulations show that this value strongly depends on the pillar stiffness. For the rigid case, the critical roughness is about 3.67. The values for other soft pillars are listed in Table 1.

Table 1 Values of α, β and $\tilde{\sigma}_c$

$\tilde{k}$	$\geqslant$ 0.55	0.1	0.055	0.02	0.01	0.008	0.004	0.002	0.001
α	0.11	0.15	0.18	0.28	0.44	0.59	0.91	1.7	3.32
β	0.03	0.035	0.035	0.05	0.08	0.09	0.1	0.11	0.15
$\tilde{\sigma}_c$	3.67	4.29	5.14	5.6	5.5	6.56	9.1	15.45	22.13

Now we consider the region of plateau, where the adhesive force is independent of the preload. The dependences of the adhesive force on roughness and stiffness are shown in Figure 5-6. Similar to the linear region, the adhesive forces are approaching the result of the rigid case, as stiffness increases (in Figure 5-6 (a)). When stiffness is larger than 0.55, all curves collapse to one curve. The adhesive force at the plateau decreases with roughness as well as stiffness. A similar relation between the adhesive force and roughness has been numerically and experimentally obtained in other studies [69][129]. But in [69], the interaction among pillars was not considered, so that it was assumed that all pillars separated at the same individual force (but the separation moment of pillars could be different).

We plot the dependence of the adhesive force on the pillar stiffness in Figure 5-6 (b). For the flattest case of $\tilde{\sigma} = 0.01$, the relation between $\tilde{F}_A$ and $\tilde{k}$ resembles the development of that flat-pillars case (as shown in Figure 4-4). When stiffness is small, the difference of adhesive forces for different roughnesses declines, i.e. very soft structure lets roughness' effect reduce, but this influence turns weak with increasing stiffness.

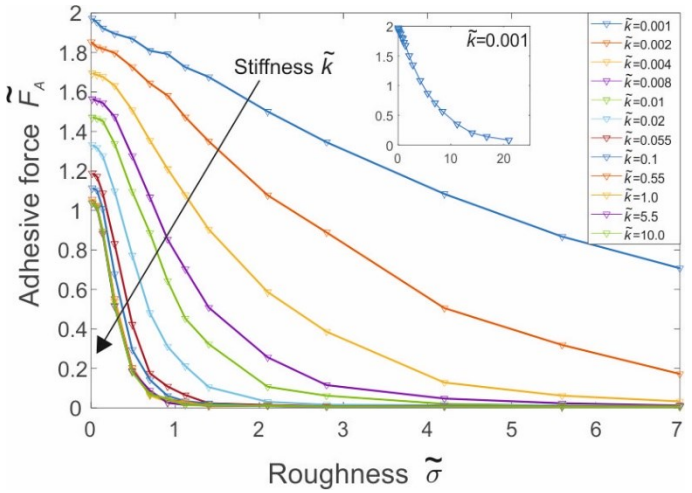

(a)

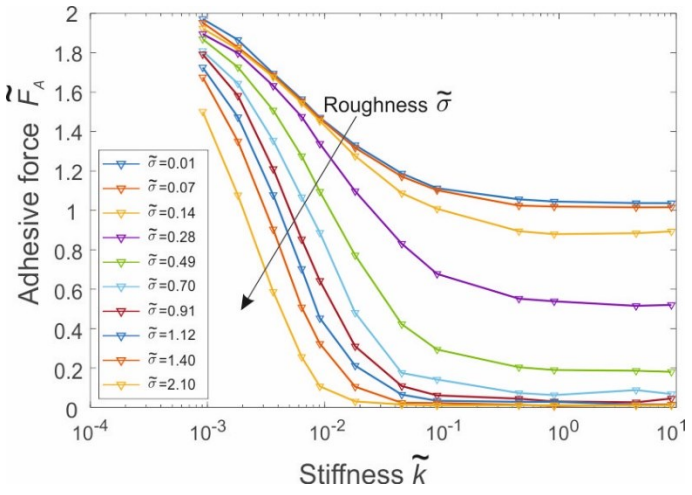

(b)

Figure 5-6 Dependence of the adhesive force at the plateau on roughness (a) and stiffness (b).

In last chapter, it was found that the deflection of the elastic half-space is very slight, when the stiffness lies at a very small value. Here for cases of $\tilde{\sigma} \to 0$, the very soft pillars become much more independent of each other, and thus, the stronger adhesive force was obtained. However, when the stiffness is large, the interaction among pillars can not be ignored, which leads to stress distribution being unequal for different pillars, and then decreasing the adhesive force. Figure 5-6 shows that decreasing stiffness approaches the initial concept

of contact splitting. In this limit (and only in this limit), the contact splitting really gives rise to a high adhesion enhancement in comparison with the compact surface [73][118][121]. While adhesion for a model with stiff structure attaching to a very rough substrate becomes weak and even disappears.

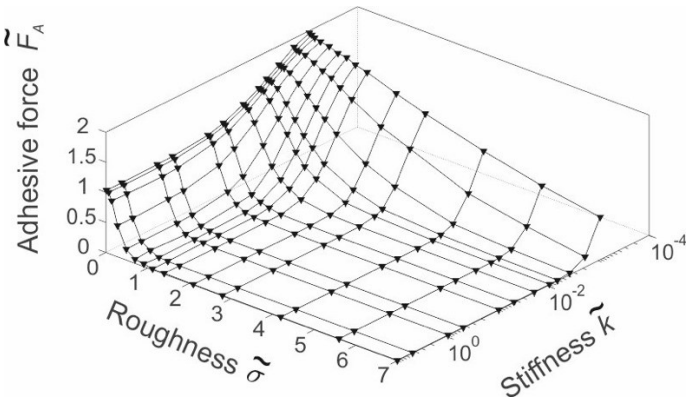

Figure 5-7 Dependence of the adhesive force on the combined influence of stiffness and roughness.

In Figure 5-7, we plot the dependence of the adhesive force on the combined effect of roughness and stiffness, and the large adhesive force exists in a very narrow region, and it drops quickly to zero either roughness or stiffness becomes large.

5.3 Conclusions

We studied the adhesive strength of rough brush-structure as a function of pillar stiffness. The case of rigid pillars has been investigated recently [76]. Observing the transition between the cases with very rigid- and extremely soft pillars, we identified the relevant parameters of this transition and studied the transition in dependence of all essential material and loading parameters as preload, roughness and pillar stiffness.

It is known that roughness and stiffness affect the strength of adhesion significantly. When stiffness was determined, simulation results showed that the adhesive force firstly increased approximately linearly with the preload for the weak compression, then reached a plateau (which level depended on system parameters) and became preload-insensitive as preload kept increasing. When roughness was determined, the maximum adhesive force in the plateau region increased with decreasing stiffness. A critical roughness, at which adhesion disappeared, existed for every determined stiffness, and this value became larger for cases of smaller stiffness. It is found that softer pillars have much better adaptability to comply with larger roughness, and thus, the detrimental effect of roughness can be compensated by decreasing stiffness. With increasing stiffness, the maximum adhesive

force as well as the adhesion coefficient would rapidly converge to them of the rigid case, especially here for cases of $\tilde{k} \geq 0.55$, all results practically collapsed together. In particular, we determined the pillar stiffness needed to make the adhesion stress 'tolerant' to the roughness, and an enhancement of adhesion was obtained by decreasing stiffness.

Chapter 6 The influence of hierarchy on adhesive contact of multi-level brush-structure

As described in Chapter 1, it is observed that there are hierarchical structures of millions of micro-fibrils on the gecko's foot pad. The so-called lamella-seta-spatula hierarchical fibrillar structure [130]-[132], possesses high compliance to ensure intimate contact with a rough substrate [133], and then generates strong adhesion [134][135]. Many theoretical and numerical models have been developed to mimic this biological attachment system [67][136][137]. For example, Bhushan et al. considered three-level structured spring models for simulation of the hierarchical structure contacting with randomly rough surfaces, and the DMT theory was applied to each spring in the bottom level [137]. They obtained a 36-times larger adhesive strength relative to a gecko's weight for the case of a very smooth surface. Schargott proposed a multi-layer model to investigate the adhesive contact on rough surfaces [67], and suggested that a stronger adhesive force was obtained through increasing number of hierarchical layers.

In this chapter, we develop the BEM further for the hierarchical brush-structure. One-, two- and three-level structures are constructed to investigate the effect of structural hierarchy on adhesive contact. An equivalent single-level structure for obtaining the same maximum (preload-insensitive) adhesive force, is numerically studied.

6.1 Numerical model

6.1.1 Modeling of hierarchical structure

Now we consider the multi-level hierarchical structure based on the studies in previous chapters. Similarly, the elastic connections between rigid cylinders and the rigid base are modelled by the linear springs, but in a multi-level form. Figure 6-1 illustrates one-, two- and three-level models. One can roughly analogize this multi-level model to the microstructure of gecko's foot pad. The smallest pillars at the bottom contacting with the substrate, represent the *spatula*. Then a *cluster* of 'spatulae'-pillars is embedded together into a relatively larger 'seta'-pillar in the *middle-level* structure. In the same way, 'seta'-pillars are connected to '*lamella*'-pillar in the *third-level* structure.

Generally, we set the pillars in different levels with length L_1, L_2, L_3, radii r_1, r_2, r_3, and pillar stiffness k_1, k_2, k_3. In next section, we will determine the equilibrium status of all pillars in different levels.

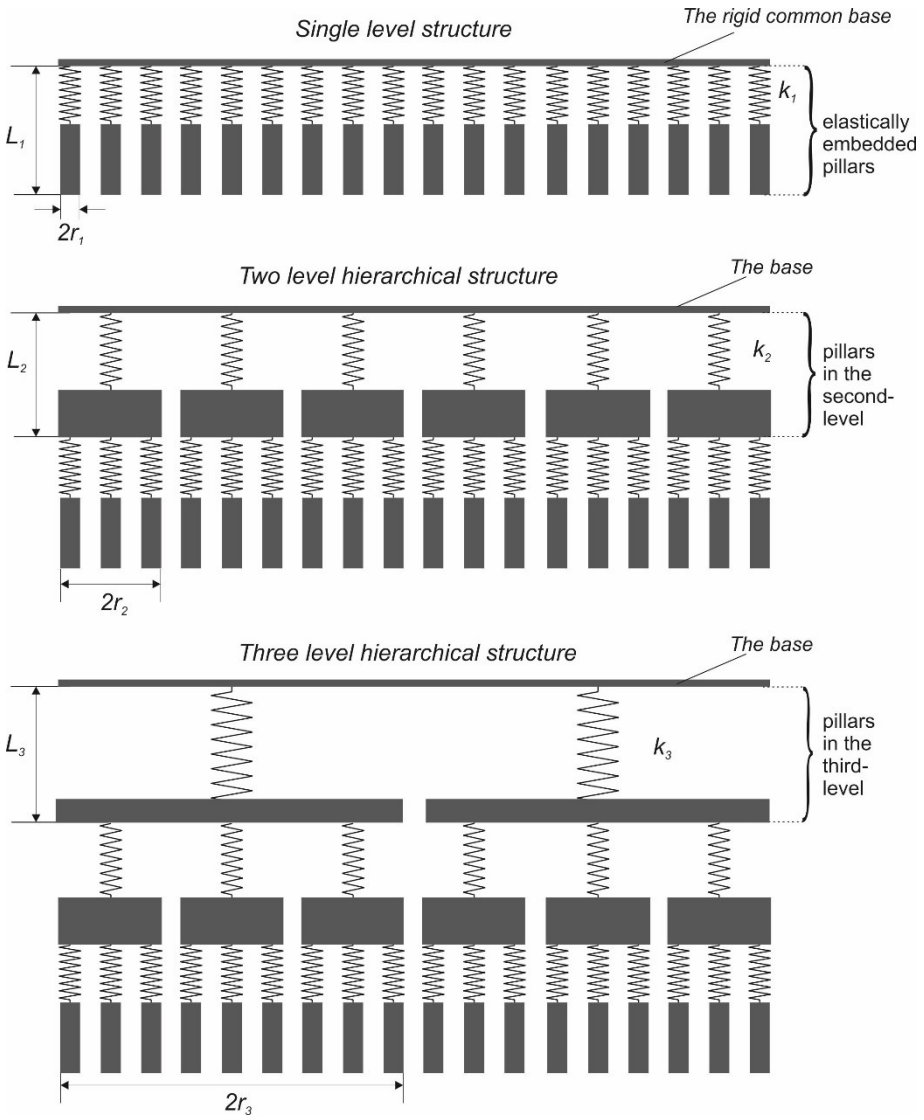

Figure 6-1 Schematic illustration of hierarchical structure with one-, two- and three levels.

6.1.2 Numerical method based on the BEM

For the single-level brush-structure, we have developed an effective algorithm based on the BEM in Chapter 3. With a given general displacement of the rigid base, the deflection of all pillars as well as the stress distribution can be very effectively calculated. In the same way, we design a new algorithm for the multi-level brush-structure.

We briefly repeat the most important relations in the case of single-level structure here, which can be regarded as the footstone to analyze the multi-level models. For a given

general displacement d (the displacement of the base), the geometrical condition needs to be satisfied. For example, within the *n*-th pillar's contact area $A_{1,n}$

$$d = u_n + \Delta l_{1,n}\,, \tag{6.1}$$

where u_n is the deflection of the elastic half-space, and $\Delta l_{1,n}$ is the deflection of the *n*-th pillar. The *n*-th pillar is under force equilibrium

$$f_n = k_1 \Delta l_{1,n} = \int_{A_{1,n}} p_n \mathrm{d}A_{1,n}\,, \tag{6.2}$$

where p_n is the stress acting on the elastic half-space within $A_{1,n}$. Then, the geometrical condition for this pillar can be rewritten as

$$u_n = d - \frac{1}{k_1}\int_{A_{1,n}} p_n \mathrm{d}A_{1,n}\,, \tag{6.3a}$$

or in a discrete form (u_n and p_n are transferred to matrix form in two-dimensional discretization)

$$u_n = d - \frac{1}{k_1}\sum_{A_{1,n}} p_n h^2\,, \tag{6.3b}$$

where h is the size of elemental meshes. The relation between the normal deflection of the elastic half-space and the normal traction is described by the Boussinesq's solution as in Chapter 3.

In the BEM, the relation between deflection and stress can be rewritten in a discrete form

$$u_{ij} = K_{iji'j'} p_{i'j'}, \tag{6.4a}$$

$$u = K * p, \tag{6.4b}$$

where u_{ij} is the displacement of the surface element at position (i,j), $p_{i'j'}$ is the normal stress acting on the element (i',j'), and $K_{iji'j'}$ is the influence matrix.

We have introduced a new matrix Π_1 to determine pillars' deflection, and thus, the relation between the general displacement and the corresponding stress distribution can be expressed as

$$d = \frac{h^2}{k_1}\Pi_1 * p + K * p = \left[\frac{h^2}{k_1}\Pi_1 + K\right] * p. \tag{6.5}$$

Now we introduce hierarchy into our current method. For a *two-level* structure as shown in Figure 6-2, we pressed it against the elastic half-space by a general displacement d. For a

clear description, the pillar in the bottom level is called *sub-pillar* (a cluster of sub-pillars is connected to a common pillar in the second level).

For the k-th pillar in the second level, it has deflection $\Delta l_{2,k} = L_{2,k} - L'_{2,k}$, so the spring force (in the second level) acting on the k-th pillar is equal to

$$F_{2,k} = k_2 \cdot \Delta l_{2,k}. \tag{6.6}$$

Correspondingly, the sub-pillars which belong to the k-th pillar (i.e. the k-th cluster), have deflection $\Delta l_{1,kn}$ (e.g. for the q-th sub-pillar: $\Delta l_{1,kq} = L_{1,kq} - L'_{1,kq}$ as shown in Figure 6-2), and the sum of these spring forces (within the k-th cluster) must equal $F_{2,k}$

$$\sum_{n \in k-\text{th cluster}} k_1 \cdot \Delta l_{1,kn} = F_{2,k}. \tag{6.7}$$

On the other side, the sum of stress p acting on these sub-pillars (from the elastic half-space) must equal $F_{2,k}$ as well

$$\sum_{n \in k-\text{th cluster}} ph^2 = \sum_{n \in k-\text{th cluster}} k_1 \cdot \Delta l_{1,kn} = k_2 \cdot \Delta l_{2,k} = F_{2,k}. \tag{6.8}$$

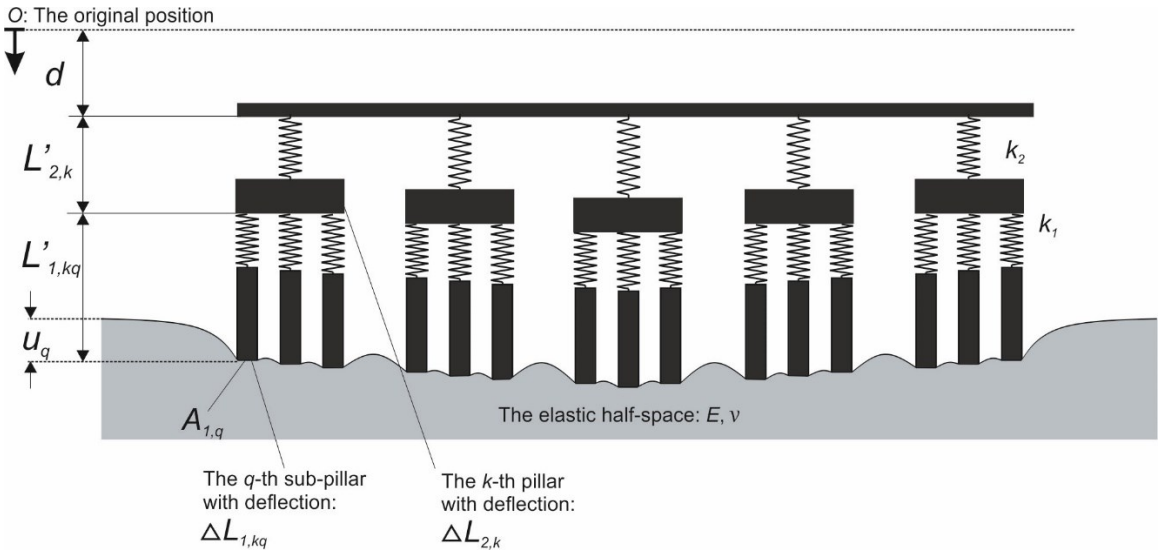

Figure 6-2 Illustration of the equilibrium status of a two-level structure. d is the general displacement of the base. For the q-th sub-pillar, $L'_{1,kq}$ represents the new balanced length and u_q is the corresponding deflection of the elastic half-space. For the k-th pillar (in the second level), $L'_{2,k}$ is the new balanced length.

For such a two-level structure, considering the deflection of pillars in the first and second level, the general geometrical condition is

$$d = u + \Delta l_1 + \Delta l_2. \tag{6.9}$$

For the first and second term on the right-hand side, we have already another expression in Eq. (6.5), then we obtain

$$d = K * p + \frac{h^2}{k_1}\Pi_1 * p + \Delta l_2. \tag{6.10}$$

It is expected that Δl_2 can be rewritten as a convolution form as well. Let us look at the q-th sub-pillar, the geometrical condition of $\Delta l_{1,kq}$, $\Delta l_{2,k}$ and u_q (as in Figure 6-2) can be expressed as

$$d = u_q + \Delta l_{1,kq} + \Delta l_{2,k}, \tag{6.11a}$$

$$d = [K * p]_q + \left[\frac{h^2}{k_1}\Pi_1 * p\right]_q + \Delta l_{2,k}. \tag{6.11b}$$

Compared with the single-level structure, the two-level structure has an *extra term* $\Delta l_{2,k}$. Furthermore, using Eq. (6.8) to substitute $\Delta l_{2,k}$ yields

$$d = [K * p]_q + \left[\frac{h^2}{k_1}\Pi_1 * p\right]_q + \frac{h^2}{k_2}\sum_{n\in k-\text{th cluster}} p\,. \tag{6.12}$$

Here, Π_1 plays *two* really important roles, e.g. for the q-th sub-pillar:

1. $[\Pi_1 * p]_q$ is used to sum the stress that acts only on the q-th sub-pillar.
2. Π_1 is used to exclude elements (of contact area) that do not belong to the q-th pillar.

Therefore, the convolution $\left[\frac{h^2}{k_1}\Pi_1 * p\right]_q$ is guaranteed to equal the deflection of the q-th sub-pillar $\Delta l_{1,kq}$.

Similarly, we introduce a matrix Π_2 for the second level, e.g. for the k-th pillar:

1. $[\Pi_2 * p]_k$ is to sum the stress acting on the sub-pillars within the k-th cluster.
2. Π_2 is to exclude those elements which do not belong to the k-th cluster.

The only difference between Π_1 and Π_2 is that Π_1 is constructed for one sub-pillar, while Π_2 for several sub-pillars which belong to the same cluster. The size of Π_1 and Π_2 is illustrated in Figure 6-3.

Therefore, the relation of Π_1 and Π_2 can be expressed as

$$[\Pi_1 * p]_q = \sum_q p\,, \tag{6.13a}$$

$$[\Pi_2 * p]_k = \sum_k [\Pi_1 * p]_q = \sum_k \sum_q p\,. \tag{6.13b}$$

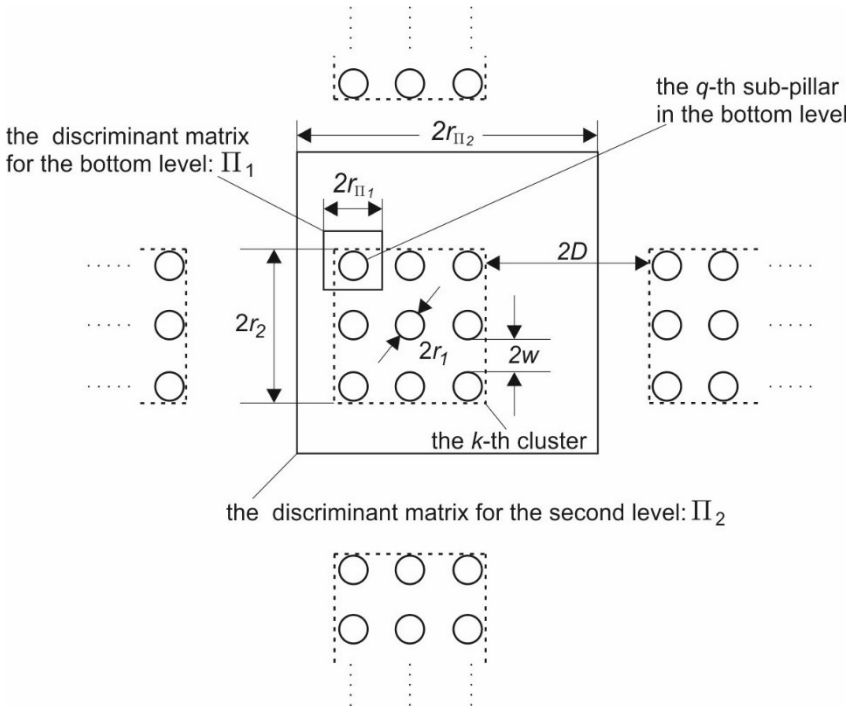

Figure 6-3 Illustration of the discriminant matrix and geometrical relation for two-level structure. Sub-pillars are regularly distributed. The radius of sub-pillar is r_1, and the size of the k-th cluster (i.e. the k-th pillar in the second level) is $2r_2 \times 2r_2$. The gap between two adjacent sub-pillars is $2w$, while the gap between two adjacent clusters is $2D$. In the following, we assume that gap is larger than pillars' size ($r_1 \leq w, r_2 \leq D$). The discriminant matrix for the bottom level Π_1 has the condition $2r_1 \leq r_{\Pi 1} \leq 2w$, and the discriminant matrix for the second level Π_2 has the condition $2r_2 \leq r_{\Pi 2} \leq 2D$.

So far, we can rewrite Eq. (6.12) as

$$d = \left[\frac{h^2}{k_1}\Pi_1 + \frac{h^2}{k_2}\Pi_2 + K\right] * p. \tag{6.14a}$$

Therefore, we obtain a similar form as Eq. (6.5). The stress distribution p is only coupled with the general displacement d. Using the conjugate-gradient method to solve the inverse problem, we can determine p for a given d, and we can accelerate the calculation by applying the FFT, as described in Chapter 3, hence

$$d = \mathrm{IFFT}\left[\mathrm{FFT}\left(\frac{h^2}{k_1}\Pi_1 + \frac{h^2}{k_2}\Pi_2 + K\right) \cdot \mathrm{FFT}(p)\right]. \tag{6.14b}$$

Separately, all parameters can be determined

$$u = K * p, \tag{6.15a}$$

$$\Delta l_1 = \frac{h^2}{k_1}\Pi_1 * p, \tag{6.15b}$$

$$\Delta l_2 = \frac{h^2}{k_2}\Pi_2 * p. \tag{6.15c}$$

As for the three-level structure, we can follow the same way to design a matrix Π_3 for the third level, then

$$d = \left(\frac{h^2}{k_1}\Pi_1 + \frac{h^2}{k_2}\Pi_2 + \frac{h^2}{k_3}\Pi_3 + K\right) * p. \tag{6.16}$$

Even for an *n*-level structure, we can accomplish the model by

$$d = \left(\sum_{i=1}^{n}\frac{h^2}{k_i}\Pi_i + K\right) * p, \tag{6.17}$$

$$\Delta l_i = \frac{h^2}{k_i}\Pi_i * p, \quad i = 1, \dots, n. \tag{6.18}$$

Considering *adhesion*, we still use the mesh-dependent detachment criterion, which is the same as cases of single-level structure in previous chapters.

6.2 Results and discussion

Based on the developed BEM, we have integrated the pillar stiffness of different levels directly into the influence matrix altogether. Then, the adhesive contact of such a multi-level structure can be numerically simulated in the same way as it in previous chapters. We construct three structures (with one-, two- and three levels), and some parameters are set as follows.

We consider a rough structure of the bottom level, to investigate the effect of roughness. Length of pillars is followed by the Gaussian function as presented in Chapter 5. The probability density function is described as

$$\Phi(l) = \frac{1}{\sqrt{2\pi\sigma}}\mathrm{e}^{-\frac{(l-l_0)^2}{2\sigma^2}}, \tag{6.19}$$

where σ and l_0 are the standard deviation and the mean value. We use σ to describe the characteristic roughness, and l is the length of pillars (in the bottom level) independently.

Since roughness is generally very smaller than pillars' length ($l \gg \sigma$), simply we assume that length of pillars in each level is approximately identical ($L_1 \approx L_2 \approx L_3$). Considering

the homogeneity of material E_p, the corresponding stiffness is $k = E_p \pi r_n^2 / L_n$, then we can determine the pillar stiffness of different levels based on the relation below

$$\frac{k_1}{r_1^2} = \frac{k_2}{r_2^2} = \cdots = \frac{k_n}{r_n^2}. \tag{6.20}$$

We set the filling factor of each level as φ_1, φ_2 and φ_3, then we can determine the stiffness according to Eq. (6.20)

$$k_1 = \varphi_1 k_2 = \varphi_1 \varphi_2 k_3. \tag{6.21}$$

The total filling factor is equal to

$$\varphi = \varphi_1 \varphi_2 \varphi_3. \tag{6.22}$$

We normalize the numerical results by the characteristic values of adhesive force and critical displacement in the case of a rigid flat brush-structure [75]

$$\tilde{F} = \frac{F}{F_c}, \tilde{d} = \frac{d}{d_c}, \tag{6.23}$$

where $F_c = \sqrt{8\pi E^* \Delta\gamma \varphi \left(\sqrt{A_0/\pi}\right)^3}$ and $d_c = \sqrt{\frac{2\pi\Delta\gamma\varphi\left(\sqrt{A_0/\pi}\right)}{E^*}}$ are the same as them in Chapter 5. The characteristic roughness σ and stiffness k are normalized as

$$\tilde{\sigma} = \frac{\sigma}{d_c}, \tilde{k} = \frac{k}{E^* L}. \tag{6.24}$$

It is clear that the hierarchy in a rigid multi-level brush-structure does not work (the rigid hierarchical structure is exactly the same as a rigid single-level structure). We focus on how the structural hierarchy affects adhesion, and thus, we firstly consider relatively small pillar stiffness. In this chapter, the filling factor is set as $\varphi_1 = 0.12$, $\varphi_2 = 0.45$, $\varphi_3 = 0.45$, and we set the stiffness in the bottom level $\tilde{k}_1$ as

$$\tilde{k}_1 = 10^{-3}. \tag{6.25}$$

Then according to Eq. (6.21)

$$\tilde{k}_2 = \frac{\tilde{k}_1}{\varphi_1} = 9 \times 10^{-3};\ \tilde{k}_3 = \frac{\tilde{k}_2}{\varphi_2} = 2 \times 10^{-2}. \tag{6.26}$$

6.2.1 Rough adhesive contact

To compare the adhesion behavior among one-, two- and three-level structures, we pick up 6 groups of pull-off process under different contact conditions. Results are shown in Figure

6-4. Generally, the structure with more levels possesses stronger adhesion, and the strongest adhesive forces for all three different structures appear under smooth contact condition with large preload ($\tilde{\sigma} = 0.04, \tilde{F}_P = 14.3$, in Figure 6-4 (b)).

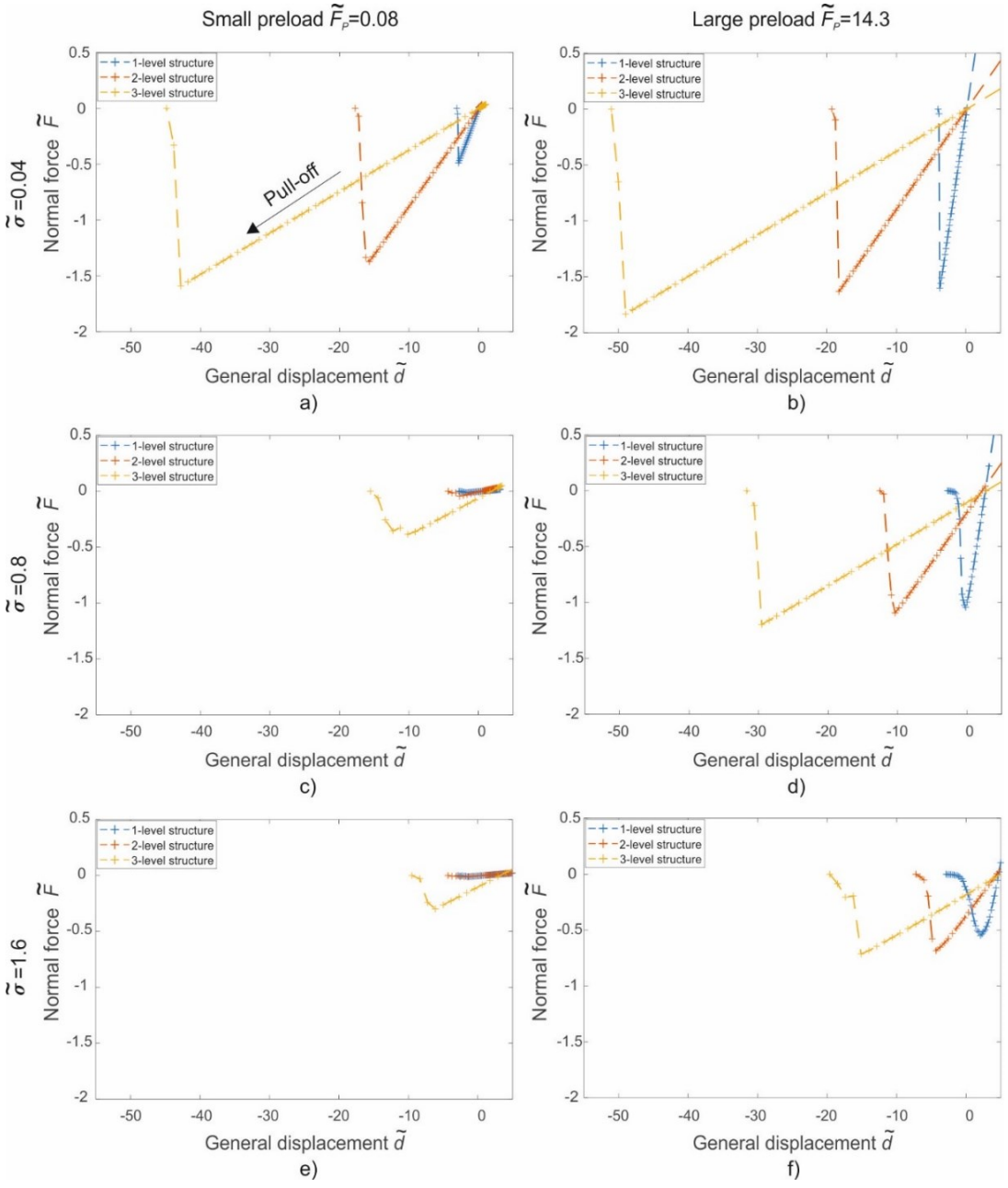

Figure 6-4 Examples of pull-off process of one-, two- and three-level structures with different roughnesses and preloads. The left side (a), (c) and (e) represent cases of small preload, while the right side (b), (d) and (f) represent cases of large preload. (a) and (b) $\tilde{\sigma} = 0.04$; (c) and (d) $\tilde{\sigma} = 0.8$; (e) and (f) $\tilde{\sigma} = 1.6$.

For cases of small preload (left column (a) (c) (e) in Figure 6-4), it is found that the three-level structure attains the largest adhesive force, compared with other two structures. Even

with large roughness, e.g. $\tilde{\sigma} = 1.6$, the adhesive force of the three-level structure reaches nearly $\tilde{F}_A = 0.4$, while adhesive forces of other two structures become very small and tend to zero. Under a large preload (right column (b) (d) (f) in Figure 6-4), a larger critical displacement appears in the case of the structure with more levels, which implies better toughness. The discrepancy of adhesive forces among the three structures becomes minor, as roughness increases.

It is clear that in rough contact, the preload will affect the initial contact area A, and then eventually affect the adhesive force. The dependence of the adhesive force on the preload for different roughnesses is shown in Figure 6-5. These values are averaged by 10 realizations of rough multi-level structures. Similar to the cases of rigid rough brush-structure in [76] and cases in Chapter 5: for a determined roughness, a curve can be divided into three parts: a linear region where the adhesive strength is practically proportional to the preload; a plateau region where the maximum adhesive force is obtained and independent of the preload; and a transitional zone between those two regions.

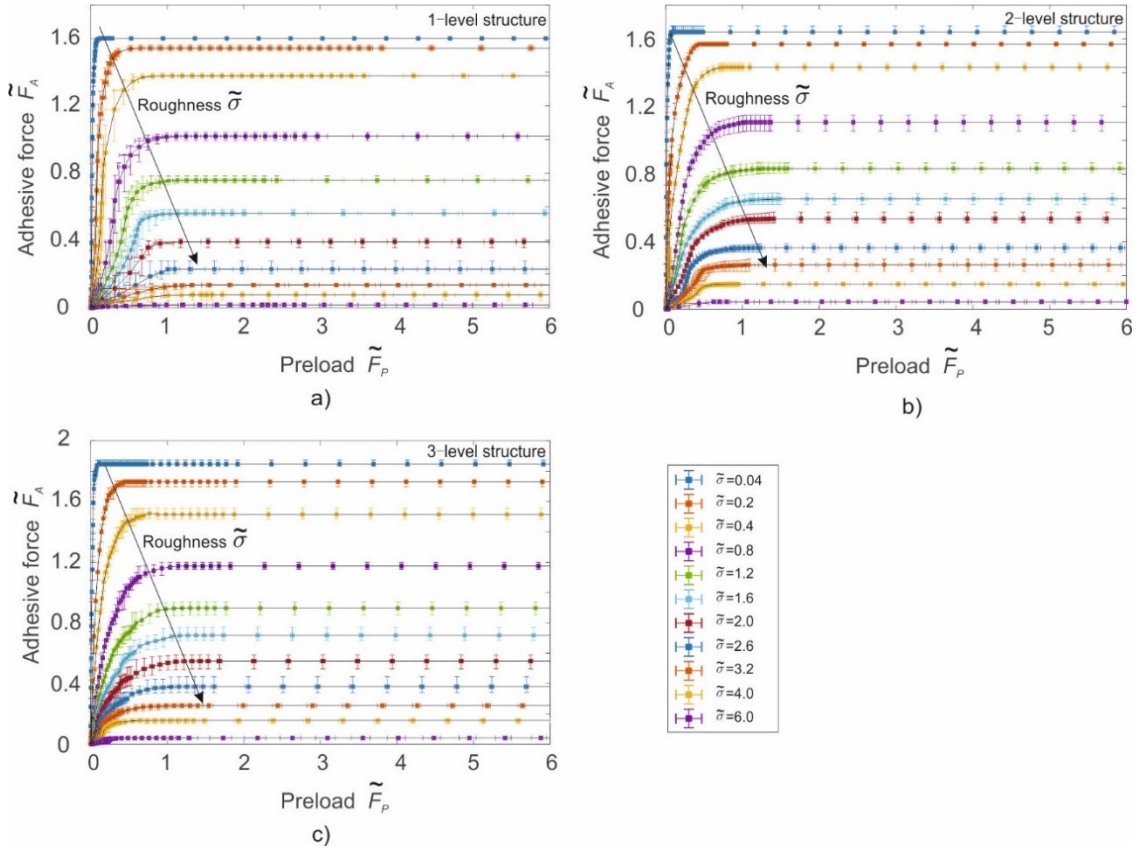

Figure 6-5 Dependence of the adhesive force on the preload for different roughnesses. (a) one-, (b) two- (c) three-level structures.

Observing one individual subfigure in Figure 6-5, one can see that for small roughness cases, the linear region is narrow and the adhesive force increases rapidly with preload. Furthermore, the maximum adhesive force at the plateau is higher, compared with large roughness cases.

Comparing the structures with different levels, a larger adhesive force at the plateau is observed in cases of structure with more levels. For example, in the case of small roughness $\tilde{\sigma} = 0.04$, adhesive force equals $\tilde{F}_A \approx 1.6$ for the single-level structure, and it slightly increases to $\tilde{F}_A \approx 1.65$ for the two-level structure, then it further enhances $\tilde{F}_A \approx 1.9$ for the three-level structure. A hierarchical structure with more levels becomes slightly more tolerant to roughness. However, similarly, the difference of adhesive force among the three structures, becomes smaller as roughness increases.

At the linear region, adhesion coefficient c is defined as the ratio of the adhesive force to the preload, $c = \tilde{F}_A/\tilde{F}_P$ [109][128]. The dependences of adhesion coefficient c at the linear region, and the maximum adhesive force $\tilde{F}_A$ at the plateau on the roughness are shown in Figure 6-6. For adhesion coefficient c in Figure 6-6 (a), similar results to the single level case in Chapter 5 are obtained that it decreases rapidly and tends to zero with roughness. The structure with more levels determines a relatively larger adhesion coefficient.

From Figure 6-6 (b), it is found that the adhesive force at the plateau generally decreases and approaches zero as roughness increases, and the three-level structure shows the slightly better ability to comply with roughness, compared with other two structures. This implies that the existence of hierarchy equivalently decreases the effective stiffness of the overall system, based on the finding in Chapter 5. When roughness becomes large ($\tilde{\sigma} > 2$), the effect of hierarchy turns weak, so that all curves go close to each other.

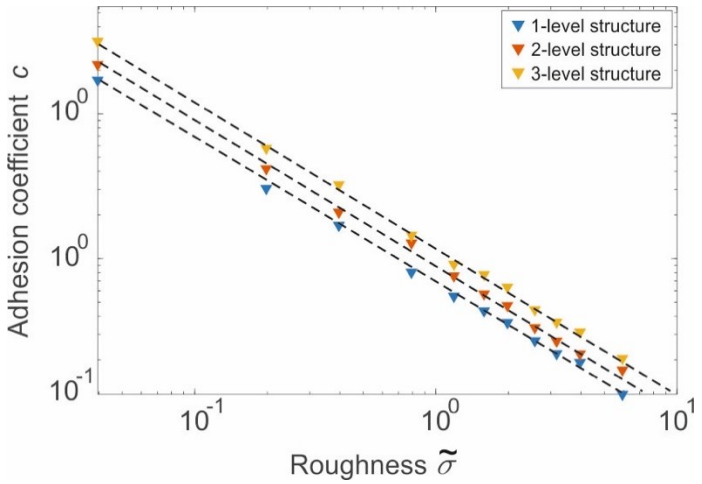

(a)

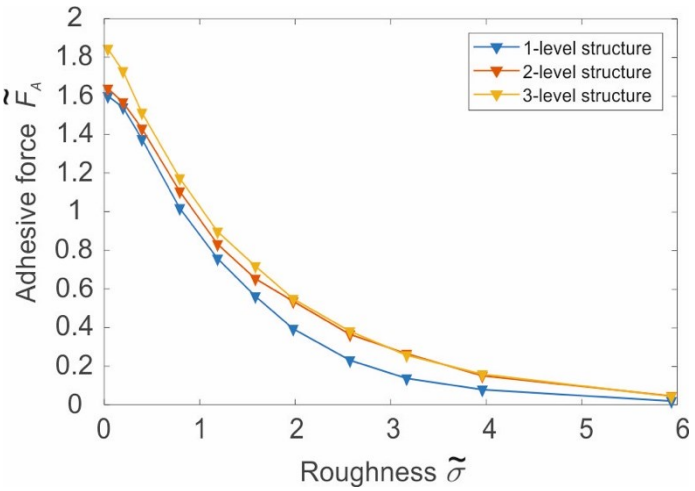

(b)

Figure 6-6 (a) Dependence of adhesion coefficient on roughness for different hierarchical structures in log-log form; (b) the maximum adhesive force at the plateau for different structures.

6.2.2 An equivalent single-level structure

In the hierarchical brush-structure, different layers are elastically connected in series, which can be theoretically estimated as a decrease of the effective stiffness of the whole system. We could thus find out an equivalent single-level structure to replace the multi-level structure

$$\sum_{i=1}^{n} \frac{h^2}{k_i} \Pi_i \triangleq \frac{h^2}{k_{1'}} \Pi_1 > \frac{h^2}{k_1} \Pi_1. \tag{6.27}$$

If we do not consider the interaction among pillars, a very simple relation between the effective stiffness $k_{1'}$ (of the equivalent single-level structure) and the k_1, k_2, k_3 (of the original three-level structure), can be obtained

$$\frac{1}{N_3 N_2 N_1} \frac{1}{k_{1'}} \approx \frac{1}{N_3} \left[\frac{1}{k_3} + \frac{1}{N_2} \left(\frac{1}{k_2} + \frac{1}{N_1} \frac{1}{k_1} \right) \right], \tag{6.28a}$$

$$\Rightarrow k_{1'} \approx \frac{1}{\frac{N_2 N_1}{k_3} + \frac{N_1}{k_2} + \frac{1}{k_1}}, \tag{6.28b}$$

where N_1, N_2 and N_3 represent the pillar number of each cluster in different levels, i.e. $N_3 \times N_2 \times N_1$ is the total number of pillars in the bottom level. With the values of k_1, k_2 and k_3 in Eqs (6.25) and (6.26) we obtain the equivalent $\tilde{k}_{1'} = 0.4 \times 10^{-4}$. Figure 6-7 (a)

shows the comparison of the adhesive forces at the plateau between the equivalent single-level structure and the original three-level structure, and Figure 6-7 (b) shows the dependence of the corresponding effective $k_{1'}$ on roughness.

The effective stiffness $k_{1'}$ increases rapidly with roughness, and then gradually tends to k_1, which is the stiffness of the bottom level in the original three-level structure. Therefore, the $k_{1'}$ approaches the theoretical estimation of Eq. (6.28) only under a very smooth contact condition.

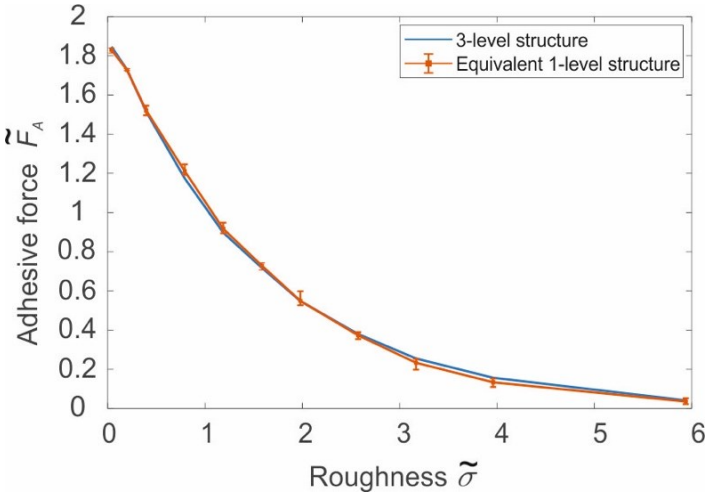

(a)

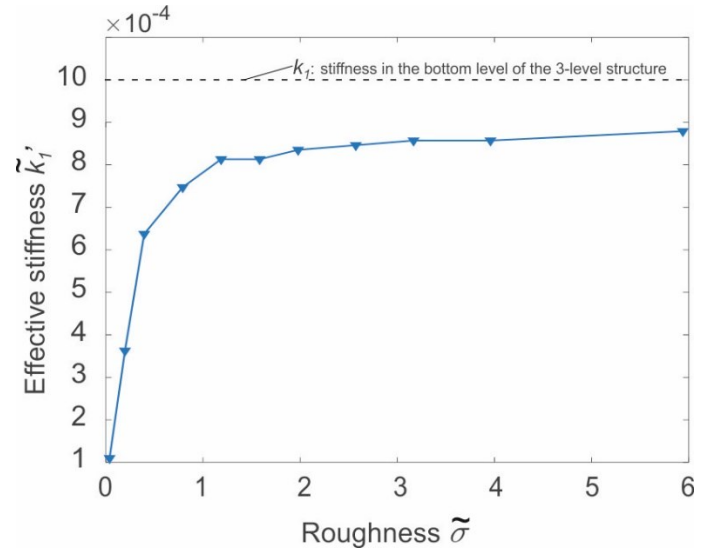

(b)

Figure 6-7 Comparison between the original three-level structure and the equivalent single-level structure; (a) Dependence of the adhesive force on roughness for the two structures; (b) Dependence of the effective stiffness of equivalent single-level structure on roughness.

It is found that, hierarchy results in smaller effective stiffness than stiffness k_1. This effect becomes weak with the increase of roughness since $k_{1'}$ approaches k_1 ($k_{1'} \to k_1$). Similarly, as shown in Figure 6-6 (b), adhesive forces for all structures approximately collapse together when roughness is large, and this also implies that the hierarchy's effect turns weak.

A hierarchical structure attains stronger adhesion in the case of small roughness. However, the effect of hierarchy is weakened gradually with increasing roughness, therefore the difference of adhesive force between hierarchical- and non-hierarchical structure becomes small.

6.2.3 Influence of stiffness

We vary the stiffness k_1 from 5×10^{-4} to 5×10^{-2}, to investigate the influence of pillar stiffness on adhesion. Stiffness k_2 and k_3 are also changed correspondingly based on Eq. (6.21) (under assumption of the homogeneity of material). In Figure 6-8 (a), a very limited enhancement of adhesion is observed for the multi-level structure when stiffness is small. This enhancement even disappears when stiffness is large. Therefore, hierarchy affects adhesion only when pillars are *soft*.

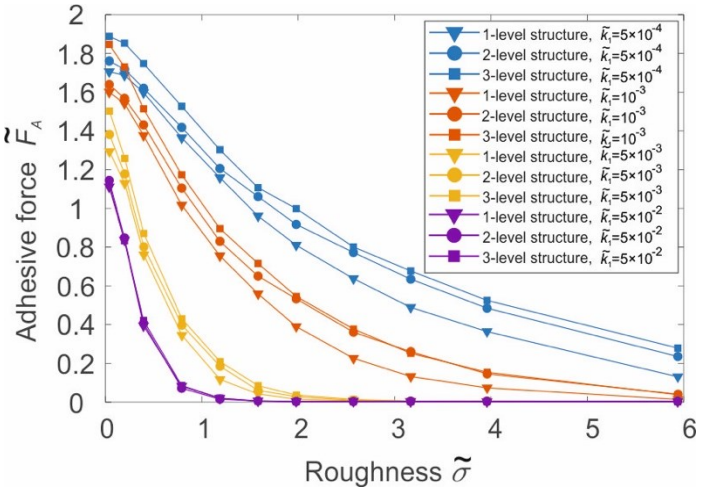

(a)

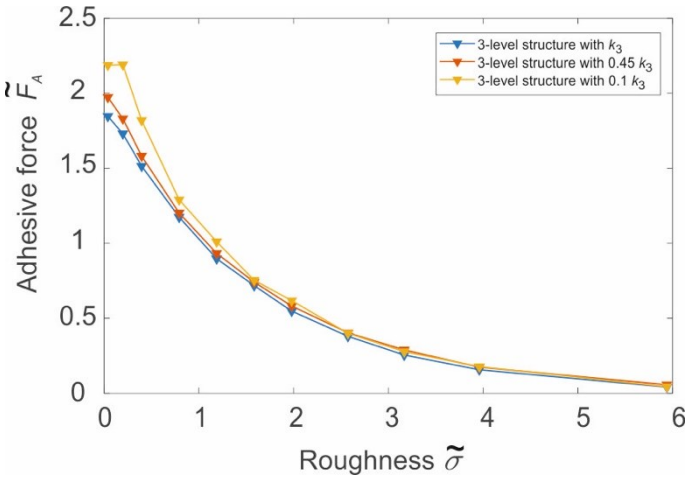

(b)

Figure 6-8 (a) Dependence of the maximum adhesive force of one-, two- and three-level structures on the roughness; (b) the maximum adhesive force with different k_3, but the same k_1 and k_2.

Considering k_3 being 20 times larger than k_1 ($\tilde{k}_3 = 2 \times 10^{-2}$), we adjust only the stiffness k_3 but keep k_1 and k_2 unchanged ($\tilde{k}_1 = 10^{-3}$ and $\tilde{k}_2 = 9 \times 10^{-3}$), to investigate the effect of top-level on adhesion. The dependence of the adhesive force on roughness is shown in Figure 6-8 (b). The adhesive force appears a minor improvement for the structure with small k_3. For the structure with $0.1k_3$, roughness has little effect on the adhesive force when $\tilde{\sigma} < 0.3$, but the top level's effect turns weak as roughness increases.

6.3 Conclusions

We developed the BEM further for the multi-level system for investigation of the influence of hierarchy on adhesive contact. Similar to the case of single-level structure, the pillar stiffness of different levels was directly introduced into the influence matrix of the BEM, then numerical simulation could be carried out exactly in the same way as in previous chapters.

We numerically studied the adhesive contact of rough hierarchical structures with one-, two- and three levels. Similar to the results in Chapter 5, it showed that the adhesive force increased linearly with the preload firstly, and it eventually kept constant. The maximum adhesive force at the plateau decreased when roughness became large.

It is found that the multi-level structure equivalently reduces the effective stiffness of the overall system, and then acquires increased compliance to roughness. Simulation results showed that a larger adhesion coefficient and larger adhesive force were obtained by

adding the number of hierarchical levels. However, this effect was quite *limited*, that only a slight enhancement was observed. Furthermore, hierarchy affected adhesion only for structures with very *soft* pillars, and no enhancement was obtained for cases of large stiffness.

We numerically studied an equivalent single-level structure with effective stiffness $k_{1'}$ for obtaining the same maximal adhesive force (independent of preload). It was found that the effective stiffness $k_{1'}$ became the minimum in the smooth contact. With increasing roughness, the effective stiffness $k_{1'}$ increased and tended to the stiffness of bottom level in the original three-level structure. Therefore, in general, the existence of hierarchy can improve adhesion, but this effect becomes weak and tend to disappear when roughness is large.

Chapter 7 Adhesive contact of concave-shaped brush-structure

In previous chapters, the adhesive contact of different elastic brush-structures has been investigated, and it is found that structure parameters such as pillar stiffness, pillar number and hierarchy all can affect adhesion. However, there is *stress concentration* appearing at the outer edge of the apparent area, which severely affects the local separation and then the final adhesive force. Experimental tests exhibited that spatulae at the end of gecko's foot pad, almost supported the same adhesion force [138]. The effect of equal load sharing (ELS) has been widely studied in recent years [15][138][139]. For example, Gao et al. proposed a fibrillar model, where fibrils are independent of each other, to mimic gecko's attachment system [139]. Then based on ELS, the individual adhesive force for all fibrils reaches simultaneously at the complete separation.

Following the concept of equal load sharing, we consider a brush-structure with macroscopic concave shape, where pillars' length distribution is artificially designed. This specific structure is expected to weaken the detrimental effect of stress concentration, and then, to let all pillars attain the individual theoretical adhesive force simultaneously at the complete separation. The influence of pillar stiffness, filling factor and concave shape is numerically investigated.

7.1 Optimized contact shape in adhesive contact

Compared with the Kendall's solution of a flat cylindrical punch, stronger adhesion was observed in the adhesive contact of a concave punch on an elastic half-space [140]. In order to obtain a uniform stress distribution p_c, the normal deflection of the elastic half-space within the contact region must meet the condition [141]

$$u(r) = \frac{4p_c R}{\pi E^*} \mathrm{E}\left(\frac{r}{R}\right);\ (r \le R), \tag{7.1}$$

where R is the radius of the concave punch, $\mathrm{E}\left(\frac{r}{R}\right)$ is the complete elliptic integral of the second kind, and E^* is the effective elastic modulus. Then the concave punch should have the following geometry

$$S_c(r) = \frac{4p_c R}{\pi E^*}\left\{\mathrm{E}\left(\frac{r}{R}\right) - \frac{\pi}{2}\right\};\ (r \le R), \tag{7.2}$$

where $S_c(0) = 0$. The profile $S_c(r)$ is shown in Figure 7-1.

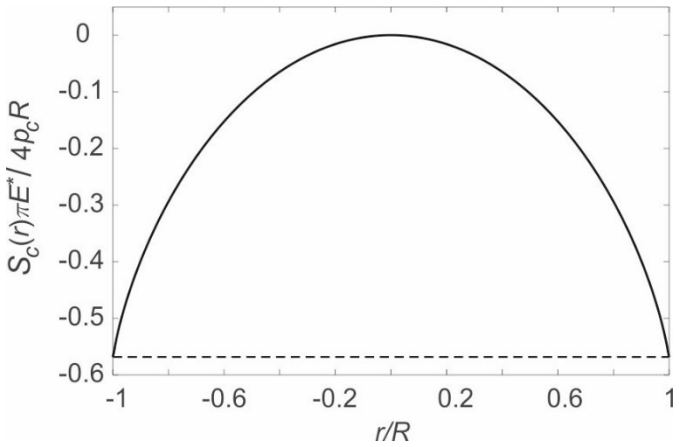

Figure 7-1 The geometry of concave punch for obtaining the uniform stress distribution.

In this chapter, we construct a brush-structure with the same macroscopic profile $S_c(r)$, but by an amplification factor $\tilde{h}$

$$S_p(r) = \tilde{h} \cdot S_c(r);\ (r \le R). \tag{7.3}$$

It is noted that the pillars are still flat-ended cylinders, but their length distribution follows the profile $S_p(r)$, as shown in Figure 7-2. The pillars are regularly distributed in a square area. For comparison, we also study the case of distribution in a circular area, as shown in the right illustration of Figure 7-2.

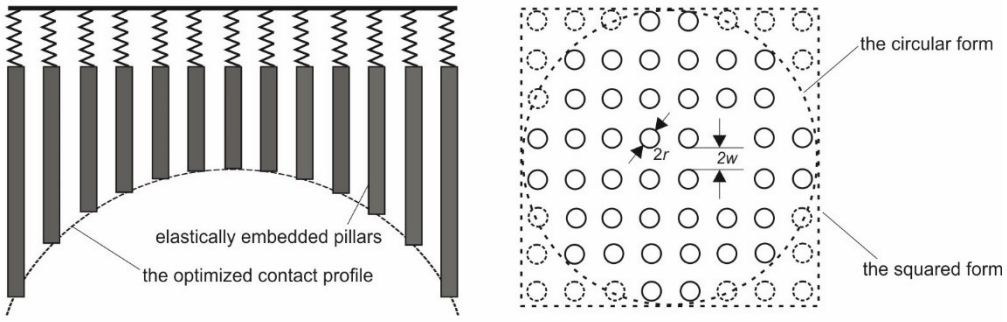

Figure 7-2 Illustration of a brush-structure with macroscopic concave shape. Pillars are flat-ended but their length distribution follows the profile Eq. (7.3). The right figure shows the pillar distribution in a circular or square form. $2r$ is the diameter of a single pillar and $2w$ is the spacing between two adjacent pillars.

The pull-off simulation of this structure is conducted using the BEM (for single-level model) and the influence of concave shape as well as pillar stiffness on adhesion is investigated.

7.2 Results and discussion

We only focus on the region of plateau, where the adhesive force is independent of the preload. In simulation, the concave-shaped brush-structure is firstly pressed against the elastic half-space deeply enough to obtain the complete contact, then pulled off until the complete detachment.

For the comparison with the *ideal situation* of equal load sharing, forces are normalized by the following value

$$\tilde{F} = \frac{F}{N \cdot F_K}, \tag{7.4}$$

where $F_K = \sqrt{8\pi E^* \Delta\gamma r^3}$ is the Kendell's solution for the single pillar with radius r, and N is the number of pillars, then $N \cdot F_K$ is simply the *maximum adhesive force*. The general displacement is normalized by the critical displacement in the case of rigid flat brush-structure

$$\tilde{d} = \frac{d}{\sqrt{\frac{2\pi\Delta\gamma\varphi\sqrt{A_0/\pi}}{E^*}}}, \tag{7.5}$$

where A_0 is the apparent area. The pillar stiffness is normalized as follows

$$\tilde{k} = \frac{k}{E^* L}. \tag{7.6}$$

We vary the factor $\tilde{h}$ to control the macroscopic contact shape. The influence of pillar stiffness and filling factor on the adhesion strength is investigated. In Figure 7-3, several examples of pull-off with factors $\tilde{h} = 0$, 0.04 and 0.8, but fixed stiffness $\tilde{k} = 0.1$, are extracted. Cases of $\tilde{h} = 0$ corresponds to the flat structure with uniform pillars' length, and it is seen that there is no obvious difference between the circular and square form, and the adhesive force is about $\tilde{F}_A \approx 0.65$. With a slightly larger factor $\tilde{h} \approx 0.04$, a stronger force is observed at $\tilde{F}_A \approx 0.95$. However, for a very larger factor $\tilde{h} = 0.8$, adhesion almost vanishes.

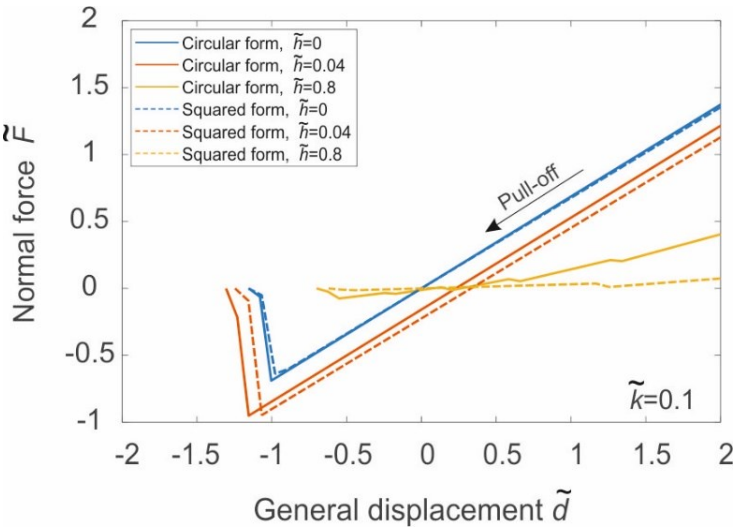

Figure 7-3 Dependence of the normal force on the displacement. Pillar stiffness and filling factor are fixed as $\tilde{k} = 0.1$ and $\varphi = 0.06$.

It is known that in the JKR-type adhesive contact of flat punch, there is singularity (stress concentration) at the boundary of the contact region. Of course, it will also exist on the circular contact area of each pillar in a brush-structure. However, for a concave-shape structure, one can still observe a reduction of the macroscopic stress concentration. The stress distribution at the critical moment for cases of circular form structure with $\tilde{h} = 0$ and 0.04 are shown in Figure 7-4. Here, only the crosssection of the normal stress distribution is presented for a clear view. It can be found that macroscopic stress concentration exists in the case of flat structure ($\tilde{h} = 0$) in Figure 7-4 (a). However, the concave shape in the case of $\tilde{h} = 0.04$ really optimizes the stress more uniformly as shown in Figure 7-4 (b). This implies that, in the case of flat structure, the separation occurs in the way of propagation (the detachment of pillars is sequential). While in the case of optimized (concave) structure, almost all pillars detach at the same time (this approaches the concept of equal load sharing).

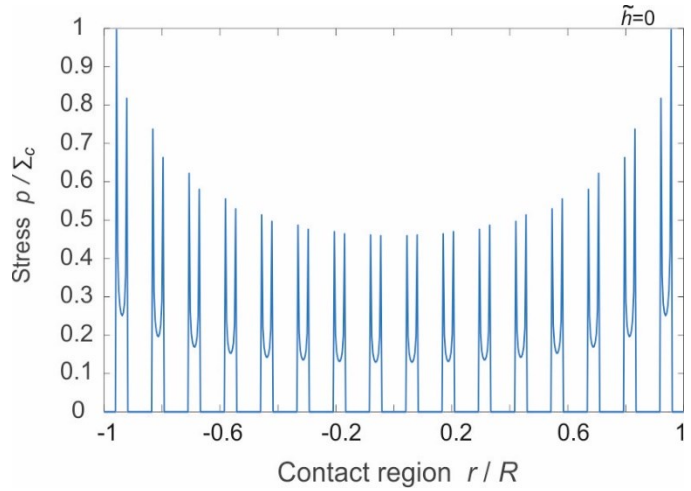

(a)

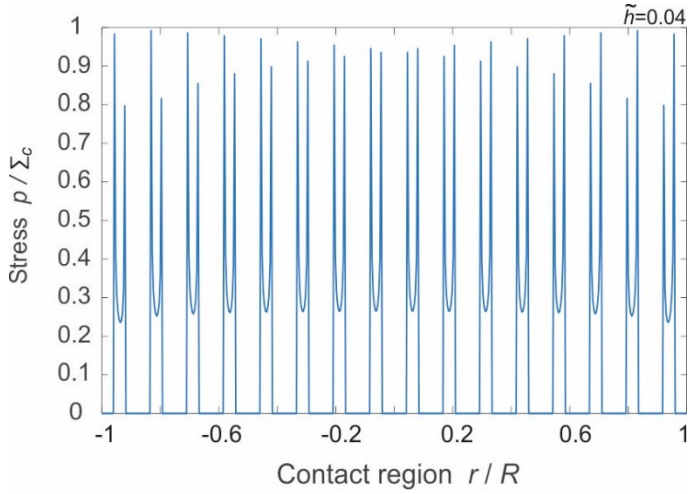

(b)

Figure 7-4 Cross-section of stress distribution on the elastic half-space at the critical moment. (a) $\tilde{h} = 0$; (b) $\tilde{h} = 0.04$. Σ_c is the critical value of the stress criterion in the BEM.

We vary the factor $\tilde{h}$ from 0 to 2 for finding the optimal shape for the maximal enhancement. The dependence of the adhesive force on the amplification factor for two different filling factors is shown in Figure 7-5. The maximum adhesive force is $\tilde{F}_A \approx 0.88$ at $\tilde{h} \approx 0.16$ for the case of large filling factor $\varphi = 0.15$. While it is $\tilde{F}_A \approx 0.95$ appears at $\tilde{h} \approx 0.5$ in the case of small filling factor $\varphi = 0.06$.

It is noted that the dimensionless forces $\tilde{F}_A$ for different filling factors are not comparable, since they are normalized by the ideal case of equal load sharing with the (different) individual contact area (see Eq. (7.4)). Thus, the forces $\tilde{F}_A$ indicates the level of approaching equal loading sharing.

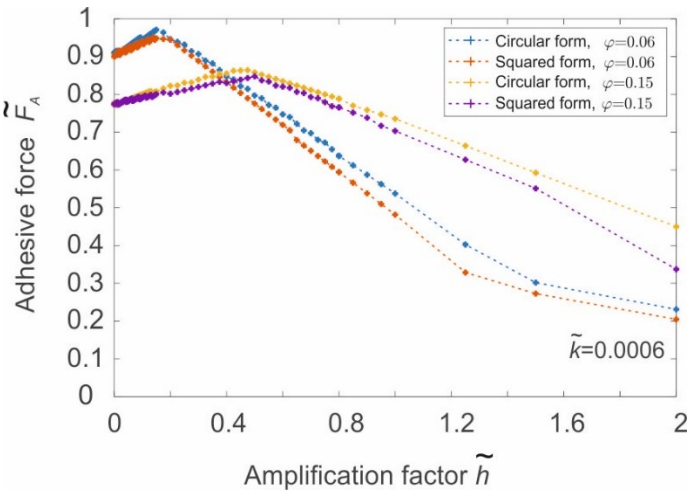

Figure 7-5 Dependence of the adhesive strength on the amplification factor. $\tilde{k} = 0.0006$.

The relation above for more different pillar stiffnesses in the case of circular form is illustrated in Figure 7-6. For the given filling factor, the maximum adhesive force $\tilde{F}_{A,max}$ are almost same for all stiffnesses, but the maximum adhesive force in smaller stiffness cases appears at a larger factor $\tilde{h}$. It is found that the smaller stiffness case has a much wider range of adhesion enhancement. For stiff cases, the change of adhesive forces is sensitively dependent on the factor $\tilde{h}$. For example in Figure 7-6 (a), for the stiffest case of $\tilde{k} = 10$, the adhesive force $\tilde{F}_A \approx 0.94$ at the factor $\tilde{h} = 0.04$ while it drops acutely to $\tilde{F}_A \approx 0.77$ at $\tilde{h} = 0.05$. These both structure shapes are very close to each other, but a small change affects the adhesion dramatically.

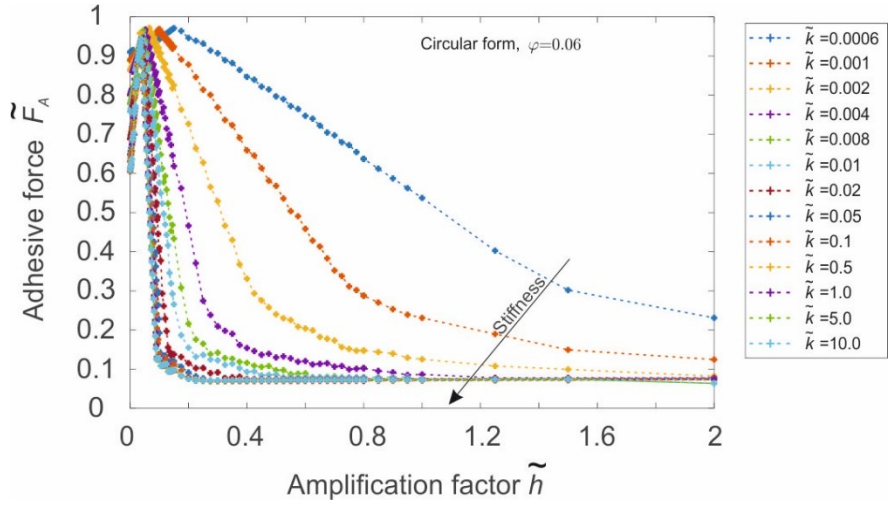

(a)

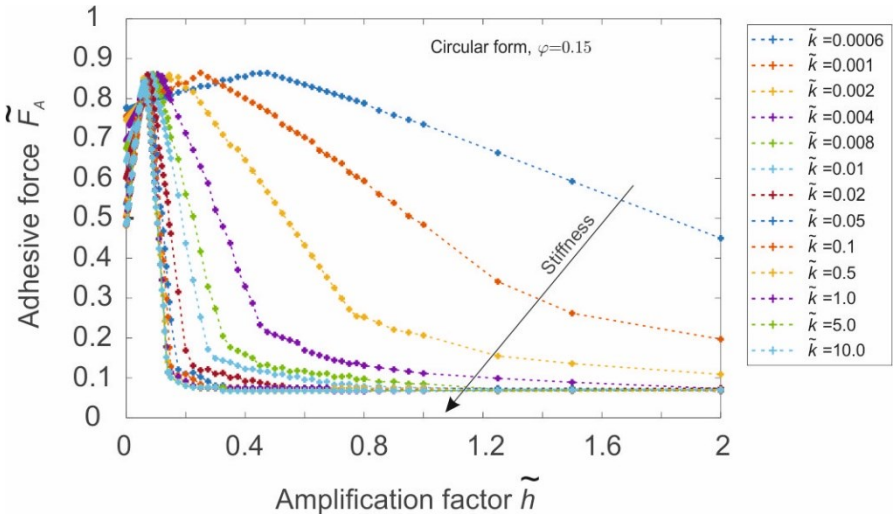

(b)

Figure 7-6 Dependence of the adhesive force on the factor $\tilde{h}$ for different stiffnesses. A circular form structure with (a) $\varphi = 0.06$; (b) $\varphi = 0.15$.

The relation between the adhesive force and the factor $\tilde{h}$ in Figure 7-6 supports a possible way to control adhesion by regulating (if possible) the factor $\tilde{h}$. Strong adhesion with small $\tilde{h}$ will be obtained when a stable attachment is needed, and the adhesion effect can be eliminated with large $\tilde{h}$ when an easy detachment is expected. With small pillar stiffness, one can regulate the factor $\tilde{h}$ with a wide tolerance (range), to avoid the severe change of adhesive force.

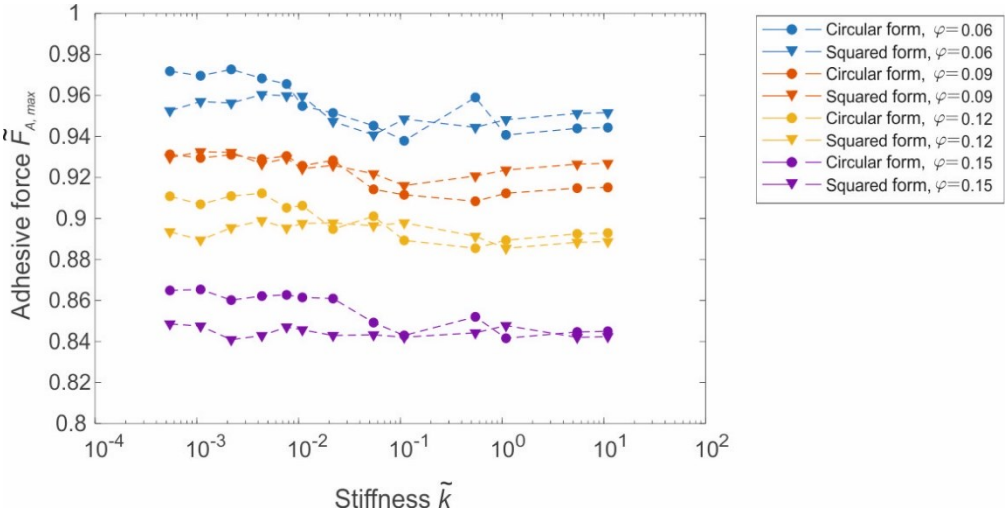

Figure 7-7 Dependence of the adhesive strength (of the optimized structures) on stiffness with different filling factors.

Figure 7-7 shows the dependence of the maximum adhesive strength $\tilde{F}_{A,max}$ on the stiffness with different filling factors. As described previously, both the geometry form and the pillar stiffness have a very slight influence on the maximal adhesive force. However, a smaller filling factor φ leads to a better effect of equal load sharing.

7.3 Conclusions

In this chapter, we numerically studied the adhesive contact between a brush-structure with concave shape and an elastic half-space. Through controlling the macroscopic concave shape of structure, the stronger adhesive force can be obtained compared with it of flat profile. A concave contact shape can greatly optimize the stress distribution more uniformly, and reduce the effect of stress concentration at the outer edge of the apparent contact area. It is observed that the adhesion enhancement can be achieved by setting a proper factor $\tilde{h}$ instead of decreasing pillar stiffness. Regulating the contact shape offers a possible way to obtain controllable adhesion.

Chapter 8 Summary and outlook

8.1 Summary

Inspired by the biological adhesion, a brush-structure with a large number of elastically embedded pillars has been modeled to mimic the microstructure of gecko's adhesion system. The adhesive contact of different brush-structures was theoretically and numerically studied using the effective BEM in this thesis. The influence of structure stiffness (pillar stiffness), loading parameter and geometry of structure (e.g. macroscopic contact shape, pillar number and pillar distribution) on the adhesion behavior of brush-structures, was systematically analyzed.

It is found that the pillar stiffness has a notable influence on the adhesion of brush-structure. The adhesive contact of a single pillar was numerically investigated using an iterative method based on the existing BEM for rigid indenters in Chapter 2. It was observed that the work of separation varied significantly with the pillar stiffness. For the complete separation of a single pillar from the elastic half-space, more external work was necessary in cases of small stiffness.

For effective simulation of multi-pillars model, we have designed a new algorithm based on the FFT-assisted BEM in Chapter 3. By introducing a simple *discriminant matrix* Π for the pillar stiffness, we can replace the elemental-wise summation of stress with a more efficient *convolution* operation. This discriminant matrix was directly integrated into the influence matrix of the existing BEM, and thus, the computational time decreases dramatically without reducing accuracy.

With the help of the new algorithm, a series of simulations have been carried out to investigate different structures:

(1) The flat brush-structure was studied to compare with the contact splitting theory in Chapter 4. By altering the pillar stiffness, we linked two limiting cases of rigid pillars (i.e. the rigid brush model) and extremely soft pillars (i.e. the contact splitting model). The transition between these two limiting cases was numerically obtained. It is found that the adhesion enhancement is dependent on the number of pillars, the pillar stiffness as well as the density of pillar distribution. Structures with *finer sub-contact surfaces*, *softer pillars* can obtain stronger adhesion.

(2) The adhesive contact of rough brush-structure was studied in Chapter 5. Under small preloading, the adhesive force was proportional to the preload. The adhesion coefficient as a function of pillar stiffness and roughness under small preloading was numerically found.

With large enough loading, the adhesive strength became preload-insensitive. It is found that soft pillars have much better compliance to large roughness, and the detrimental effect of roughness can be compensated by decreasing stiffness. Thus, the pillar stiffness is needed to make the adhesion stress 'tolerant' to the roughness.

(3) The hierarchical brush-structure was studied for investigation of the influence of multi-level structure on the adhesive strength in Chapter 6. The BEM was further developed for this system and discriminant matrix for each hierarchical layer was introduced into the BEM. The simulation results showed that the existence of hierarchy decreased the effective stiffness of the overall system essentially and thus improved the adhesive strength. The stronger adhesion can be obtained by increasing the number of hierarchical levels, but this increasing effect is very *limited* and even disappears in large roughness cases.

(4) In Chapter 7, the brush-structure with a macroscopic concave shape was constructed for weakening the general stress concentration and obtaining the effect of equal load sharing. The adhesion enhancement obtained by reducing the pillar stiffness, can be equivalently achieved by regulating the *concave* contact shape. Through controlling the concave contact shape, it is possible to achieve controllable adhesion.

8.2 Future work

The results obtained in this work could be helpful for further understanding of the bio-adhesion, especially the influence of pillar stiffness. However, as stated in the assumption in Chapter 1, there are some limitations in this model. The following aspects could be considered in future work:

(1) Different geometries of the pillar's tip could be introduced into the current brush-structure model, for example spherical cap or concave shape, to investigate the effect of tip geometry on adhesion.
(2) The stiffness of all pillars was assumed identical in this work. A stiffness- (compliance-) gradient distribution may eliminate the macroscopic stress concentration. Furthermore, the pillar stiffness could be modeled with nonlinear springs as well. It is meaningful to develop a new algorithm for such a system and investigate the effect of heterogeneous pillar stiffness.
(3) Viscoelastic properties may also have a significant influence on adhesive contact. One can model the connection between the pillars and rigid base with the viscoelastic elements, for example Kelvin-Voigt or Standard model.

(4) Bunching of pillars was not considered in this work. However, it occurs commonly in the biological adhesion structure as well as in the related experiments, in particular when the fibrils are very soft. This effect should be taken into account in further study.

References

[1] Autumn, K.; Sitti, M.; Peattie, A.; Hansen, W.; Spenberg, S.; Liang, Y. A.; Kenny, T.; Fearing, J.; Israelachvili, J.; Full, R. J. Evidence for van der Waals adhesion in gecko setae. Proc. National Acad. Sci. USA 2002, 99, 12252–12256.

[2] Aristotle. Historia Animalium. Trans. Thompson, D. A. W., 1918.

[3] Irschick, D.J., et al. Effects of loading and size on maximum power output and gait characteristics in geckos. Journal of Experimental Biology, 2003, 206(22): p. 3923-3934.

[4] Irschick, D. J.; Austin, C. C.; Petren, K.; Fisher, R. N.; Losos, J. B.; Ellers, O. A comparative analysis of clinging ability among pad-bearing lizards. Biol. J. Linnean Soc. 1996, 59, 21–35.

[5] Fischer, S. C. L.; Arzt, E.; Hensel, R. Composite Pillars with a Tunable Interface for Adhesion to Rough Substrates. ACS Applied Materials & Interfaces, 2017, 9(1): p. 1036-1044.

[6] Fischer, S. C. L., et al. Funnel-Shaped Microstructures for Strong Reversible Adhesion. Advanced Materials Interfaces, 2017, p. 1700292.

[7] Yu, J., et al. Gecko-Inspired Dry Adhesive for Robotic Applications. Advanced Functional Materials, 2011, 21(16): p. 3010-3018.

[8] Khaled, W.B.; Sameoto, D. Anisotropic dry adhesive via cap defects. Bioinspiration & Biomimetics, 2013, 8(4): p. 44002.

[9] del Campo, A.; Greiner, C.; Arzt, E. Contact Shape Controls Adhesion of Bioinspired Fibrillar Surfaces. Langmuir, 2007, 23(20): p. 10235-10243.

[10] Afferrante, L.; Carbone, G. The ultratough peeling of elastic tapes from viscoelastic substrates. Journal of the Mechanics and Physics of Solids, 2016, 96: 223–234.

[11] Heide-Jørgensen, S.; Budzik, M. K.; Turner, K. T. Mechanics and fracture of structured pillar interfaces. Journal of the Mechanics and Physics of Solids, 2020, 137, 103825.

[12] Morano, C.; Zavattieri, P.; Alfano, M. Tuning energy dissipation in damage tolerant bio-inspired interfaces. Journal of the Mechanics and Physics of Solids, 2020, 103965.

[13] Gorb, S.; Scherge, M. Biological Microtribology: Anisotropy in Frictional Forces of Orthopteran Attachment Pads Reflects the Ultrastructure of a Highly Deformable Material. Proceedings: Biological Sciences, 2000, 267(1449), 1239-1244.

[14] Scherge, M.; Gorb, S. N. Biological Micro- and Nanotribology: Nature's Solutions, Springer, Berlin 2001.

[15] Huber, G.; Gorb, S. N.; Spolenak, R.; Arzt, E. Resolving the nanoscale adhesion of individual gecko spatulae by atomic force microscopy. Biol. Lett. 2005, 1, 2.

[16] Huber, G.; Mantz, H.; Spolenak, R.; Mecke, K.; Jacobs, K.; Gorb, S. N.; Arzt, E. Evidence for capillarity contributions to gecko adhesion from single spatula nanomechanical measurements. Proc. Natl. Acad. Sci. USA 2005, 102, 16293.

[17] Bhushan, B. Adhesion of multi-level hierarchical attachment systems in gecko feet. J. Adhes. Sci. Technol. 2007, 21, 1213–1258.

[18] Bhushan, B. Nanotribology and nanomechanics: an introduction, 2nd edn. Heidelberg, Germany: Springer, 2008.

[19] Ruibal, R.; Ernst, V. Structure of Digital Setae of Lizards. Journal of Morphology, 1965. 117(3): p. 271-293.

[20] Tian, Y.; Pesika, N.; Zeng, H. B.; Rosenberg, K.; Zhao, B. X.; McGuiggan, P.; Autumn, K.; Israelachvili, J. Adhesion and friction in gecko toe attachment and detachment. Proc. Natl. Acad. Sci. USA, 2006, 103(51):19320–19325.

[21] Autumn, K.; Liang, Y. A.; Hsieh, S. T.; Zesch, W.; Chan, W. P.; Kenny, T. W.; Fearing, R.; Full, R. J. Adhesive force of a single gecko foot-hair. Nature, 2000, 405, 6787, pp. 681685.

[22] Sun, W.; Neuzil, P.; Kustandi, T. S.; Oh, S.; Samper, V. D. The nature of the gecko lizard adhesive force. Biophys. J., 2005, Vol. 89, No. 2, pp. 14-17.

[23] Jeonga, H. E.; Suha, K. Y. Nanohairs and nanotubes: Efficient structural elements for gecko-inspired artificial dry adhesives. Nano. Today, 2009, 4, 335-46.

[24] Spolenak, R.; Gorb, S.; Arzt, E. Adhesion design maps for bio-inspired attachment systems. Acta. Biomaterialia, 2005, 1, 5-13.

[25] Schubert, B.; Majidi, C.; Groff, R. E.; Baek, S.; Bush, B.; Maboudian, R.; Fearing, R. S. Towards friction and adhesion from high modulus microfiber arrays J. Adhesion Sci. Technol., 2007, 21, 1297-315.

[26] Gu, Z.; Li, S.; Zhang, F.; Wang, S. Understanding Surface Adhesion in Nature: A Peeling Model. Adv. Sci., 2016, 1500327.

[27] Hui, C.-Y.; Glassmaker, N. J.; Tang, T.; Jagota, A. Design of biomimetic fibrillar interfaces: 1. Mechanics of enhanced adhesion. J. R. Soc. Interface, 2004, 1.

[28] Geim, A. K.; Dubonos, S. V.; Grigorieva, I. V.; Novoselov, K. S.; Zhukov, A. A.; Shapoval, S. Y. Microfabricated adhesive mimicking gecko foot-hair. Nat. Mater, 2003, 2(7):461-3.

[29] Peressadko, A.; Gorb, S. N. When less is more: experimental evidence for tenacity enhancement by division of contact area. J. Adhes., 2004, 80(4):247–261.

[30] Ge, L.; Sethi, S.; Ci, L.; Ajayan, P. M.; Dhinojwala, A. Carbon nanotube-based synthetic gecko tapes. Proc. Natl. Acad. Sci. U.S.A., 2007, 104, 10792–10795.

[31] Sethi, S.; Ge, L.; Ci, L.; Ajayan, P. M.; Dhinojwala, A. Gecko-Inspired Carbon Nanotube-Based Self-Cleaning Adhesives. Nano. Lett., 2008, 8, 822–825.

[32] Greiner, C.; Arzt, E.; del Campo, A. Hierarchical gecko-like adhesives. Adv. Mater., 2009, 21, 4, 479–482.

[33] Murphy, M. P.; Kim, S.; Sitti, M. Enhanced adhesion by gecko-inspired hierarchical fibrillar adhesives. ACS Appl. Mater Interfaces, 2009, 04, 1(4):849-55.

[34] Kim, S.; Sitti, M. Effect of head shape on the adhesion capability of mushroom-like biological adhesive structures. Appl. Phys. Lett., 2006, 89, 261911–261913.

[35] Gorb, S. N.; Varenberg, M.; Peressadko, A.; Tuma, J. Biomimetic mushroom-shaped fibrillar adhesive microstructure. J. R. Soc. Interface, 2007, 4, 271– 275.

[36] Wang, Y.; Hu, H.; Shao, J.; Ding, Y. Fabrication of Well-Defined Mushroom-Shaped Structures for Biomimetic Dry Adhesive by Conventional Photolithography and Molding. ACS Appl. Mater. Interfaces, 2014, 6, 2213−8.

[37] Hertz, H. On the contact of elastic solids. J Reine Angew Math, 1982, 92:156–171.

[38] Roberts, A. D. Ph.D. dissertation. Cambridge University, England, 1968.

[39] Kendall, K. Ph. D dissertation. Cambridge University, England, 1969.

[40] Bradley, R. S. The cohesive force between solid surfaces and the surface energy of solids. Phil Mag 1932, 13(86): 853–862.

[41] Dzyaloshinskii, I. E.; Lifshitz, E. M.; Pitaevskii, L. P. General Theory of van der Waals' Forces. Soviet Physics Uspekhi 1961, 4: 153–176.

[42] Johnson, K. L.; Kendall, K.; Roberts, A. D. Surface energy and the contact of elastic solids. Proc. R. Soc. Lond. A., 1971, 324, 301-313.

[43] Derjaguin, B. V.; Muller, V. M.; Toporov, Y. P. Effect of contact deformations on the adhesion of particles. Journal of Colloid and Interface Science, 1975, 53(2), pp. 314-326.

[44] Muller, V. M.; Derjaguin, B. V.; Toporov, Y. P. On two methods of calculation of the force of sticking of an elastic sphere to a rigid plane. Colloids and Surfaces, 1983, 7(3), pp. 251-259.

[45] Tabor, D. Surface forces and surface interactions, Journal of Colloid and Interface Science, 1977, 58(1), pp. 2-13.

[46] Muller, V. M.; Yushchenko, V. S.; Derjaguin, B. V. On the influence of molecular forces on the deformation of an elastic sphere and its sticking to a rigid plane. J. Colloid Interface Sci., 1980, 77, 91.

[47] Maugis, D. Adhesion of spheres: The JKR-DMT transition using a Dugdale model, J. Colloid Interface. Sci. 1992, 150, 243—269.

[48] Dugdale, D. S. Yielding of steel sheets containing slits. J. Mech. Phys. Solids, 1960, 8(2):100–104.

[49] Greenwood, J. A.; Williams, J. B. Contact of nominally flat surfaces. Proc. R. Soc. Lond. Ser. a-Math Phys. Eng. Sci., 1966, 295(1442), 300–319.

[50] Bush, A.; Gibson, R.; Thomas, T. The elastic contact of a rough surface. Wear, 1975, 35, 87–112.

[51] Persson, B. N. J. Theory of rubber friction and contact mechanics. J. Chem. Phys., 2001, 115, 3840-3861.

[52] Yang, C.; Tartaglino, U.; Persson, B. N. J.; Influence of surface roughness on superhydrophobicity. Phys. Rev. Lett., 2006, 97, 116103.

[53] Yang, C.; Tartaglino, U.; Persson, B. N. J. Nanodroplets on rough hydrophilic and hydrophobic surfaces. Eur. Phys. J. E., 2008, 25, 139-152.

[54] Persson, B. N. J. Contact mechanics for randomly rough surfaces. Surf. Sci. Rep., 2006, 61, 201-227.

[55] Hyun, S.; Pei, S.; Molinari, J.-F.; Robbins, M. O. Finite-element analysis of contact between elastic self-affine surfaces. Phys. Rev. E, 2004, 70, 026117.

[56] Afferrante, L.; Bottiglione, F.; Putignano, C.; et al. Elastic Contact Mechanics of Randomly Rough Surfaces: An Assessment of Advanced Asperity Models and Persson's Theory. Tribol. Lett., 2018, 66, 75.

[57] Pohrt, R.; Popov, V. L. Normal contact stiffness of elastic solids with fractal rough surfaces. Physical Review Letters, 2012, 108, 104301, 1–4.

[58] Ciavarella, M. A very simple estimate of adhesion of hard solids with rough surfaces based on a bearing area model. Meccanica, 2018, 53, 241–250.

[59] Ciavarella, M. On Pastewka and Robbins' Criterion for Macroscopic Adhesion of Rough Surfaces. Journal of Tribology, 2017, 139(3), 031404.

[60] Ciavarella, M.; Papangelo, A. A modified form of Pastewka–Robbins criterion for adhesion. The Journal of Adhesion, 2017, 1-11.

[61] Ciavarella, M.; Papangelo, A.; Afferrante, L. Adhesion between self-affine rough surfaces: Possible large effects in small deviations from the nominally Gaussian case. Tribology International, 2017, 109, 435-440.

[62] Fuller, K. N. G.; Tabor, D. Effect of surface-roughness on adhesion of elastic solids. Proc. R. Soc. Lond. Ser. a-Math Phys. Eng. Sci., 1975, 345(1642), 327–342.

[63] Briggs, G. A. D.; Briscoe, B. J. Effect of surface-topography on adhesion of elastic solids. J. Phys. D-Appl. Phys., 1977, 10(18), 2453–2466.

[64] Fuller, K. N. G.; Roberts, A. D. Rubber rolling on rough surfaces. J. Phys. D-Appl. Phys., 1981, 14 (2), 221–239.

[65] Guduru, P. R. Detachment of a rigid solid from an elastic wavy surface: theory. J. Mech. Phys. Solids, 2007, 55, 445–472.

[66] Schargott, M.; Popov, V. L.; Gorb, S. Spring model of biological attachment pads. J. Theor. Biol., 2006, 243:48–53.

[67] Schargott, M. A mechanical model of biomimetic adhesive pads with tilted and hierarchical structures. Bioinspiration & biomimetics, 2009, 4 (2), 026002.

[68] Jagota, A.; Hui, C-Y. Adhesion, friction, and compliance of bio-mimetic and bio-inspired structured interfaces. Materials Science & Engineering R., 2011, 72, 12, 253-292.

[69] Hui, C.-Y.; Glassmaker, N. J.; Jagota, A. How Compliance Compensates for Surface Roughness in Fibrillar Adhesion. The Journal of Adhesion, 2005, 81:7-8, 699-721.

[70] Porwal, P. K.; Hui, C-Y. Strength statistics of adhesive contact between a fibrillar structure and a rough substrate. J. R, Soc., Interface, 2008, 5: 441–448.

[71] Arzt, E.; Gorb, S.; Spolenak, R. From micro to nano contacts in biological attachment devices. Proc. Natl. Acad. Sci. USA, 2003, 100, 19, 10603-10606.

[72] Spolenak, R.; Gorb, S.; Gao, H. J.; Arzt, E. Effects of contact shape on the scaling of biological attachments. Proc. R. Soc. Lond. Ser. A-Math Phys. Eng. Sci., 2005, 461(2054):305–319.

[73] Varenberg, M.; Murarash, B.; Kligerman, Y.; Gorb, S. N. Geometry-controlled adhesion: revisiting the contact splitting hypothesis. Appl. Phys. A-Mater Sci. Process, 2011, 103(4):933–938.

[74] Popov, V. L.; Pohrt, R.; Li, Q. Strength of adhesive contacts: Influence of contact geometry and material gradients. Friction, 2017, 5, 308–325.

[75] Li, Q.; Popov, V. L. Adhesive force of flat indenters with brush-structure. Mechanical Engineering, 2018, 16, 1, 1 – 8.

[76] Li, Q.; Popov, V. L. Adhesive contact of rough brushes. Beilstein J. Nanotechnol, 2018, 9, 2405–2412.

[77] Borodich, F.; Savencu, O. Hierarchical Models of Engineering Rough Surfaces and Bio-inspired Adhesives in Bio-inspired Structured Adhesives, Biologically-Inspired Systems; Heepe L., Xue L., Gorb S. (eds). Springer: Cham., 2017, 9,179-219.

[78] Tian, Y.; Wan, J.; Pesika, N.; Zhou, M. Bridging nanocontacts to macroscale gecko adhesion by sliding soft lamellar skin supported setal array. Scientific reports, 2013, 3, 1382.

[79] Argatov, I.; Li, Q.; Popov, V.L. Cluster of the Kendall-type adhesive microcontacts as a simple model for load sharing in bioinspired fibrillar adhesives. Archive of Applied Mechanics, 2019, 89, 1447–1472.

[80] Griebel, M.; Knapek, S.; Zumbusch, G. Numerical Simulation in Molecular Dynamics. Berlin, Heidelberg: Springer, 2007.

[81] Eid, H.; Adams, G. G.; McGruer, N. E.; Fortini, A.; Buldyrev, S.; Srolovitz, D. A Combined Molecular Dynamics and Finite Element Analysis of Contact and Adhesion of a Rough Sphere and a Flat Surface. Tribology Transactions, 2011, 54:6, 920-928.

[82] Kim, H. J.; Kim, W. K.; Falk, M. L.; et al. MD Simulations of Microstructure Evolution during High-Velocity Sliding between Crystalline Materials. Tribol. Lett., 2007, 28, 299–306.

[83] Yang, C.; Persson, B. N. J. Molecular Dynamics Study of Contact Mechanics: Contact Area and Interfacial Separation from Small to Full Contact. Phys. Rev. Lett., 2008, 100, 024303.

[84] Gilabert, F. A.; Krivtsov, A. M.; Castellanos, A. A Molecular Dynamics Model for Single Adhesive Contact. Meccanica, 2006, 41, 341–349.

[85] Anciaux, G.; Molinari, J. F. Contact mechanics at the nanoscale, a 3D multiscale approach. Int. J. Numer. Meth. Engng., 2009, 79: 1041-1067.

[86] Crocombe, A. D.; Adams, R. D. Peel Analysis Using the Finite Element Method. The Journal of Adhesion, 1981, 12:2, 127-139.

[87] Du, Y.; Chen, L.; McGruer, N. E.; Adams, G. G.; Etsion, I. A finite element model of loading and unloading of an asperity contact with adhesion and plasticity. Journal of Colloid and Interface Science, 2007, 312, 2, 522-528.

[88] Takahashi, K., et al. Geckos' foot hair structure and their ability to hang from rough surfaces and move quickly. Int. J. Adhesion & Adhesives, 2006, 26, 639-643.

[89] Cheng, A. H-D.; Cheng D. T. Heritage and early history of the boundary element method. Engineering Analysis with Boundary Elements, 2005, 29: 268–302.

[90] Cruse, T. A. Boundary Element Analysis in Computational Fracture Mechanics. Kluwer, Dordrecht, 1988.

[91] Blandford, G. E.; Ingraffea, A. R.; Liggett, J. A. Two-dimensional stress intensity factor computations using the boundary element method. International Journal for Numerical Methods in Engineering, 1974, 17(3): 387–404.

[92] Ren, N.; Lee, S. C. Contact simulation of three-dimensional rough surfaces using moving grid method. J. Tribol., 1993, 115(4): 597-601.

[93] Peng, W.; Bhushan, B. Transient analysis of sliding contact of layered elastic/plastic solids with rough surfaces. Microsyst. Technol., 2003, 9(5): 340-345.

[94] Polonsky, I.A.; Keer, L.M. A numerical method for solving rough contact problems based on the multi-level multi-summation and conjugate gradient techniques. Wear, 1999, 231, 206–219.

[95] Willner, K. Fully coupled frictional contact using elastic half space theory. J. Tribol., 2008, 130(3): 031405.

[96] Boussinesq, V. J. Application des Potentiels l'Etude del'Equilibre et du. S. 1, Gautier-Villar, 1882.

[97] Venner, C.; Lubrecht, A. Multilevel Methods in Lubrication. Elsevier Tribology Series, 2000, 37.

[98] Vollebregt, E. A. H. A new solver for the elastic normal contact problem using conjugate gradients, deflation, and an FFT-based preconditioner. Journal of Computational Physics, 2014, 257: 333-351.

[99] Wang, Q.; Sun, L.; Zhang, X.; Liu, S.; Zhu D. FFT-Based Methods for Computational Contact Mechanics. Front. Mech. Eng., 2020, 6, 61.

[100] Joe, J.; Scaraggi, M.; Barber, J. R. Effect of fine-scale roughness on the tractions between contacting bodies. Tribol. Int. 2017, 111, 52–56.

[101] Wu, J. J. (2012). Numerical simulation of the adhesive contact between a slightly wavy surface and a half-space. J. Adhes. Sci. Technol. 26, 331–351.

[102] Bazrafshan, M.; de Rooij, M. B.; Valefi, M.; Schipper, D. J. Numerical method for the adhesive normal contact analysis based on a Dugdale approximation. Tribol. Int., 2017, 112, 117-128.

[103] Pohrt, R.; Popov, V.L. Adhesive contact simulation of elastic solids using local mesh-dependent detachment criterion in Boundary Elements Method. Facta universitatis – series Mechanical Engineering, 2015, 13. 3-10.

[104] Argatov, I.; Li, Q.; Pohrt, R. et al. Johnson-Kendall-Roberts adhesive contact for a toroidal indenter. Proceedings of the Royal Society of London A: Mathematical, Physical and Engineering Sciences 2016, 472(2191).

[105] Li, Q.; Argatov, I.; Popov, V. L. Onset of detachment in adhesive contact of an elastic half-space and flatended punches with non-circular shape: analytic estimates and comparison with numeric analysis. Journal of Physics D: Applied Physics, 2018.

[106] Li, Q.; Popov, V. L. Adhesive contact between a rigid body of arbitrary shape and a thin elastic coating. Acta Mech. 2019, 230, 2447–2453.

[107] Pohrt, R.; Li, Q. Complete boundary element formulation for normal and tangential contact problems. Phys. Mesomech, 2014, 17, 334–340.

[108] Kendall, K. The adhesion and surface energy of elastic solids. Journal of Physics D: Applied Physics, 1971, 4(8): 1186.

[109] Popov, V. L. Contact Mechanics and Friction. Physical Principles and Applications, 2nd ed.; Springer: Berlin, Germany, 2017.

[110] Takahashi, K.; Mizuno, R.; Onzawa, T. Influence of the stiffness of the measurement system on the elastic adhesional contact. Journal of Adhesion Science and Technology, 1995, 9:11, 1451-1464.

[111] Liu, S.; Wang, Q.; Liu, G. A versatile method of discrete convolution and FFT (DC-FFT) for contact analyses. Wear. 2000, 243, 101–111.

[112] Li, Q. Simulation of a Single Third-body Particle in Frictional Contact. Facta Universitatis Series Mechanical Engineering, 2020, 18.

[113] Popov, V. L.; Pohrt, R. Adhesive wear and particle emission: Numerical approach based on asperity-free formulation of Rabinowicz criterion. Friction, 2018, 6.

[114] Yao, H.; Gao, H. Mechanics of robust and releasable adhesion in biology: bottom-up designed hierarchical structures of gecko. J Mech Phys Solids, 2006, 54(6):1120–1146.

[115] Kamperman, M.; Kroner, E.; del Campo, A.; McMeeking, R.M.; Arzt, E. Functional Adhesive Surfaces with “Gecko” Effect: The Concept of Contact Splitting. Adv. Eng. Mater., 2010, 12, 335-348.

[116] O'Rorke, R.; Terry, S.; Taylor, H. Bioinspired fibrillar adhesives: A review of analytical models and experimental evidence for adhesion enhancement by surface patterns. Journal of Adhesion Science and Technology, 2015, 30.

[117] Gao, H. J.; Yao, H. M. Shape insensitive optimal adhesion of nanoscale fibrillar structures. Proceedings of the National Academy of Sciences, 2004, 101 (21).

[118] Barreau, V.; Hensel, R.; Guimard, N.K.; Ghatak, A.; McMeeking, R.M.; Arzt, E. Fibrillar Elastomeric Micropatterns Create Tunable Adhesion Even to Rough Surfaces. Adv. Funct. Mater., 2016, 26, 4687-4694.

[119] Sitti, M.; Fearing, R. S. Synthetic gecko foot-hair micro/nano-structures as dry adhesives. Journal of Adhesion Science and Technology, 2003, 17, 1055-1073.

[120] Yurdumakan, B.; Raravikar, N.R.; Ajayan, P.M.; Dhinojwala, A. Synthetic gecko foot-hairs from multiwalled carbon nanotubes, Chem. Commun. 2005, 30, 3799-3801.

[121] Boesel, L.F.; Greiner, C.; Arzt, E; del Campo, A. Gecko-Inspired Surfaces: A Path to Strong and Reversible Dry Adhesives. Adv. Mater., 2010, 22: 2125-2137.

[122] Majumder, A.; Sharma, A.; Ghatak, A. Bio-Inspired Adhesion and Adhesives: Controlling Adhesion by Micro-nano Structuring of Soft Surfaces in Microfluids and Microfabrication; Springer, Boston, MA. 2010, 283-307.

[123] Autumn, K.; Peattie, A.M. Mechanisms of Adhesion in Geckos. Integrative and Comparative Biology, 2002, 42, 6, 1081–1090.

[124] Persson, B. N. J., J. On the mechanism of adhesion in biological systems. Chem. Phys., 2003, 118, 7614–7621.

[125] Northen, M.; Foster, K. A batch fabricated biomimetic dry adhesive. Nanotechnology, 2005, 16, 1159.

[126] Li, Q.; Pohrt, R.; Popov, V. L. Adhesive Strength of Contacts of Rough Spheres. Front. Mech. Eng., 2019, 5:7.

[127] Briggs, G. A. D.; Briscoe, B. J. The effect of surface topography on the adhesion of elastic solids. J. Phys. D Appl. Phys., 1977, 10, 2453–2466.

[128] Barber, J. R. Contact Mechanics; Springer: Berlin, Germany, 2018.

[129] Fuller, K. N. G.; Tabor, D. The effect of surface roughness on the adhesion of elastic solids. Proc. R. Soc. London, Ser. A. 1975, 345, 327–342.

[130] Chen, B.; Wu, P. D.; Gao, H. Hierarchical modelling of attachment and detachment mechanisms of gecko toe adhesion. Proc. R. Soc. Lond. Ser. A-Math Phys. Eng. Sci., 2008, 464 (2094):1639–1652.

[131] Brodoceanu, D.; Bauer, C.; Kroner, E.; Arzt, E.; Kraus, T. Hierarchical bioinspired adhesive surfaces - A review. Bioinspiration & Biomimetics, 2016, 11, 051001.

[132] Gao, H.; Wang, X.; Yao, H.; Gorb, S.; Arzt, E. Mechanics of hierarchical adhesion structures of geckos. Mechanics of Materials - MECH MATER, 2005, 37.

[133] Persson, B. N. J.; Gorb, S. The effect of surface roughness on the adhesion of elastic plates with application to biological systems. J. Chem. Phys., 2003, 119, 11437.

[134] Huber, G.; Gorb, S.; Hosoda, N.; Spolenak, R.; Arzt, E. Influence of surface roughness on gecko adhesion. Acta Biomater, 2007, 3, 607-10.

[135] Russell, A. P.; Johnson, M. K. Real-world challenges to, and capabilities of, the gekkotan adhesive system: contrasting the rough and the smooth. Can. J. Zool., 2007, 85, 1228-38.

[136] Hess, M. Über die exakte Abbildung ausgewählter dreidimensionaler Kontakte auf Systeme mit niedrigerer räumlicher Dimension (German Edition). Cuvillier Verlag, Göttingen, 2011.

[137] Kim, T. W.; Bhushan, B. Adhesion analysis of multi-level hierarchical attachment system contacting with a rough surface. Journal of Adhesion Science and Technology, 2007, 21, 1, 1-20.

[138] Hui, C. Y.; Glassmaker, N. J.; Tang, T.; Jagota, A. Design of biomimetic fibrillar interfaces: 2. Mechanics of enhanced adhesion. J. R. Soc. Interface, 2004, 1(1).

[139] Yao, H.; Gao, H. Multi-scale cohesive laws in hierarchical materials. Int. J. Solids Struct., 2007, 44, 8177.

[140] Willert, E.; Li, Q.; Popov, V. L. The JKR-adhesive normal contact problem of axisymmetric rigid punches with a flat annular shape or concave profiles. Facta Universitatis-Series Mechanical Engineering, 2016, 14(3), 281-292.

[141] Johnson, K. L. Contact Mechanics. Cambridge, (UK), 2003.